RESEARCH ARTICLE SUMMARY

MOLECULAR BIOLOGY

Cryo-EM structure of human telomerase dimer reveals H/ACA RNP-mediated dimerization

Sebastian Balch†, Zala Sekne†, Elsa Franco-Echevarría†, Patryk Ludzia, Rachael C. Kretsch, Wenqing Sun, Haopeng Yu, George E. Ghanim, Sigurdur Thorkelsson, Yiliang Ding, Rhiju Das, Thi Hoang Duong Nguyen*

Full article and list of author affiliations: https://doi.org/10.1126/science.adr5817

INTRODUCTION: In most eukaryotes, telomerase ribonucleoprotein (RNP) counteracts the end-replication problem by extending telomeric DNA at chromosome ends. This enzyme requires a telomerase reverse transcriptase (TERT) and an RNA template embedded within telomerase RNA (hTR in humans) for DNA synthesis. Early size fractionation studies estimated the mass of human telomerase to be considerably larger than the combined mass of TERT and hTR, leading to competing models of its composition. Some propose that human telomerase functions as a monomer of TERT and hTR with additional protein factors, whereas others suggest a dimeric form of TERT and hTR. Cryo–electron microscopy (cryo-EM) structures of human telomerase revealed a monomeric TERT-hTR composition and the identity of the additional factors. Human telomerase adopts a bilobed architecture scaffolded by hTR. One lobe, the catalytic core, consists of TERT, activity-essential domains of hTR, and a histone H2A-H2B dimer. The other lobe, called the Hinge and ACA box (H/ACA) RNP, contains two H/ACA heterotetramers and telomerase Cajal body localization factor (TCAB1), all bound to the H/ACA domain of hTR. These structures account for the observed mass and extensive prior evidence supporting the monomeric form as the active configuration. Nevertheless, questions remain about the potential existence of a dimeric state of human telomerase.

RATIONALE: In this study, we leveraged large cryo-EM datasets of human telomerase to explore architectural diversity within the purified sample. We identified and resolved the structure of a human telomerase dimer from a small subset of particles. We next validated our structural findings through mutagenesis, biochemical assays, and in-cell studies. Our work integrated previous evidence on telomerase dimerization and identified key molecular interactions essential for dimer formation and their importance in telomere maintenance.

RESULTS: The cryo-EM structure of the human telomerase dimer confirms its existence and reveals an assembly of two intertwined telomerase monomers, each containing a catalytic core and an H/ACA RNP. Using tandem-affinity purification, we found that while the reconstituted human telomerase is predominantly monomeric, the dimeric complex exists at low abundance, consistent with our cryo-EM analyses. In contrast to previous reports, we observed no interactions between the two catalytic cores of the dimer. Biochemical and structural analyses suggest that the dimer is catalytically active, but the two catalytic cores engage with telomeric DNA independently and show no cooperativity.

Dimerization is primarily mediated by the two H/ACA RNPs. We identified interactions between hTR of one protomer and the H/ACA proteins of the other protomer, where several mutations associated with premature aging disease cluster. Disrupting this interface impairs telomerase assembly, reduces telomerase activity, and compromises telomere maintenance in cells, explaining the short telomere phenotype linked to disease mutations. Our data suggest that telomerase dimerization may aid telomerase assembly by stabilizing the H/ACA proteins during RNP formation.

Additionally, the structure reveals roles for the H/ACA protein GAR1. GAR1 facilitates the dimerization through cross-protomer GAR1-GAR1 interactions and its binding to the H2A-H2B histone dimer. Within a single telomerase protomer, we also resolved a G-quadruplex formed at the 5′ end of hTR, which is stabilized by GAR1.

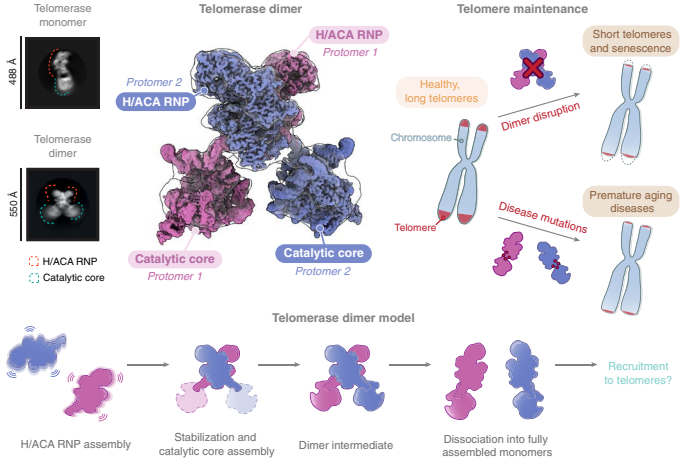

Structure and function of the human telomerase dimer. Two human telomerase protomers intertwine to form a low-abundance X-shaped dimer stabilized by interactions between their H/ACA RNPs. Disrupted dimerization impairs telomere maintenance in cells and is also associated with premature aging diseases. The dimer is proposed to play a role in stabilizing the H/ACA RNP during human telomerase assembly.

CONCLUSION: The composition of human telomerase had been a subject of ongoing debate, with the first cryo-EM structure offering key insights into its organization. In this study, we resolved the structure of a low-abundance human telomerase dimer, unambiguously demonstrating its existence and composition. By elucidating the dimerization interface, we provide insights into its potential role in telomere maintenance. We propose that telomerase dimerization serves a stabilizing function during human telomerase assembly, before full RNP maturation. Given the importance of proper telomerase assembly, our findings have important implications for telomere-related diseases and therapeutic strategies. □

*Corresponding author. Email: knguyen@mrc-lmb.cam.ac.uk †These authors contributed equally to this work. Cite this article as S. Balch *et al.*, *Science* 389, eadr5817 (2025). DOI: 10.1126/science.adr5817

MOLECULAR BIOLOGY

Cryo-EM structure of human telomerase dimer reveals H/ACA RNP-mediated dimerization

Sebastian Balch[1]†, Zala Sekne[1]†‡, Elsa Franco-Echevarría[1]†, Patryk Ludzia[1]§, Rachael C. Kretsch[2], Wenqing Sun[3,4], Haopeng Yu[4], George E. Ghanim[1]¶, Sigurdur Thorkelsson[1]#, Yiliang Ding[4], Rhiju Das[2,5,6], Thi Hoang Duong Nguyen[1]*

Telomerase ribonucleoprotein (RNP) synthesizes telomeric repeats at chromosome ends using a telomerase reverse transcriptase (TERT) and a telomerase RNA (hTR in humans). Previous structural work showed that human telomerase is typically monomeric, containing a single copy of TERT and hTR. Evidence for dimeric complexes exists, although the composition, high-resolution structure, and function remain elusive. Here, we report the cryo–electron microscopy (cryo-EM) structure of a human telomerase dimer bound to telomeric DNA. The structure reveals a 26-subunit assembly and a dimerization interface mediated by the Hinge and ACA box (H/ACA) RNP of telomerase. Premature aging disease mutations map to this interface. Disrupting dimer formation affects RNP assembly, bulk telomerase activity, and telomere maintenance in cells. Our findings address a long-standing enigma surrounding the telomerase dimer and suggest a role for the dimer in telomerase assembly.

Telomeres, situated at the ends of linear eukaryotic chromosomes, undergo shortening during each cell cycle as a result of incomplete genome replication (*1*). Telomerase is a ribonucleoprotein (RNP), which preserves telomere length by adding telomeric repeats (GGTTAG in humans) to the chromosome 3′ termini (*2*, *3*). Up to 90% of cancer cells confer cellular immortalization through telomerase activation (*4*, *5*). Conversely, mutations that compromise telomerase function contribute to a diverse range of premature aging diseases, such as dyskeratosis congenita (*6*, *7*).

The enzymatic activity of telomerase relies on a telomerase reverse transcriptase (TERT) and an internal RNA template contained in the telomerase RNA (TER or hTR in humans) (*2*). The human telomerase holoenzyme contains 11 accessory subunits, including a histone H2A-H2B dimer, two sets of the Hinge and ACA box (H/ACA) heterotetramers [dyskerin, nucleolar protein 10 (NOP10), H/ACA ribonucleoprotein complex subunit 2 (NHP2), and H/ACA ribonucleoprotein complex subunit 1 (GAR1)], and telomerase Cajal body localization factor (TCAB1) (*8*, *9*). Recent cryo–electron microscopy (cryo-EM) structures revealed the segregation of human telomerase subunits into two lobes flexibly connected by hTR (*8*–*10*). In one lobe, TERT and histone H2A-H2B bind two activity-essential domains of hTR: the pseudoknot/template domain (PK/t) and conserved regions 4 and 5 (CR4/5) (Fig. 1, A and B). This lobe, known as the catalytic core, is the site where telomeric DNA synthesis occurs. In the other lobe, the H/ACA proteins and TCAB1 associate with the H/ACA domain of hTR to form the H/ACA RNP (Fig. 1, A and B), which plays a crucial role in telomerase biogenesis (*11*–*13*).

There have been reports suggesting the existence of a dimeric form of human telomerase. Size fractionation experiments indicated that the molecular weight of human telomerase is in the range of 550 to 670 kDa (*14*–*17*). Human telomerase was, thus, proposed to be a dimer of TERT, hTR, and dyskerin (*16*, *17*). However, extensive evidence suggests that human telomerase functions as a monomer of TERT and hTR (*8*–*10*, *18*–*22*). A monomeric telomerase holoenzyme, consistent with the composition revealed by recent structural studies (578 kDa), would exhibit a comparable size fractionation pattern (*8*, *9*, *21*). Therefore, relying on size alone does not definitively distinguish between the proposed dimeric composition and the monomeric composition observed by cryo-EM.

Additional support for dimeric human telomerase comes from purification of telomerase with two differently tagged TERT or two different constructs of the hTR template sequence as well as from single-molecule experiments (*15*, *17*, *19*). These studies demonstrated the presence of telomerase RNPs with two copies of either TERT or hTR in addition to monomeric telomerase RNPs. However, it remains unclear from these studies whether both TERT and hTR simultaneously exist in duplicate and whether other telomerase accessory subunits are also present. Without a comprehensive understanding of the structure, composition, and molecular interactions that drive dimerization, the functional role of such dimeric telomerase remains unknown.

A population of human telomerase forms dimers

We initially collected cryo-EM data of human telomerase with the telomerase recruitment complex, TPP1-POT1-TIN2 (TPT), and telomeric DNA to understand telomerase interactions with the DNA substrate (fig. S1, A and B). Close inspection of two-dimensional (2D) class averages revealed a small subset of particles featuring two attached telomerase molecules (Fig. 1C and fig. S1C). We devised a data processing strategy to enrich for such particles across four independent cryo-EM datasets and obtained a 6.2-Å consensus map (see Materials and methods; figs. S2 and S3, A to D, and table S1). By unambiguously fitting the map with published structures of human telomerase (*9*, *23*), we verified the identity of these particles as telomerase homodimers (Fig. 1, E to G).

To test whether the telomerase dimer is formed during telomerase reconstitution in human cells, we used a split nanoluciferase assay. In this assay, cells were cotransfected with hTR and TERT containing split nanoluciferase constructs, named LgBiT and SmBiT (fig. S4A) (*24*). Bioluminescence is obtained when the LgBiT and SmBiT fragments are in close proximity. We detected bioluminescence only in cells transfected with two TERT constructs, one carrying LgBiT and the other carrying SmBiT (fig. S4B). This suggests that telomerase complexes with two TERT molecules in close proximity form in cells.

To detect the presence of the human telomerase dimer biochemically, we prepared telomerase with a combination of two differentially tagged TERTs: ZZ-3xFlag-TERT (ZZ-F-TERT) and ZZ-twin-Strep-SUMO*-TERT (ZZ-SS-TERT). We then used a two-step purification strategy involving oligonucleotide-affinity purification (O-purification) on hTR followed by Strep-Tactin pulldown, a strategy similar to that used for cryo-EM sample preparation (Materials and methods) (Fig. 1D). Immunoblots of the resulting Strep-Tactin elution with an anti-Flag antibody revealed the copurification of ZZ-F-TERT (Fig. 1H, lane 3). No nonspecific binding of ZZ-F-TERT to the Strep-Tactin resin was detected (Fig. 1H, lane 6). This demonstrates the existence of telomerase RNP containing both tagged versions of TERT simultaneously. Furthermore, the intensity of the Flag-tagged TERT band in the Strep-Tactin elution was weak relative to that in the oligonucleotide elution (OE) fraction (Fig. 1H, lanes 1 and 3). Hence, the dual-tagged complexes constitute only a small fraction of our reconstituted complexes, consistent with the low particle distribution of the dimer in our cryo-EM data (fig. S2).

[1]MRC Laboratory of Molecular Biology, Cambridge, UK. [2]Biophysics Program, Stanford University, Stanford, CA, USA. [3]Key Laboratory of Molecular Epigenetics of the Ministry of Education, Northeast Normal University, Changchun, China. [4]Department of Cell and Developmental Biology, John Innes Centre, Norwich Research Park, Norwich, UK. [5]Department of Biochemistry, Stanford University, Stanford, CA, USA. [6]Howard Hughes Medical Institute, Stanford University, Stanford, CA, USA. ***Corresponding author. Email: knguyen@mrc-lmb.cam.ac.uk** †These authors contributed equally to this work. ‡Present address: Illumina Inc., San Diego, CA, USA. §Present address: Department of Biochemistry, University of Cambridge, Cambridge, UK. ¶Present address: Department of Molecular Biology, Princeton University, Princeton, NJ, USA. #Present address: Thermo Fisher Scientific, Eindhoven, Netherlands.

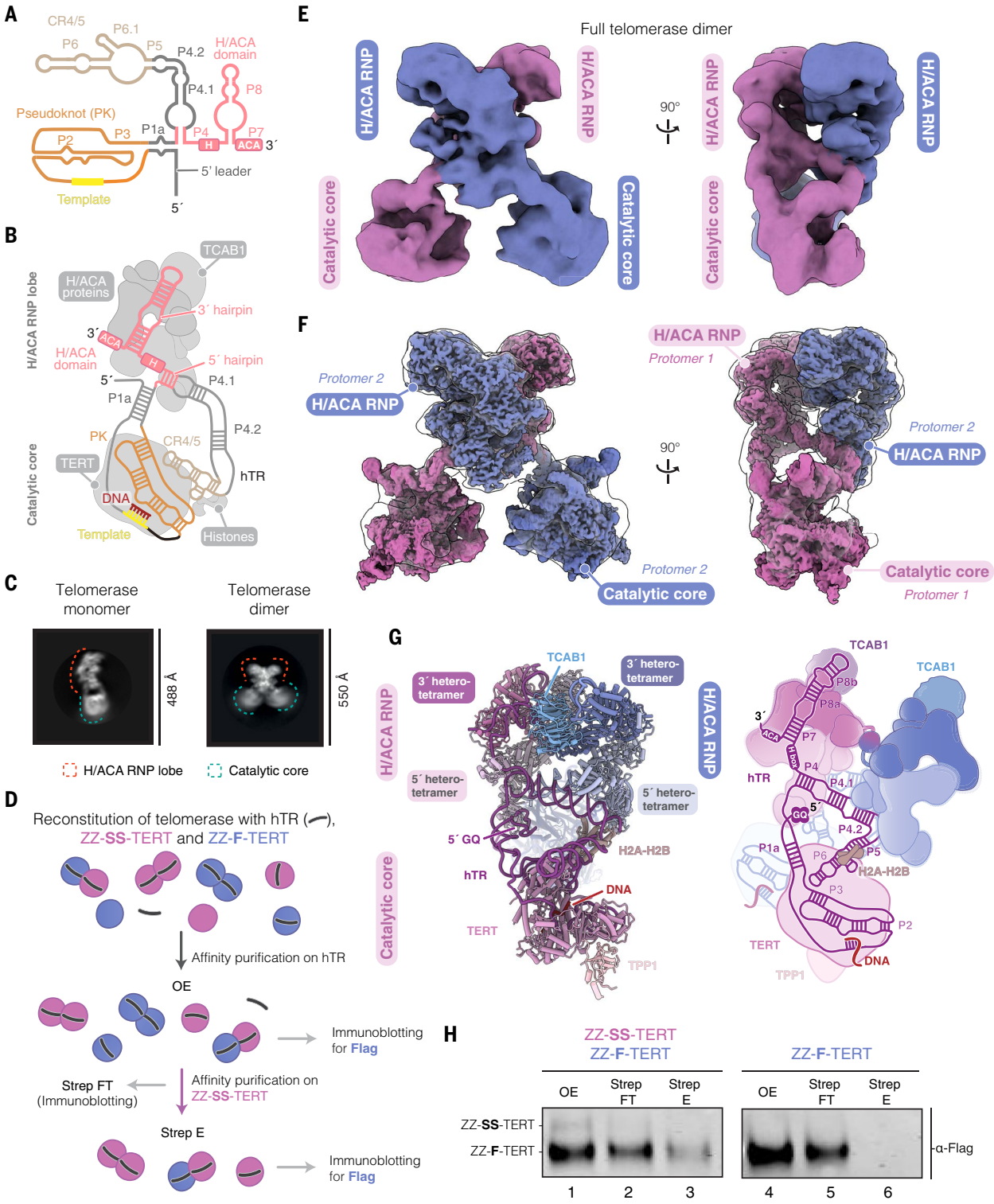

Fig. 1. Structure of the human telomerase dimer. (**A**) Schematic showing secondary structure of hTR. (**B**) Schematic of human telomerase monomer. The domains of hTR are colored as shown in (A). (**C**) Representative cryo-EM 2D class averages of the telomerase monomer and the telomerase dimer. (**D**) Schematic of the purification strategy to probe for the human telomerase dimer using ZZ-SS-TERT and ZZ-F-TERT. ZZ, protein A; SS, twin-Strep tag; F, Flag tag; OE, oligonucleotide elution; Strep FT, Strep-Tactin flow-through; Strep E, Strep-Tactin elution. (**E**) A 6.2-Å consensus cryo-EM map of the full human telomerase dimer. The two protomers are colored in magenta and blue. (**F**) The consensus cryo-EM map of the full telomerase dimer with two fitted copies of the 3.0-Å cryo-EM reconstructions of the human telomerase H/ACA RNP protomer and the 3.3-Å cryo-EM reconstructions of the human telomerase catalytic core. These composite maps were obtained from focused classification and refinement on the H/ACA RNP and the catalytic cores separately. (**G**) Atomic model of the full telomerase dimer (left) as shown in (F) and the schematic of the structure (right) as shown in (F). The model was obtained through a combination of fitting published models, manual building, and DRRAFTER modeling (*23*,*26*,*27*). (**H**) Immunoblots of the telomerase sample with ZZ-SS-TERT and ZZ-F-TERT (left), and control telomerase with ZZ-F-TERT (right) obtained by purification strategy depicted in (D). An anti-Flag antibody was used.

To further confirm that the dual-tagged telomerase is the telomerase dimer, we isolated these particles using a double pulldown on both the Flag and Strep tags after O-purification and analyzed them using negative stain EM (fig. S5, A and C). The 2D class averages of these particles resemble those of the dimeric particles observed in the cryo-EM data (fig. S5, D to F), confirming their identity as telomerase dimers.

The telomerase dimer structure reveals its composition and an unexpected dimerization interface

The human telomerase dimer contains twice the number of subunits present in the telomerase holoenzyme (Fig. 1, B and E to G) (*9*). In the dimer structure, the two protomers intertwine in an X-shaped architecture, showcasing a near-twofold symmetry axis passing through the dimer interface (Fig. 1, E and F). Various regions of TERT within the catalytic core have been suggested to mediate dimer or multimer formation (*19*, *25*). However, our cryo-EM structure reveals that dimerization is primarily facilitated by interactions between the two H/ACA RNPs, with the two catalytic cores positioned away from the dimerization interface (Figs. 1, E and F, and 2D).

To resolve the dimerization interface, we performed signal subtraction and focused classification on the two H/ACA RNPs within the structure. We obtained a 3.0-Å-resolution map for a single H/ACA RNP protomer and a 3.9-Å-resolution map for the two H/ACA RNPs containing most of the dimerization interface (Fig. 1F; figs. S1D, S2, S3, E to

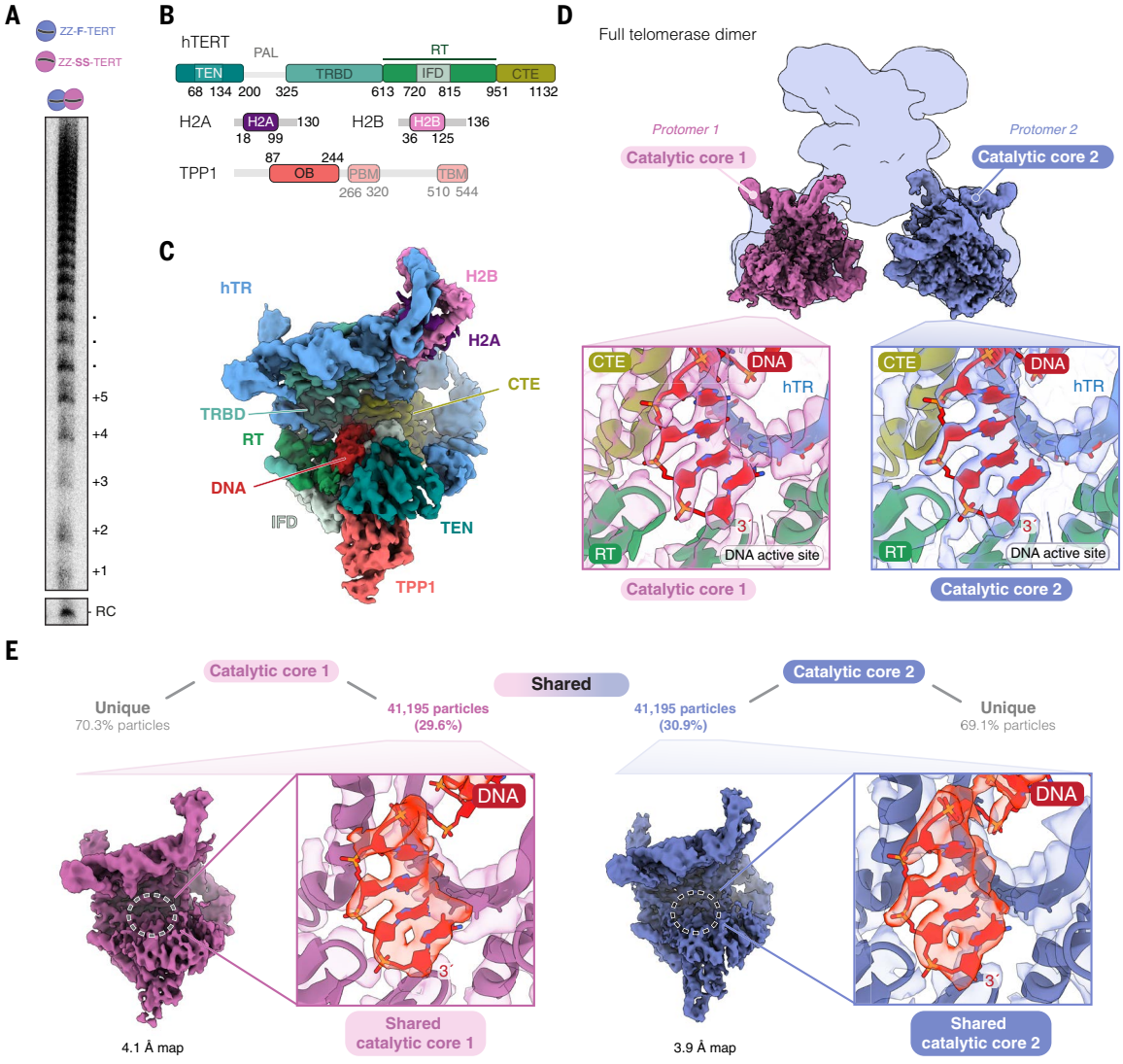

Fig. 2. The human telomerase dimer is catalytically active. (**A**)Telomerase activity assay of the purified dual-tagged human telomerase dimer following the procedure depicted in fig. S5A. RC, recovery control. (**B**) Domain organization of human TERT (hTERT), histones H2A and H2B, and TPP1. TEN, telomerase essential N-terminal; PAL, proline/arginine/glycine-rich linker; TRBD, telomerase RNA binding domain; RT, reverse transcriptase; IFD, insertion in the fingers domain; CTE, C-terminal extension; OB, oligonucleotide/oligosaccharide binding; PBM, POT1 binding motif; TBM, TIN2 binding motif. (**C**) A 3.3-Å cryo-EM map of the human telomerase catalytic core using C2-expanded particles. Domains are labeled and colored according to the color scheme in (B). (**D**) The consensus cryo-EM map of the full human telomerase dimer with fitted 3.8- and 3.6-Å cryo-EM reconstructions of the human telomerase catalytic cores 1 and 2, respectively. The maps were generated without applying symmetry functions. Insets show the close-up views of the DNA-bound telomerase active site of the catalytic core 1 (left) and catalytic core 2 (right). (**E**) Data processing strategy used to obtain the human telomerase catalytic cores from the shared particles, which originated from the subsets that gave the reconstructions of the two catalytic cores shown in (D). The shared particles are those found in both particle stacks used to generate 4.1-Å and 3.9-Å maps for catalytic cores 1 and 2, respectively. The maps of telomerase catalytic cores 1 and 2, obtained from only the shared particles, are shown with the DNA in the active sites.

L, and S6; and table S1). Henceforth, we refer to the latter reconstruction as the H/ACA RNP dimer. The improved resolution enabled model building, particularly of regions involved in dimerization (fig. S6 and table S1). We then docked atomic models of the catalytic cores bound to the recruitment factor TPP1 and the H/ACA RNP dimer into the consensus map, combined with RNA modeling by DRRAFTER, to obtain a complete atomic model for the dimeric telomerase complex (Fig. 1G, fig. S7, and data S1) (*23*, *26*, *27*).

The telomerase holoenzyme dimer is catalytically active

We asked whether dimerization affects the ability of TERT to bind and extend telomeric DNA. Using telomerase activity assay, we confirmed that the purified dual-tagged dimer can extend telomeric DNA (Fig. 2A and fig. S5, A and B). This finding aligns with a previous study (*15*) but contrasts with another report that found no activity after tandem affinity purification of differentially tagged TERT (*20*). However, it is worth noting that the input lysate used by Errington *et al.* (*20*) was only 0.2% of what we used (Materials and methods; fig. S5A). Given the low abundance of the dimer, the activity in this previous study (*20*) was likely below the detection threshold of their telomerase activity assay, which explains the observed discrepancy with our results.

We next examined the DNA binding state of the catalytic core in the dimer structure. By applying symmetry, we obtained a reconstruction at 3.3-Å resolution for a catalytic core protomer in the context of the telomerase dimer (Fig. 2, B and C, and figs. S1E, S2, and S8, A to D). Consistent with our activity assay, a telomeric DNA substrate is bound in the active site of TERT (Fig. 2C; fig. S9, A and B; and table S2). Hence, our structure represents a functionally active dimer.

The proline/arginine/glycine-rich region of TERT is not involved in the dimerization of the telomerase holoenzyme

TERT consists of four domains: telomerase essential N-terminal (TEN) domain, telomerase RNA binding domain (TRBD), reverse transcriptase (RT), and C-terminal extension (CTE) (Fig. 2B). The TEN domain and TRBD are connected by a disordered proline/arginine/glycine-rich linker (PAL) (Fig. 2B). Previous studies showed that disrupting the PAL reduced dimerization of overexpressed TERT. However, once assembled into the telomerase RNP, the PAL mutant showed no defects in telomerase activity (*19*). In our dimer structure, we did not observe direct interactions between the two catalytic cores. The PAL regions of the two TERTs were unresolved owing to flexibility. To investigate whether the two PAL regions in our dimer structure may be interacting with each other, we tested the role of the PAL in telomerase dimer formation.

We reconstituted telomerase with ZZ-F-TERT and ZZ-SS-TERT, both lacking the PAL (ΔPAL). Following O-purification and Strep-Tactin pulldown, we assessed the copurification of ZZ-F-TERT in the Strep-Tactin elution (Fig. 1D and fig. S10A). We found that the level of ZZ-F-TERT in the ΔPAL mutant was slightly greater than that in the wild-type (WT) telomerase (fig. S10, B and C), suggesting that telomerase with the ΔPAL TERT can still dimerize. We also observed a notable increase in dyskerin levels in the ΔPAL mutant telomerase compared with the wild type (fig. S10, B and D). Dimerization of TERT protein through the PAL has been proposed to occur in hTR-free TERT or in inactive RNP (*19*). Another study described such inactive RNP with a morphology distinct from the dimer observed in this study (fig. S5G) (*8*). Removing the PAL may reduce this unproductive dimerization of TERT, thereby improving RNP assembly and explaining the increased levels of both ZZ-F-TERT and dyskerin observed in the ΔPAL mutant.

We also isolated the ΔPAL dimer using a three-step purification process (fig. S10E). The purified ΔPAL dimer remained catalytically active, consistent with previous findings that PAL is dispensable for telomerase activity (fig. S10F) (*19*). Negative stain EM 2D class averages of the ΔPAL dimer were similar to those of the WT dimer (fig. S10, G to I), further confirming that PAL deletion does not affect telomerase dimerization. Our results demonstrate that the PAL-mediated TERT dimerization is distinct from the dimerization of telomerase holoenzyme reported in this study and may occur at an earlier stage of telomerase assembly.

The two catalytic cores operate independently

Previous biochemical and kinetic studies proposed that the two active sites in a telomerase dimer act cooperatively or in tandem (*15*, *28*). To determine whether both catalytic cores can simultaneously bind to a DNA substrate, we performed signal subtraction to focus on each of the two catalytic cores individually (fig. S2). The best subsets of particles for the two catalytic cores yielded reconstructions at 3.6- and 3.8-Å resolution, showing clear densities for bound DNA substrates and TPP1 (Fig. 2D; figs. S8, E to L, and S9, C and D; and table S2).

A substantial proportion of particles in these two independently processed subsets originated from the same nonsubtracted dimeric particles. Reconstructions of the two catalytic cores from this common subset of particles showed clear density for the DNA in the active site of TERT (Fig. 2E). This demonstrates the presence of dimeric telomerase with both catalytic cores bound to separate telomeric DNA substrates. Given the independent engagement of DNA and the lack of interactions between the two catalytic cores, our structure does not explain the previously observed cooperativity between the two active sites.

To assess the potential cooperativity between the two catalytic cores in our telomerase dimer, we purified a dimer containing one WT TERT and one catalytically inactive TERT mutant (D712A/D868A/D869A) and compared its activity to that of a dimer with two WT TERTs (fig. S11, A and B). Telomerase activity was proportional to the amount of active TERT present, indicating no cooperativity between the catalytic cores (fig. S11, C and D). We obtained similar results in an independent experiment, where we used glycerol gradient centrifugation to separate the monomeric telomerase complex from the dimeric complex (fig. S12A). Telomerase activity of the gradient fractions correlated with TERT levels, and the dimer peak fraction did not show increased processivity compared with the monomeric fraction (fig. S12, B to D). Although additional factors may coordinate the two catalytic cores in cells, our structural and biochemical data suggest that the two catalytic cores function independently in vitro.

The P4.2 stem of hTR is critical for dimerization

The H/ACA domain of hTR exhibits a dual-hairpin structure, characteristic of RNAs within the H/ACA RNP family (Fig. 1, A and B) (*21*, *29*). Each RNA hairpin associates with four H/ACA proteins including dyskerin, NHP2, NOP10, and GAR1 (*30*). We refer to the H/ACA proteins as either the 5′ or 3′ heterotetramers, depending on whether they are bound to the 5′ or 3′ hairpin of hTR, respectively.

In telomerase, the H/ACA RNP is connected to the catalytic core through two linkers in hTR: the P1 linker, formed by the P1a stem, and the P4/5 linker, consisting of the P4.1, P4.2, and P5 stems (Figs. 1, A and B, and 3D, and fig. S7A). The P1 and P4/5 linkers of hTR were unresolved in previous high-resolution structures of telomerase owing to their flexibility (*9*, *10*, *22*). In our dimer structure, the two H/ACA RNPs pack against each other through an intricate network of protein-RNA and protein-protein interactions (Fig. 3, A to D), which rigidifies the RNA linkers in hTR. This limits the relative conformations between the lobes of each protomer (movie S1). Our dimer structure allowed for a detailed visualization of these RNA linkers and unveiled their role in telomerase dimerization, as described below (fig. S6, E, F, and K).

The P4/5 linker of hTR from one protomer binds to a cleft formed by the 5′ dyskerin, 5′ NOP10, and 5′ NHP2 of the other protomer (Fig. 3, E to H). The P4.2 stem is anchored by residues Lys^{121} and Arg^{122} of the 5′ NHP2 and further stabilized by other residues in the 5′ NHP2

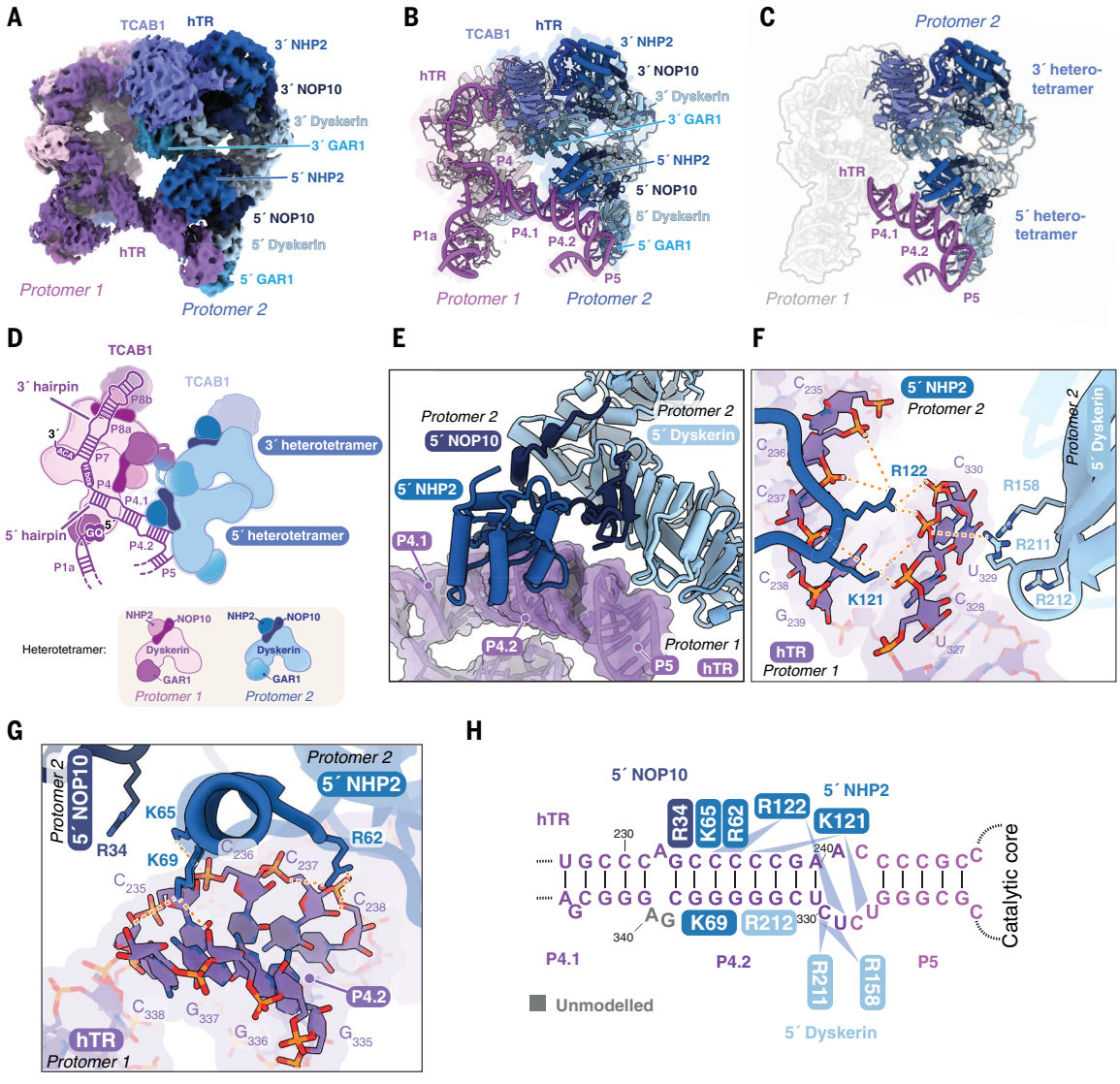

Fig. 3. Dimerization relies on interactions between the two H/ACA RNPs. (**A**) A 3.9-Å cryo-EM map of the H/ACA RNP dimer with individual protomers colored. Only subunits of protomer 2 (blue) and hTR of protomer 1 are labeled for simplicity. (**B** and **C**) A cartoon representation of the telomerase H/ACA RNP dimer model. In (C), only protomer 2 and the hTR P4/5 linker of protomer 1 are highlighted in colors. (**D**) Schematic of the H/ACA RNP dimer. (**E**) A close-up view of the interprotomer interactions between the hTR of protomer 1 and the 5′ H/ACA heterotetramer of protomer 2. The P4/5 linker interacts with the 5′ dyskerin, 5′ NHP2, and 5′ NOP10. (**F**) A close-up view of the interactions between the hTR P4.2/P5 junction of protomer 1 and the 5′ dyskerin and 5′ NHP2 of protomer 2. Single-letter abbreviations for the amino acid residues are as follows: A, Ala; C, Cys; D, Asp; E, Glu; F, Phe; G, Gly; H, His; I, Ile; K, Lys; L, Leu; M, Met; N, Asn; P, Pro; Q, Gln; R, Arg; S, Ser; T, Thr; V, Val; W, Trp; and Y, Tyr. (**G**) A close-up view of the interactions between the hTR P4.2 stem of protomer 1 and the 5′ NHP2 and 5′ NOP10 of protomer 2. (**H**) Schematic of the interactions between the P4/5 linker of hTR from protomer 1 and the 5′ H/ACA proteins of protomer 2.

(Arg^{62}, Lys^{65}, and Lys^{69}) and NOP10 (Arg^{34}) (Fig. 3, F to H). The junction between the P4.2 and P5 stems (nucleotides 327–330) also engages in backbone interactions with the 5′ dyskerin, specifically with residues Arg^{158}, Arg^{211}, and Arg^{212} (Fig. 3, F and H).

To validate these interprotomer protein-RNA interactions, we generated hTR mutants with disrupted base pairing in the P4.2 stem or perturbed P4.2/P5 junction (Fig. 4A and fig. S13). We reconstituted these mutants with a 1:1 mixture of ZZ-F-TERT and ZZ-SS-TERT, followed by O-purification and Strep-Tactin pulldown as described above (Fig. 1D). We probed for Flag-tagged TERT in the Strep-Tactin elution as a readout for dimer formation. Consistent with our structure, disrupting the base pairing of the P4.2 stem (P4.2 switch) severely reduced dimer formation (Fig. 4B and fig. S13). This defect was restored using a compensatory mutant (P4.2 comp.), where the two strands of P4.2 stem were swapped while maintaining base pairing (Fig. 4, A and B). Mutations at the P4.2/P5 junction (ΔU329, ΔUC329–330, and UC329–330GG) did not significantly reduce dimer formation (Fig. 4B). As the P4.2 stem forms the most extensive interactions with the 5′ H/ACA proteins (Fig. 3E), these results agree with our structure and demonstrate that the P4.2 stem of hTR is critical for dimer formation.

Disrupting dimerization impairs telomere maintenance in cells and assembly of active telomerase RNP

To investigate the impact of disrupting dimerization in cells, we used an hTR knockout HCT116 cell line, which exhibits critically short telomeres (*31*), and performed rescue experiments using either WT or mutant hTR (P4.2 switch, P4.2 comp., ΔU329, ΔUC329–330, and UC329–330GG). WT and mutant hTR were stably expressed in this

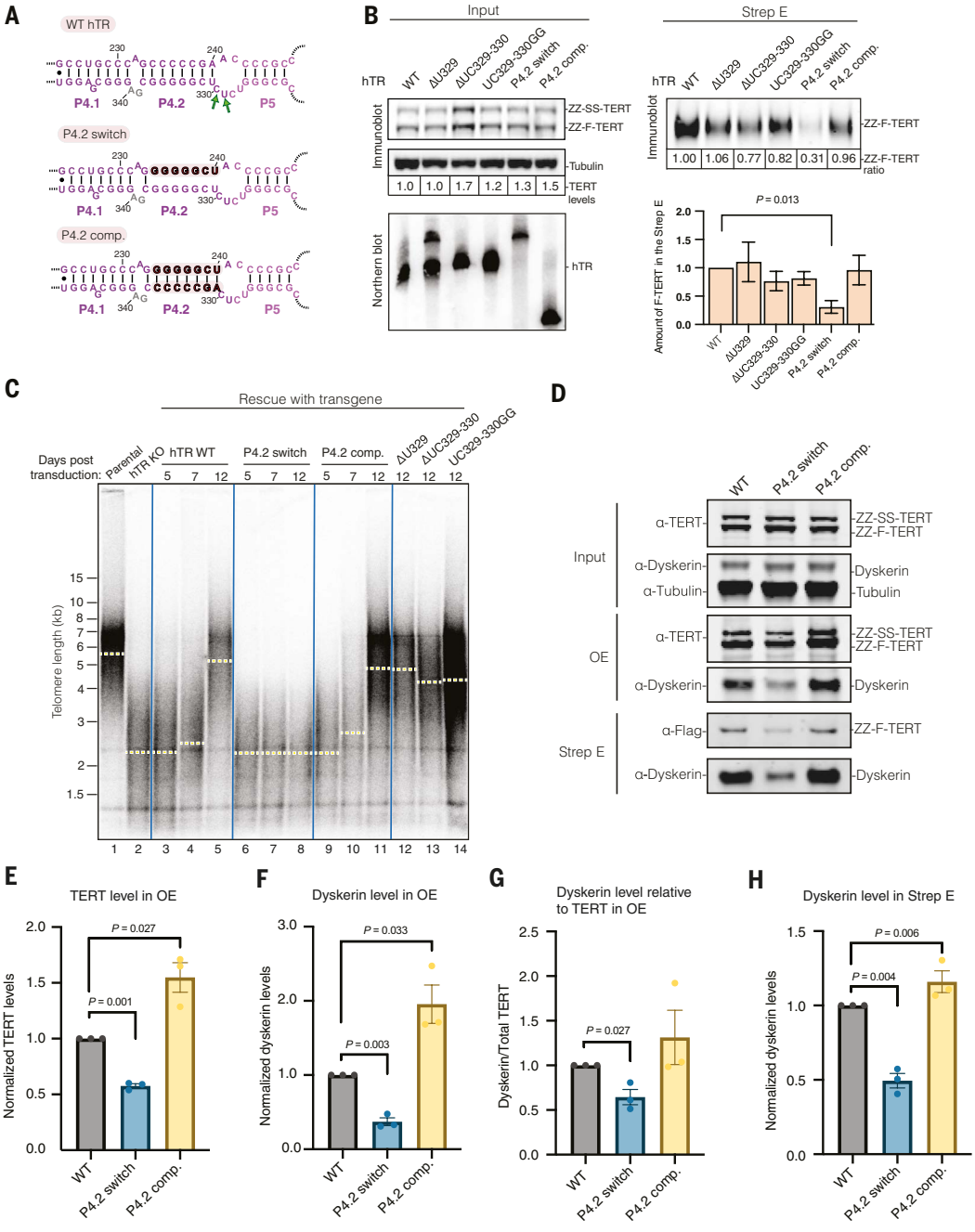

Fig. 4. Disrupting the P4.2 stem of hTR affects the binding of dyskerin and telomere maintenance in cells. (**A**) Schematic of WT hTR P4.2 stem, P4.2 switch, and P4.2 compensatory (P4.2 comp.) hTR mutants. Nucleotides 329 and 330 of hTR (highlighted in with green arrows) are also mutated in experiments shown in (B) and (C). Nucleotides mutated to create the P4.2 switch and P4.2 comp. mutants are shown in red. (**B**) Immunoblots and Northern blots of the human telomerase reconstituted with the ZZ-SS-TERT, ZZ-F-TERT, and the WT or mutant hTR. In the left panel, TERT levels in telomerase lysates (input) are normalized to tubulin levels. Telomerase was purified as described in Fig. 1D. The right panel depicts the immunoblot and corresponding quantification of the levels of the ZZ-F-TERT detected in the Strep elution (Strep E). ZZ-F-TERT levels in the Strep E of mutants are normalized to that in the WT sample. The bar graph represents the amount of ZZ-F-TERT in the Strep E assembled with the mutant hTR compared with the WT hTR. Experiments were performed in triplicate ($n = 3$). Error bars represent the standard error of the mean (SEM), and significant P value is reported for the P4.2 switch hTR mutant. See fig. S13 for the replicate data. (**C**) Telomere restriction fragment (TRF) assay of HCT116 hTR knockout (KO) cell lines transduced with either WT or mutant hTR from (A). Lanes 1 and 2 show telomere lengths of the parental HCT116 and the KO cell lines, respectively. Lanes 3 to 14 show telomere lengths of KO cells that were rescued with various hTR transgene constructs. Yellow dashed lines indicate the mean telomere length for each lane. (**D**) Immunoblots of the input lysates (input), OE, and Strep E to dissect the effects of disrupting P4.2 stem of hTR. Each of hTR constructs, either WT or P4.2 switch or P4.2 comp. mutant, was reconstituted with a mixture of ZZ-SS-TERT and ZZ-F-TERT (fig. S14A). Telomerase was purified by O-purification and Strep-Tactin pulldown, as shown in fig. S14A. Experiments were performed in triplicate ($n = 3$). See fig. S14B for replicate data. (**E**) Bar graph showing the levels of TERT in the OE of WT hTR and P4.2 switch and P4.2 comp. mutants. (**F**) Bar graph showing the levels of dyskerin in the OE of WT hTR and P4.2 switch and P4.2 comp. mutants. (**G**) Bar graph showing the levels of dyskerin relative to TERT in the OE of WT hTR and P4.2 switch and P4.2 comp. mutants. Together with the graphs shown in (E) and (F), this graph shows that in the OE, dyskerin levels in the P4.2 switch hTR mutant were more severely reduced than TERT compared with the WT hTR. (**H**) Bar graph showing the levels of dyskerin in the Strep E of WT hTR and P4.2 switch and P4.2 comp. mutants. In the quantification shown in (E) to (H), TERT or dyskerin levels of the mutants were normalized to those of the WT hTR. Error bars in (E) to (H) represent SEM, and significant P values are also reported.

cell line by transgene integration at the adeno-associated virus integration site 1 (AAVS1) safe-harbor locus (*31*). Without transgene expression, telomere restriction fragment (TRF) analysis showed that the hTR knockout cells exhibit telomere shortening and eventually undergo cell death (Fig. 4C, lanes 1 and 2). Expression of the WT hTR efficiently rescued telomere shortening, restoring the telomere length to parental levels (Fig. 4C, lanes 1 and 3 to 5), whereas the P4.2 switch mutant did not (Fig. 4C, lanes 6 to 8). In contrast, the P4.2 compensatory mutant restored telomere length to a similar level as the WT hTR (Fig. 4C, lanes 9 to 11). Mutations in the P4.2/P5 junction, which did not substantially affect dimer formation, also rescued telomere shortening but to a lesser extent than WT hTR (Fig. 4C, lanes 12 to 14). These results validate our structural and biochemical work and suggest that human telomerase dimerization is important for telomere maintenance in cells.

We next sought to determine the functional role of telomerase dimerization. We first examined the effect of disrupting dimerization on telomerase activity. Although the P4.2 stem of hTR is distant from the telomerase active site, telomerase activity was severely impaired in the P4.2 switch mutant (fig. S13). Restoring base pairing within the P4.2 stem rescued the activity defects, as shown in the P4.2 comp. mutant (fig. S13). Given that the telomerase dimer is a minor population in our sample, the bulk activity observed likely corresponds to that of the more abundant monomeric complex. Our data suggest that disrupting dimerization affects the activity of the monomeric complex and imply that the dimer may be a biogenesis precursor of the monomer. Therefore, we hypothesized that dimerization may have a role in telomerase assembly.

To test this hypothesis, we examined the impact of disrupting P4.2 stem on hTR interaction with TERT and dyskerin. We reconstituted either WT hTR or the P4.2 mutant (either switch or comp.) with ZZ-F-TERT and ZZ-SS-TERT, as described above (Fig. 4, B and D, and fig. S14A). Following the O-purification through hTR, we compared the levels of TERT and dyskerin in the OE fractions of the WT hTR and the two P4.2 hTR mutants (Fig. 4D and fig. S14, A and B; OE fractions). The P4.2 switch hTR mutant efficiently pulled down TERT, but with ~40% less efficiency compared with WT hTR (Fig. 4, D and E). However, the dyskerin level associated with the P4.2 switch mutant was more significantly reduced than TERT (Fig. 4, D to G). A similar trend was also observed in the second Strep-Tactin purification (Fig. 4, D and H; Strep E fraction). In contrast, the P4.2 comp. hTR mutant rescued the defects in both TERT and dyskerin binding (Fig. 4, D to H). These results are consistent with the cross-protomer interaction between the P4.2 stem of hTR and the 5′ dyskerin in our dimer structure (Fig. 3, A to E).

Given the close proximity of the P4.2 stem to the activity-essential CR4/5 domain of hTR, we examined the folding of the P4.2 stem and the CR4/5 region in the WT hTR and the P4.2 switch and comp. hTR mutants. We reconstituted ZZ-SS-TERT with either P4.2 switch or comp. hTR mutants, followed by O-purification and Strep-Tactin pull-down, which would yield mostly monomeric telomerase RNP (fig. S15A). To assess RNA structural integrity, we conducted RNA dimethyl sulfate (DMS) chemical probing experiments on purified P4.2 switch and comp. mutants, comparing their reactivities to WT hTR (fig. S15E). In the WT hTR, the P4.2 stem region exhibited low DMS reactivities, indicating stable base pairing in this region (fig. S15E). In contrast, the P4.2 switch hTR mutant displayed high DMS reactivities across the P4.2 stem region, suggesting stem disruption (fig. S15E). In the P4.2 comp. mutant, DMS reactivities were low across the stem region (fig. S15E), confirming the restoration of base pairing. Moreover, the P4.2 switch mutant showed relatively similar DMS reactivities across the CR4/5 region compared with the WT hTR, suggesting that disrupting the P4.2 stem did not cause global misfolding of the CR4/5 region (fig. S15E). Therefore, the RNA DMS chemical probing results generally agree with our structural design.

Negative stain EM of the purified P4.2 switch and P4.2 comp. mutants showed that both still formed monomeric telomerase RNPs similar to the wild type (figs. S1F and S16, A to F). However, compared with the P4.2 comp. mutant, the P4.2 switch mutant produced fewer assembled telomerase particles relative to the total particle count (fig. S16, A to D). Additionally, the purified P4.2 switch mutant exhibited a marked decrease in telomerase activity per TERT and reduced dyskerin levels relative to TERT (fig. S15, B to D). Collectively, these findings indicate that although the P4.2 switch mutant can still bind TERT, many of the resulting TERT-hTR complexes lack dyskerin and are inactive, pointing to an assembly defect.

Cross-protomer interactions are important for the assembly of H/ACA proteins with hTR

Many premature aging disease mutations in the H/ACA proteins have been shown to affect telomerase assembly (*8*, *9*, *27*). We previously mapped most of the disease mutations to the interface between the two dyskerin molecules in the H/ACA RNP of human telomerase (Fig. 5A) (*27*). The 5′ H/ACA RNA hairpin of hTR is shorter than in canonical H/ACA RNAs, leading to a weaker association with the 5′ H/ACA heterotetramer compared with a canonical H/ACA hairpin (Fig. 1, A and B) (*8*, *9*, *21*, *27*, *32*). The mutations at the dyskerin-dyskerin interface compromise the assembly of the 5′ heterotetramer and, consequently, telomerase assembly, leading to telomerase deficiency (*8*, *9*, *21*, *27*). A cluster of previously unaccounted disease mutations in hTR, NOP10, NHP2, and dyskerin is located at the dimerization interface between the 5′ H/ACA proteins and the P4/5 linker of hTR (Fig. 5, A and B). In particular, NOP10 R34 and dyskerin R158 directly interact with the P4/5 linker (Fig. 3, F to H). NOP10 R34W has been shown to impair pre-RNP assembly (*33*). This suggests that these disease mutations may affect the assembly of the 5′ H/ACA proteins by disrupting their interaction between the P4.2 stem at the dimerization interface.

To test the role of dimerization in telomerase assembly, we mutated key residues in H/ACA proteins that are involved in interaction with the P4.2 stem (Figs. 3, F to H, and 5, C and D, and figs. S17 and S18, A and C). Our telomerase reconstitution was supplemented with either overexpressed 3xFlag-tagged WT or mutant H/ACA proteins. Our telomerase reconstitution relies on assembly of hTR with the endogenous H/ACA proteins (*34*). Assembly defects can be assessed by comparing the relative incorporation levels of the overexpressed proteins to those of the endogenous proteins (*27*). We purified telomerase using O-purification on hTR and performed immunoblots against dyskerin or NHP2. Because they are present in vast excess relative to the endogenous proteins, overexpressed WT dyskerin and NHP2 efficiently outcompeted their endogenous counterparts for assembly into telomerase (Fig. 5, C and D). In contrast, three dyskerin mutants (R211D/R212D, R158W/R211A/R212A, and R158W/R211D/R212D) and both NHP2 mutants (K121A/R122A and K121D/R122D) were less efficient in competing with endogenous dyskerin and NHP2, respectively, for incorporation into telomerase (Fig. 5, C to F). The dyskerin R158W and R211A/R212A mutants showed slight but significant defects in their abilities to compete with the endogenous dyskerin for telomerase incorporation (Fig. 5, C and E). Thus, our data indicate that these mutant H/ACA proteins are defective in telomerase incorporation. Notably, the level of TERT being assembled with hTR was greatly reduced for the dyskerin triple mutant R158W/R211D/R212D (Fig. 5C). This observation suggests that disrupted dimerization can compromise hTR assembly with TERT.

To rule out the possibility that the dyskerin and NHP2 mutations selected above may affect the assembly of the 3′ H/ACA proteins, we examined the equivalent residues in the 3′ dyskerin and 3′ NHP2. R158, R211, and R212 in the 3′ dyskerin are not involved in any protein-protein or protein-RNA interactions (figs. S18A and S19, A and B). Although K121 and R122 in the 3′ NHP2 interact with TCAB1 and hTR backbone, respectively, they are not conserved across archaea and

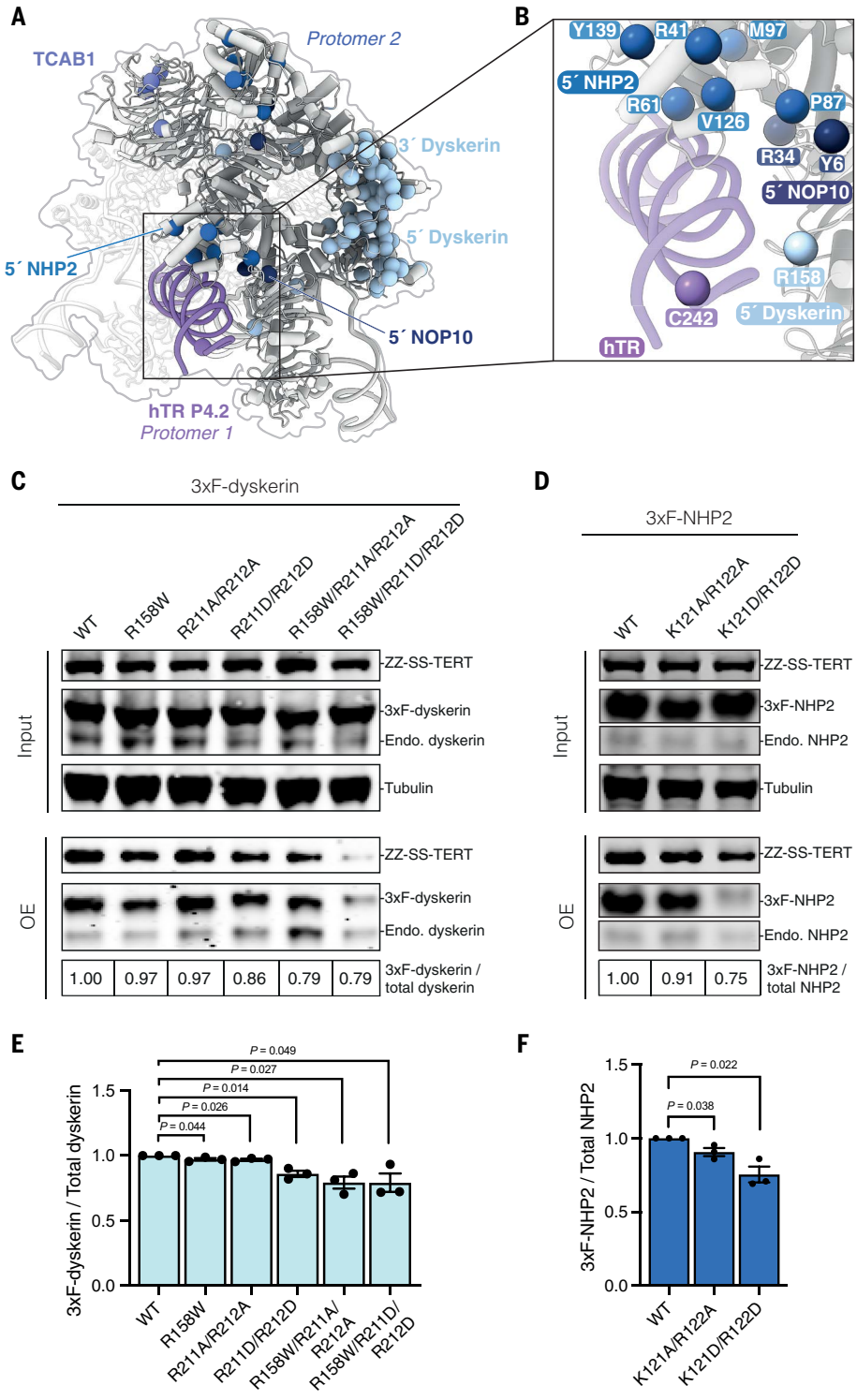

Fig. 5. Dimerization plays a role in telomerase assembly. (**A**) Disease mutation mapping of the H/ACA proteins and hTR onto the model of the H/ACA RNP dimer (*6*,*53*). Disease mutations are represented as spheres. (**B**) Inset showing a close-up view of the interface between the hTR P4.2 stem of protomer 1 and the H/ACA proteins of protomer 2 with the disease mutations at this interface. (**C**) Immunoblots of cell lysates (input) and OE from cells transfected with ZZ-SS-TERT, hTR, and WT or mutant 3xF-dyskerin. The total dyskerin levels in the OE were calculated as 3xF-dyskerin plus endogenous dyskerin. Mutant 3xF-dyskerin levels over total dyskerin were normalized to the WT sample. (**D**) Immunoblots of cell lysates and OE from cells transfected with ZZ-SS-TERT, hTR, and either WT or mutant 3xF-NHP2. Analysis and quantification are the same as for (C). (**E**) Bar graph showing the levels of 3xF-dyskerin over the total amount of dyskerin in the OE samples from (C). (**F**) Bar graph showing the levels of 3xF-NHP2 over the total amount of NHP2 in the OE samples from (D). Experiments in (C) and (D) were performed in triplicate ($n = 3$). See fig. S17 for the replicate data. Error bars in (E) and (F) represent SEM, and significant *P* values are reported.

eukaryotes (figs. S18C and S19, C and D). These interactions have been suggested to enhance the affinity of the 3′ H/ACA heterotetramer for the 3′ H/ACA hairpin of hTR but are likely not crucial for the assembly of the 3′ hairpin (*8*, *9*, *32*). We did not mutate residues R62, K65, and K69 of NHP2, despite their involvement in dimerization (Fig. 3, G and H). These three residues are part of a highly conserved RNA binding surface essential for the interaction of the 3′ NHP2 with the 3′ RNA hairpin (figs. S18C and S19, C and D). Mutating these residues would affect the assembly of the 3′ heterotetramer and thus telomerase assembly, independent of dimerization. Therefore, the telomerase assembly defects of the dyskerin and NHP2 mutants described above would reflect disruption of dimerization (Fig. 5, C to F). Taken together, our structure and biochemical data not only rationalize a cluster of disease mutations in the H/ACA RNP but also suggest that dimerization has a functional role in telomerase assembly.

The N-terminal RG domains of the two 3′ GAR1 molecules also promote dimerization

GAR1 is composed of a β barrel domain, flanked on both sides by low-complexity arginine-glycine (RG)–rich domains (fig. S18B) (*9*, *10*, *27*). In our dimer structure, we observe clear density corresponding to the two N-terminal RG domains of the two 3′ GAR1, one from each protomer. Both N-terminal RG domains protrude from the GAR1 β barrel domain to intertwine with each other (Fig. 6, A to D). However, owing to the disordered nature of RG domains, this density does not show high-resolution features sufficient for de novo model building (Fig. 6B). RG domains have been implicated in RNA binding and in promoting phase separation in the assembly of membraneless organelles (*35*). Among the reported telomerase H/ACA RNP structures, only the N-terminal RG domain of the 5′ GAR1 has been partially resolved and found to stabilize an RNA hairpin formed by the 5′ leader sequence of hTR (nucleotides 1–17) (Fig. 1A) (*10*). In our structure, the intertwined N-terminal RG domains of the two 3′ GAR1 make contacts with the P7b stems of the two hTRs (Fig. 6, C and D). Thus, our structure suggests an unexpected contribution for the N-terminal RG domain of the 3′ GAR1 in telomerase dimerization and provides structural evidence affirming its RNA binding capacity.

The 5′ GAR1 interacts with the 5′ G-quadruplex of hTR and the histone dimer

The 5′ region of hTR (nucleotides 1–31) contains multiple guanosine (G) tracts capable of forming G-quadruplexes, which are four-stranded

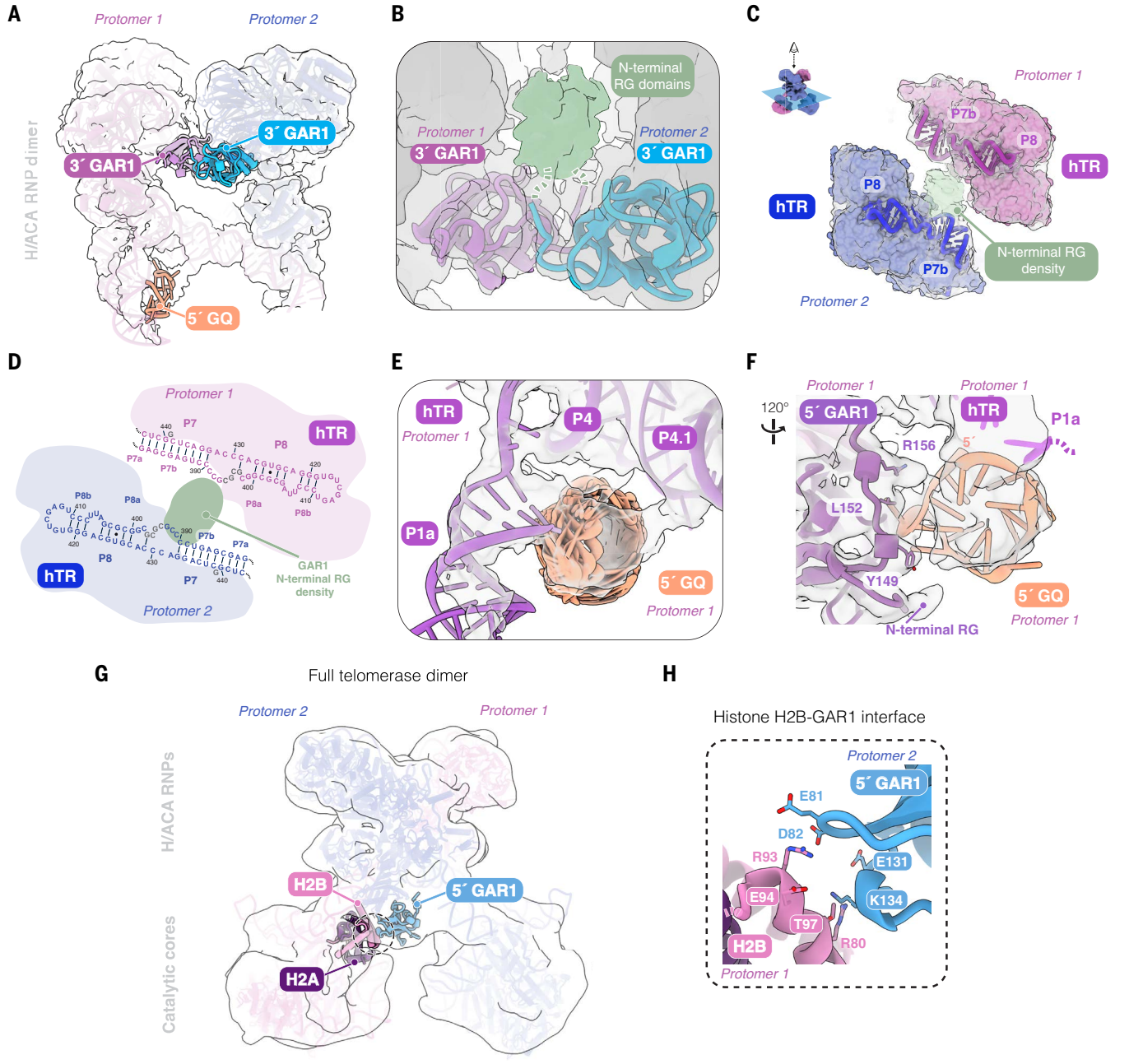

Fig. 6. GAR1 role in telomerase dimerization. (**A**) Consensus cryo-EM density of the H/ACA RNP dimer with the 5′ G-quadruplex (GQ), the 3′ GAR1 from protomer 1, and the 3′ GAR1 of protomer 2 fitted into the density. (**B**) Interaction between the 3′ GAR1 subunits of the H/ACA RNP protomers 1 and 2 within the 3.9-Å H/ACA RNP dimer map. Although the density for the N-terminal arginine-glycine (RG)–rich domains of both protomers is clear, they do not appear to have defined structures for model building. The dashed lines and the green cryo-EM density represent the predicted positioning of the N-terminal RG domains of the 3′ GAR1 subunits. (**C**) The density of the N-terminal RG domains of the two 3′ GAR1 subunits reaching toward the hTR P7b stem of both H/ACA RNP protomers. (**D**) Schematic of the two P7b stems of hTR within the dimer and their contact with the N-terminal RG domains of the 3′ GAR1. (**E**) A 3.9-Å cryo-EM H/ACA RNP dimer map with fitted ensemble of the 5′ GQ conformations, modeled by DRRAFTER (*26*). (**F**) A close-up view of the 5′ GQ interaction with the 5′ GAR1 within protomer 1. The same interaction is formed between the 5′ GQ and the 5′ GAR1 of protomer 2. (**G**) Consensus cryo-EM density of the full telomerase dimer with histone H2A-H2B dimer from protomer 1 and the 5′ GAR1 of protomer 2 fitted into the density. (**H**) A close-up view showing the interface between the histone H2B of protomer 1 and the 5′ GAR1 of protomer 2.

secondary structures formed by the Hoogsteen base pairing of four guanine residues (*36*, *37*). By protecting hTR from degradation, G-quadruplex formation is important for telomerase biogenesis and mature hTR accumulation in cells (*37*–*39*). In mature telomerase, part of the 5′ G-tracts (nucleotides 18–30) forms the P1a linker (Fig. 1, A and B). The rest of the 5′ region (nucleotides 1–17), also known as the 5′ leader sequence, is assumed to be single-stranded (Fig. 1A) (*40*). However, it has been demonstrated to form a G-quadruplex in vitro (*37*, *41*), but this G-quadruplex structure has not been detected in vivo or visualized in any reported telomerase structures (*9*, *10*, *22*, *23*, *27*). Wan *et al.* observed that this region forms a stem loop instead (*10*). Moreover, conflicting suggestions have been made regarding whether this 5′ G-quadruplex is mutually exclusive with P1a formation (*36*, *41*).

The stabilization of the P1 linker by dimerization enabled us to resolve the P1a stem and an adjacent density consistent with a 5′ G-quadruplex for the 5′ leader sequence (Materials and methods; fig. S20 and data S2). Thus, our work provides structural evidence for G-quadruplex formation in human telomerase. Because of the limited local resolution of this region (~7 Å), we used DRRAFTER to model an ensemble of G-quadruplex structures in the cryo-EM density (Fig. 6E and data S3). Our structure confirms that the 5′ G-quadruplex structure can coexist with the P1a stem. This is consistent with a previous finding, which showed a low-level association of the G-quadruplex helicase DHX36 with active telomerase RNP (*38*). Although we do not observe density for DHX36 in our dimer reconstructions, endogenous DHX36 was consistently detected by mass spectrometry in purified telomerase samples (*8*, *9*).

The 5′ G-quadruplex packs against P4 and P4.1 stems of hTR (Fig. 6E). Consistent with our structure, the interaction between the 5′ leader sequence and P4.1 stem has been previously observed using gel-shift assays (*37*). The G-quadruplex is also stabilized by the 5′ GAR1 within a single protomer (Fig. 6F), revealing another mode of RNA binding by GAR1. Our observation is supported by a recent study, which demonstrates that GAR1 interacts with G-quadruplex RNAs both in living cells and in vitro (*42*).

Besides interacting with the G-quadruplex, the 5′ GAR1 also contacts the histone H2B in the catalytic core of the other protomer (Fig. 6G). Although the resolution of the dimer consensus map precludes precise determination of these interactions, several residues in histone H2B and GAR1 can potentially form electrostatic interactions at this interface (Fig. 6H). In all previous structures of the telomerase monomer, both the 5′ and 3′ GAR1 associate with the H/ACA RNP solely through well-characterized interactions with dyskerin (*9*, *10*, *22*, *23*, *27*). Hence, our telomerase dimer structure unveils additional interactions between GAR1 and other telomerase components.

Discussion

In this study, we uncovered the structure of a low-abundance human telomerase dimer by leveraging the large cryo-EM dataset collected on human telomerase. Our work reconciles a long-standing debate regarding the TERT-hTR stoichiometry in human telomerase and provides insights into the molecular interactions crucial for dimerization and the potential roles of the telomerase dimer in telomere maintenance.

The 1.2-MDa human telomerase dimer resolved here is a dimer of the full holoenzyme rather than a dimer of TERT, hTR, and dyskerin, as previously suggested (*16*). The reported 30-Å negative stain EM structure of a 600-kDa human telomerase complex, suggested to be dimeric, strongly resembles the cryo-EM structures of the monomeric telomerase RNP and differs from the telomerase dimer presented in this study (fig. S1F) (*8*, *9*, *17*). The previously identified 600-kDa human telomerase complex likely has a monomeric TERT-hTR composition with all the holoenzyme components (*14*–*17*). Therefore, our work not only resolves the ambiguity in the composition of the 600-kDa human telomerase complex but also reveals a dimeric telomerase complex, which has not been previously visualized.

Our data present several lines of evidence indicating a role for dimerization in telomerase assembly. First, dimerization is mostly mediated by the H/ACA RNP, which is involved in telomerase biogenesis and accumulation (*11*, *32*). Second, several dyskeratosis congenita disease mutations in the 5′ H/ACA proteins and hTR are located at key dimerization interfaces (Fig. 5, A and B). Third, disruption of dimerization leads to defects in telomere maintenance in cells and incorporation of the H/ACA proteins into telomerase (Figs. 4, C to H, and 5, C to F). We propose that dimerization promotes telomerase assembly by stabilizing the suboptimal binding of the 5′ H/ACA heterotetramer to the 5′ H/ACA hairpin of hTR during assembly (Fig. 3, B to D). Given the presence of all accessory factors, the dimer would represent an assembly intermediate that is close to RNP maturation. This proposed role of the dimer would account for the low abundance of the dimer in our sample and the telomerase activity defects resulting from disrupting dimerization. The requirement to pass through a dimeric state during assembly is reminiscent of the HIV RT. The homodimer of the catalytic p66 subunit of HIV RT serves as an immediate precursor to the mature p66/p51 heterodimer, in which one p66 protomer is converted into the p51 subunit by proteolytic cleavage (*43*). Like our telomerase dimer, the p66 homodimer also exhibits enzymatic activity (*44*, *45*).

Although both the P4.2 stem and the P4.2/P5 junction (nucleotides 329 and 330) of hTR are involved in dimerization, disrupting the P4.2/P5 junction did not significantly affect dimer formation (Fig. 4B and fig. S13). Notably, nucleotides 327–329 within this junction are known to participate in triplex formation with the H-box and a region downstream of the mature 3′ end of hTR during early telomerase assembly (*46*). During this process, the binding of the H/ACA proteins disrupts the triplex, enabling 3′ end processing of hTR and promoting efficient telomerase assembly. The mutations we introduced in the P4.2/P5 junction likely partially destabilize this triplex, potentially enhancing telomerase assembly. This improved assembly could counterbalance the downstream effects of impaired dimerization, which may explain why we did not observe a substantial effect on dimer formation in P4.2/P5 junction mutants.

The interaction between the 5′ GAR1 and the 5′ G-quadruplex of hTR may also play a role in telomerase maturation. GAR1 has been identified as a G-quadruplex ligand sensitizing gene (*47*). In the absence of GAR1, the G-quadruplex is more susceptible to stabilization by small molecules. This implies that GAR1 interaction might contribute to resolving the G-quadruplex rather than stabilizing it. The unwinding of the G-quadruplex may happen during telomerase maturation, explaining its potential absence in the previous telomerase monomer structure (*9*).

Residue Lys^{134} of GAR1, which faces histone H2B in the dimer structure (Fig. 6H), has been reported to be SUMOylated in a previous proteomic study (*48*). Arginine methylation of the N-terminal RG domain of GAR1 has also been identified (*49*). Such posttranslational modifications would perturb the dimerization interface, potentially providing a mechanism to convert the dimer to the monomer.

Given that the dimer is catalytically active (Fig. 2A), we cannot exclude the possibility that dimerization also has a role in telomere extension. One model suggests that a telomerase dimer, with two active sites, could extend either two telomeres simultaneously or a single telomere cooperatively (*15*, *28*). Our in vitro data, which show that the two catalytic cores operate independently, are more consistent with the former mechanism. However, substantial evidence indicates that the catalytic activity of human telomerase requires only a single TERT and hTR (*18*–*20*). Although live-cell imaging of human telomerase cannot infer its oligomeric state because of the substoichiometric labeling of TERT, the observed diffusion coefficient of TERT-containing particles in cells is consistent with a molecular mass of 600 kDa (*50*). As discussed earlier, this 600-kDa species likely corresponds to the monomeric holoenzyme. Telomerase holoenzymes from unicellular eukaryotes are also unequivocally monomeric for TERT and TERs (*51*, *52*). Furthermore, the P4.2 stem of hTR, which is critical for dimerization, is highly variable in sequence and length among vertebrates (*40*). TERs from some fish species lack this stem altogether (*53*). These observations suggest that dimerization is not a conserved feature of telomerase and, from an evolutionary perspective, would argue against a general role for the dimer in telomere extension.

Our work unveils the architectural diversity of human telomerase and provides an invaluable platform for further studies of telomerase modulation, assembly, and function in the dimer context. The identification of the dimeric state and its functional role could have broad implications for telomere-related diseases and therapeutic strategies.

Materials and methods

Expression of human telomerase

Human telomerase was reconstituted in Expi293F cells (Thermo Fisher, Cat# A14527) by cotransfection with pcDNA3.1-ZZ-TEV-twin-Strep-SUMO*-TERT and pcDNA3.1-U3-hTR-HDV (*8*, *32*). TEV is the tobacco etch virus protease cleavage site, SUMO* is the SUMOstar protease cleavage site (LifeSensors, Cat# SP4110), and HDV is the hepatitis delta virus ribozyme. Whole-cell extracts were prepared by three hypotonic freeze-thaw cycles, snap-frozen in liquid nitrogen, and stored at −70°C until used.

Reconstitution of human telomerase with DNA and TPP1-POT1-TIN2 (TPT)

Telomerase lysates were incubated with streptavidin agarose resin (Thermo Fisher, Cat# 20361), prebound to a 5′ biotinylated 2′-*O*-methyl oligonucleotide for 3 hours at room temperature. After washing the resin with wash buffer [20 mM HEPES NaOH pH 8.0, 150 mM NaCl, 2 mM $MgCl_2$, 0.2 mM EGTA, 10% glycerol, 0.1% IGEPAL CA-630, 1 mM dithiothreitol (DTT), and 0.2 mM phenylmethylsulfonyl fluoride (PMSF)], sample was eluted with a competitor oligonucleotide (sequence: CTAACCCTAACTGATGACAGGTCTAGddC, where ddC stands for dideoxycytosine). Next, MagStrepXT resin (IBA LifeSciences, Cat# 2-4090-002) was added to the eluate and incubated for 2 hours at 4°C. The resulting resin was washed three times with wash buffer and then incubated with 10 μM telomerase DNA primer [either $(TTAGGG)_5$ or $(TTAGGG)_5TTA$ and 100 μM dGpCpp, a nonhydrolyzable analog of dGTP, (Jena Bioscience, Cat# NU-431S)] for 45 min at room temperature. After washing, purified TPP1-POT1-TIN2 (TPT) was added to the resin at a final concentration of 0.15 mg/ml in 1 column volume (CV) of MagStrepXT beads and incubated for 1 hour at 4°C. TPT was expressed in *Spodoptera frugiperda* (Sf9) (Sf9, Oxford Expression Technologies Ltd, Cat# 600100) and purified as previously described (*23*). Complexes were eluted from the resin by overnight cleavage with SUMOstar protease (LifeSensors, Cat# SP4110) at 4°C. Fractions were analyzed on the SDS-PAGE gel followed by silver staining (Invitrogen Cat# LC6070).

Cloning of mutant hTR, TERT, dyskerin, and NHP2

Mutant constructs were generated as described previously (*23*). Briefly, we used NEBaseChanger to design mutagenesis primers (see table S3). Mutants of pcDNA3.1-U3-hTR-HDV, pcDNA 3.1 ZZ-TEV-twin-Strep-SUMO*-TERTΔPAL, pcDNA3.1-ZZ-TEV-3xFlag-TERTΔPAL, pcDNA3.1-3xFlag-dyskerin (Addgene, Plasmid# 126870), or pcDNA3.1-3xFlag-NHP2 (Addgene, Plasmid# 126871) (*21*, *32*) were generated using NEB Q5 Site-Directed Mutagenesis Kit (NEB, Cat# E0554). Catalytically dead mutants pcDNA3.1-ZZ-TEV-twin-Strep-SUMO*-TERT D712A/D868A/D869A and pcDNA3.1-ZZ-TEV-3xFlag-TERT D712A/D868A/D869A were generated by QuikChange site-directed mutagenesis. SmBiT and LgBiT luciferase fragment constructs were amplified from plasmids kindly provided by L. James's laboratory and inserted at the N terminus of pcDNA3.1-ZZ-TEV-twin Strep-SUMO*-TERT and pcDNA3.1-ZZ-TEV-3xFlag-TERT. Correct mutations and cloned constructs were confirmed by DNA sequencing, and plasmid stocks for transfection were prepared using PureLink HiPure plasmid midiprep kit (Invitrogen, Cat# K210005).

Telomerase activity assays

Telomerase primer extension assays were performed in 50 mM Tris-acetate pH 8.0, 4 mM $MgCl_2$, 250 μM deoxythymidine triphosphate (dTTP), 250 μM deoxyadenosine triphosphate (dATP), 5 μM unlabeled deoxyguanosine triphosphate (dGTP), 0.1 μM α-^{32}P-dGTP (3000 Ci/mmol, 10 mCi/ml) (Hartmann Analytic Gmbh, Cat# FP204), 500 nM $(TTAGGG)_5$, and 5 mM DTT. Reactions were carried out at 30°C for 45 min and stopped with 50 mM Tris HCl pH 7.5, 20 mM EDTA, and 0.2% SDS. Following nucleic acid extraction with phenol:chloroform:isoamyl alcohol (25:24:1) (Thermo Scientific, Cat# 17908), sample was precipitated using ethanol with a ^{32}P-labeled 24-nucleotide DNA as a recovery control (RC). The primer extension products were run on a 10.5% denaturing polyacrylamide (19:1) Tris-borate-EDTA (TBE) gel at 500 V for 2 hours and 15 min. The gel was subsequently dried at 80°C for 60 min and exposed to a phosphorimager screen overnight. The screen was scanned by an Amersham Typhoon Biomolecular Imager (Cytiva) and quantified using ImageQuant (Cytiva).

Expression and purification of the dual-tagged telomerase

Human telomerase with two tags was reconstituted in Expi293F cells (Thermo Fisher, Cat# A14527) by cotransfection with pcDNA3.1-ZZ-TEV-twin-Strep-SUMO*-TERT, pcDNA3.1-ZZ-TEV-3xFlag-TERT, and pcDNA3.1-U3-hTR-HDV. Whole-cell extracts were prepared by three hypotonic freeze-thaw cycles. Telomerase lysates underwent 2′-*O*-methyl oligonucleotide purification to yield OE as described above. DYKDDDK Fab-Trap Agarose resin (Chromotek, Cat# ffa) was added to the eluate and incubated overnight at 4°C. After washing with wash buffer, the sample was eluted off the beads with 0.5 mg/ml Flag peptide (Thermo Fisher, Cat# A36805). Next, the Flag eluate was incubated with MagStrepXT resin (IBA LifeSciences, Cat# 2-4090-002) for 2 hours at 4°C. The resulting resin was washed three times with wash buffer. The sample was eluted from the resin by overnight cleavage with SUMOstar protease (LifeSensors, Cat# SP4110) at 4°C. Fractions were analyzed by negative staining and telomerase activity assays. Purifications of the dual-tagged WT dimer (168 ml of input lysate from 1 liter of cell suspension; fig. S5A), the ΔPAL dimer (168 ml of input lysate from 1.2 liters of cell suspension; fig. S10E), and the dimer with one copy of WT TERT and one copy of the catalytically inactive TERT (196 ml of input lysate from 1.5 liters of cell suspension; fig. S11A) were performed using the method described in this section.

Expression and purification of single-tagged human telomerase with the P4.2 switch and P4.2 comp. hTR mutants

Human telomerase was expressed in Expi293F cells (Thermo Fisher, Cat# A14527) by cotransfection with pcDNA3.1-ZZ-TEV-twin-Strep-SUMO*-TERT and pcDNA3.1-U3-hTR-HDV harboring either the P4.2 switch (P4.2 switch) or compensatory (P4.2 comp.) mutations (see table S3). Cell lysates were prepared by three hypotonic freeze-thaw cycles, snap-frozen in liquid nitrogen, and stored at −70°C until used. Lysates (84 ml from 500 ml of cell suspension) were subjected to 2′-*O*-methyl oligonucleotide purification by incubation with streptavidin agarose resin (Thermo Scientific, Cat# 20361), prebound to a 5′ biotinylated 2′-*O*-methyl oligonucleotide, as described above. MagStrepXT resin (IBA LifeSciences, Cat# 2-4090-002) was added to the oligo purification eluate and incubated for 2 hours at 4°C. The resin was washed three times with wash buffer. Telomerase was eluted by overnight cleavage with SUMOstar protease (LifeSensors, Cat# SP4110) at 4°C. The final elution sample was analyzed by immunoblotting, activity assay, DMS chemical probing and negative stain EM (figs. S15 and S16).

Split nanoluciferase assay

Human embryonic kidney (HEK) 293T cells (ATCC, Cat# CRL-3216, RRID:CVCL_0063) were grown in Dulbecco's modified Eagle's medium (DMEM) with GlutaMax (Thermo Fisher, Cat# 10566016), supplemented with 10% fetal bovine serum (FBS), 100 μg/ml streptomycin, and 100 units/ml penicillin. Cells were seeded at an approximate density of 20,000 cells per well in a 96-well plate (Greiner, Cat# 655098). After 24 hours, cells were cotransfected with pcDNA3.1-U3-hTR-HDV, and two pcDNA3.1-TERT plasmids, one containing the SmBiT and the other containing the LgBiT, with a total of 300 ng DNA used per well (fig. S4). In each transfection combination, one TERT was Flag-tagged, and the other was twin-Strep-tagged. Transfection was performed with

Lipofectamine 3000 (Thermo Fisher, Cat# L3000001) in OptiMem reduced serum medium (Gibco, Cat# 31985062) for 24 hours. The Nano-Glo live cell reagent (Promega, Cat# N2011) was added to the wells, and bioluminescence was measured with the Glomax Discover plate reader (Promega, Cat# GM3000). Bioluminescence is obtained when the LgBiT and SmBiT fragments of nanoluciferase are in close proximity. Bioluminescence values were normalized to the untransfected control (fig. S4B). Transfection and assays were performed in triplicate.

Glycerol gradient centrifugation

Human telomerase was reconstituted in Expi293F cells (Thermo Fisher, Cat# A14527) by cotransfection of pcDNA3.1-ZZ-TEV-3xFlag-TERT, pcDNA3.1-ZZ-TEV-twin-Strep-SUMO*-TERT, and pcDNA3.1-U3-hTR-HDV for 48 hours. Cell extract was prepared through three cycles of hypotonic freeze-thaw lysis, snap-frozen in liquid nitrogen, and stored at −70°C until use. The resulting lysate (112 ml from 630 ml of cell suspension) was subjected to 2′-*O*-methyl oligonucleotide purification as described above. The eluate from this purification was incubated with prewashed MagStrepXT resin for 2 hours at 4°C. Telomerase was eluted at 4°C by overnight cleavage of the ZZ-TEV-twin-Strep tag with SUMOstar protease (LifeSensors, Cat# SP4110).

The eluate (20 μl) from the Strep-Tactin purification was then applied onto a 200-μl 10–30% glycerol gradient (Beckman Coulter, Cat# 343775), pre-equilibrated overnight at 4°C. The sample was spun at 4°C and 55,000 rpm for 90 min using a TLS55 rotor (Beckman Coulter). Sample was fractionated into 20-μl aliquots. Fractions were analyzed by telomerase activity assays and immunoblotting (fig. S12). For immunoblotting, a 4–15% Criterion TGX gel (Bio-Rad, Cat# 5671085) was used to resolve the fractions; and anti-TERT (1:1000, Abcam, Cat# 32020, lot 1041820-24) was used as primary antibody. Goat anti-rabbit Alexa-Fluor 680 (1:5000, Abcam, Cat# ab175773, lot GR222353-8) was used as a secondary antibody.

Total TERT levels for each glycerol gradient fraction were calculated for each fraction using ImageJ. The activity in each fraction was quantified with ImageQuant (Cytiva) and normalized against the signal of the recovery control (RC). This allowed the overall activity per TERT to be obtained. These experiments were not performed in triplicate owing to the discontinuation of the TERT antibody from Abcam (Cat# 32020, lot 1041820-24). An alternative TERT antibody from Proteintech (Cat# 27586-1-AP, lot 00132796) did not give quantifiable signals for TERT.

Parallel gradients were also run for gel filtration standards (1.8 mg/ml, Bio-Rad, Cat# 1511901) and the anaphase-promoting complex (0.5 mg/ml, a kind gift from J. Yang and D. Barford) (fig. S12B).

Preparation of dual-tagged telomerase with P4.2 stem and P4.2/P5 junction hTR mutants

To test the contribution of hTR in telomerase dimerization, Expi293F (Thermo Fisher, Cat# A14527) cells were cotransfected with pcDNA 3.1-ZZ-TEV-twin Strep-SUMO*-TERT, pcDNA 3.1-ZZ-TEV-3xFlag-TERT, and WT or mutant pcDNA 3.1-U3-hTR-HDV (Fig. 4, A and B). Cells were harvested after 48 hours, and lysates were prepared by three freeze-thaw cycles. For each reconstitution, we used 14 ml of input lysate from 150 ml of cell suspension. Lysates were subjected to oligonucleotide purification, as described above, to yield OE. OE was incubated with MagStrepXT resin (IBA LifeSciences, Cat# 2-4090-002) for 2 hours at 4°C. The resin was washed with wash buffer three times (see above), and telomerase was cleaved off the resin using SUMOstar protease (LifeSensors, Cat# SP4110) overnight at 4°C. Elution fractions were analyzed by immunoblotting against Flag-tag antibody (1:1000, Proteintech, Cat# 66008-4-Ig, lot 10027647) (see below). Telomerase activity assays, immunoblotting, and Northern blotting were also performed for the crude lysates (fig. S13). Expression, lysis, and purification for all samples were performed in triplicate.

Preparation of dyskerin and NHP2 mutants

To test dyskerin and NHP2 contribution in telomerase dimerization, Expi293F (Thermo Fisher, Cat# A14527) cells were cotransfected with pcDNA3.1-ZZ-TEV-twin-Strep-SUMO*-TERT, pcDNA3.1-U3-hTR-HDV, and pcDNA 3.1 with WT or mutant 3xFlag-tagged dyskerin or NHP2 construct. Cells were harvested after 48 hours, and lysates were prepared by three freeze-thaw cycles. For each reconstitution, we used 14 ml of input lysate from 100 ml of cell suspension. Lysates were subjected to oligonucleotide purification, as described above, to yield OE. After normalizing the final volume of OE, samples were analyzed by immunoblotting to compare the incorporation of overexpressed 3xFlag-dyskerin or 3xFlag-NHP2 into telomerase (Fig. 5, C to F, and fig. S17). Immunoblotting was also performed for the crude lysates. Expression, lysis, and purification were performed in triplicate for all WT and mutant dyskerin and NHP2.

Immunoblotting

Fractions of dual-tagged WT telomerase were resolved on a 3–8% Tris-Acetate NuPAGE gel (Invitrogen, Cat# EA0375PK2) in Tris-Acetate buffer and transferred onto a nitrocellulose membrane. The membrane was incubated for 1 hour at room temperature with 5% nonfat milk in phosphate-buffered saline (PBS) supplemented with 0.1% Tween-20 (PBST) before an overnight incubation at 4°C with anti-Flag (1:1000, Proteintech, Cat# 66008-4-Ug, lot 10027647). Following the washing, the membrane was incubated with goat anti-mouse Alexa-Fluor 680 secondary antibody (1:5000, Abcam, ab175775, lot GR3273649-2) in PBST for 1 hour. Scanning of the membrane was performed on a Li-COR Odyssey Imager, and the quantification was performed using ImageJ.

For the dyskerin and NHP2 mutant telomerase, the lysates and elution fractions from the oligo purification (OE) were resolved on a 4–12% Bis-Tris NuPAGE gel (Invitrogen, Cat# NP0321BOX) then transferred onto a nitrocellulose membrane and incubated with 5% nonfat milk in PBST for 1 hour. The membrane was first incubated with a primary antibody overnight at 4°C (1:1000 rabbit anti-dyskerin, Santa Cruz Biotechnology, Cat# sc-48794, lot E0214; or 1:20000 mouse anti-alpha tubulin, Proteintech, Cat# 66031-1-Ig, lot 10004185; or 1:1000 rabbit anti-NHP2, Proteintech, Cat# 15128-1-AP, lot 00059015).

For the dual-tagged ΔPAL dimer and catalytically inactive telomerase samples, 4–12% Bis-Tris NuPAGE gels were used to resolve lysates, Flag elution and Strep-Tactin elution fractions. Anti-TERT (1:1000, Abcam, Cat# 32020, lot 1041820-24) was used as a primary antibody for the dual-tagged ΔPAL telomerase dimer experiments. During this study, the TERT antibody was discontinued by Abcam. For the catalytically inactive telomerase samples, we used rabbit anti-TERT from Proteintech (1:1000, Cat# 27586-1-AP, lot 00132796), which gives lower signals than the Abcam TERT antibody, and rabbit TCAB1 antibody (1:1000, Proteintech, Cat# 14761-1-AP, lot 60343).

Membranes were washed three times and incubated with a secondary antibody (1:5000 goat anti-rabbit Alexa-Fluor 680, Abcam, Cat# ab175773, lot GR222353-8; or 1:5000 goat anti-mouse Alexa-Fluor 680, Abcam, Cat# ab175775, lot GR3273649-2) before being washed again and imaged on a Li-COR Odyssey Imager. All immunoblots were performed in triplicates, and quantification was done in ImageJ.

Northern blotting

Total RNA was extracted from the crude lysates of WT hTR and hTR mutants, coexpressed with ZZ-TEV-3xFlag-TERT and ZZ-TEV-twin-Strep-SUMO*-TERT, using TRIzol (Thermo Scientific, Cat# 15596026). The purified RNA samples were resolved on a 5% formamide polyacrylamide (19:1) TBE gel and then transferred onto a Hybond N+ nylon membrane (Cytiva, Cat# RPN303). The membrane was cross-linked using a Stratalinker UV cross-linker for 2 min. Following a 20-min incubation with Church's buffer [0.5 M phosphate buffer pH 7.2, 1% bovine serum albumin (BSA), 1 mM EDTA, and 7% SDS]

supplemented with 15% formamide at 50°C, the membrane was incubated with ^{32}P-end labeled DNA primers probes specific for the CR4/5 and PK/t domains of hTR overnight at 50°C. The membrane was washed twice with 4x SSC and 0.1% SDS, and twice with 2x SSC and 0.1% SDS. The dried membrane was exposed to a phosphorimager screen overnight and imaged on an Amersham Typhoon Biomolecular Imager (Cytiva).

Lentivirus plasmid transfection in HEK293T cells

HEK293T cells (ATCC, Cat# CRL-3216, RRID:CVCL_0063) were cultured in DMEM with GlutaMax (Gibco, Cat# 10566016), supplemented with 10% FBS, 100 μg/ml streptomycin, and 100 units/ml penicillin. To generate lentivirus, HEK293T cells were transfected with the packaging plasmid (psPAX2), the envelope plasmid (pMD2.G), and transgene constructs expressing hTR mutants, which were cloned into the DUET011 backbone. The WT transgene construct was a kind gift from K. Collins and X. Zhang (University of California, Berkeley) (*31*). Following a 24-hour incubation, the media was replaced, and cells were allowed to grow for another 24 hours. After this incubation period, the supernatant containing viral particles was filtered using a 0.22-μm filter, aliquoted, and stored at −70°C until further use.

Lentivirus transduction of HCT116 hTR knockout (KO) cells

HCT116 hTR KO cells were a kind gift from K. Collins and X. Zhang (University of California, Berkeley). To transduce HCT116 hTR KO cells, 2 ml of lentivirus was thawed and combined with 8 ml of prewarmed DMEM with GlutaMax (Gibco, Cat# 10566016) supplemented with 10% FBS, 100 μg/ml streptomycin, and 100 units/ml penicillin. The lentivirus and DMEM mixture was supplemented with 6 μg/ml of polybrene to enhance transduction efficiency and was then added to the HCT116 hTR KO cells. After 24 hours, the media was replaced. The media was replaced again 72 hours posttransduction, and the cells were selected with hygromycin B at 300 μg/ml for 7 days. Following the selection period, the cells were passaged using DMEM with GlutaMax (Gibco, Cat# 10566016) supplemented with 10% FBS, 100 μg/ml streptomycin, and 100 units/ml penicillin.

Extraction of genomic DNA from HCT116 cells

HCT116 cell pellets (~50 μl) were suspended in 500 μl of radioimmunoprecipitation assay (RIPA) buffer (SERVA, Cat# 39244.1), to which 6.25 μl of RNase A (Thermo Fisher, Cat# 12091021) (20 mg/ml) was added, followed by an incubation at 37°C for 30 min. After this incubation period, 10 μl of proteinase K (20 mg/ml) was introduced to the reaction, which was then incubated overnight at 50°C. The reaction mixture was extracted with phenol:chloroform:isoamyl alcohol (Thermo Scientific, Cat# 17908) and precipitated using isopropanol. The resulting DNA pellet was washed twice with 75% ethanol and air-dried before resuspension in TE buffer (10 mM Tris HCl pH 7.4 and 1 mM EDTA pH 7.4) with constant rotation overnight.

Telomere restriction fragment assay

Between 3 and 10 μg of purified genomic DNA was digested with FastDigest AluI (Thermo Fisher, Cat# FD0014) and MboI (Thermo Fisher, Cat# FD0814) restriction enzymes at 37°C overnight. The digested DNA fragments were separated on a 0.7% agarose gel in 1x TAE buffer for approximately 23 hours at 35 V. The gel was vacuum dried for 1 hour at 50°C. The dried gel was denatured using denaturation buffer (0.5 M NaOH, 1.5 M NaCl) for 30 min at 50°C. After denaturation, the gel was washed with 4x SSC buffer supplemented with 0.1% SDS for 10 min and then blocked with Church's buffer for 30 min at 50°C. Following the blocking step, ^{32}P-end-labeled telomeric repeat probes [$(TTAGGG)_4$, $(CCCTAA)_4$] and a 1 kb plus DNA ladder (Thermo Fisher, Cat# 10780718) probe were added. The probes were hybridized overnight at 50°C. The gel was washed three times with 4x SSC and 0.1% SDS at 40°C. The gel was then exposed to a phosphorimager screen for at least 24 hours before being imaged using an Amersham Typhoon Biomolecular Imager (Cytiva).

Negative staining EM sample preparation

Telomerase sample of interest was prepared without cross-linker and applied (3 μl per grid) on 400 mesh copper grids (Electron Microscopy Sciences, Cat# G400-Cu) with a homemade amorphous carbon film on nitrocellulose. Prior to sample application, negative stain grids were glow discharged using a Sputter coater discharger (model Edwards S150B). Sample was incubated on the grid for 90 s before undergoing 1 min incubation with 2% w/v uranyl formate (UF) by gentle agitation. Automatic data collection was done using Tecnai F20 transmission electron microscope (200 kV) with a Falcon 3 direct electron detector in linear mode. Collection was performed in EPU software and at a physical pixel size of 2.02 Å per pixel, with a total electron dose of 41.7 electrons per Å^2 over a total exposure time of 2 s. We collected 4664 micrographs for the dual-tagged WT telomerase dimer (fig. S5, C to F); 1419 micrographs for the dual-tagged ΔPAL dimer (fig. S10, G to I); 1257 micrographs for the single-tagged P4.2 switch mutant (fig. S16, A and B); and 1102 micrographs for the single-tagged P4.2 comp. mutant (fig. S16, C and D).

Negative stain EM data processing

Data processing was performed in RELION 5.0 (*54*, *55*). CTFFIND4.1 was used to estimate contrast transfer function (CTF) parameters of the micrographs (*56*). Data for each complex were processed separately as detailed below.

The dual-tagged WT telomerase dimer: A total of 149,089 particles were first picked with Laplacian-of-Gaussian (LoG) blob detection in RELION (*57*). The particles were binned by 4, extracted with a 60^2 pixel box and subjected to multiple rounds of 2D classification. We then unbinned a subset of 20,105 particles for generating 2D references to improve particle picking. Four 2D references from 863 particles were selected as 2D references for reference-based picking. The second round of picking yielded 50,123 particles, which were binned by 4, extracted with a 60^2 pixel box and subjected to 25 rounds of 3D classification with eight classes and a regularization parameter T of 4. We used the cryo-EM reconstruction of the full dimer as an initial model for this 3D classification. Six of the classes resembled the dimer particles observed in cryo-EM data and were thus pooled for 2D classification. Representative 2D class averages are shown in fig. S5E.

The dual-tagged ΔPAL dimer: To avoid model bias, we picked particles using 2D references of the monomeric telomerase RNP. A total of 110,700 particles were picked, binned by 4, extracted with a 60^2 pixel box, and subjected to several rounds of 2D classification. Representative 2D class averages are shown in fig. S10H. Although the particles were picked with 2D references of the telomerase monomer, the majority resembled the dimeric particles.

The P4.2 switch mutant: To generate 2D references for picking, we picked 207,603 particles using LoG blob detection in RELION. Particles were binned by 4 and extracted with a 60^2 pixel box. After several rounds of 2D classification, we unbinned a subset of 4516 particles for 2D classification. Four 2D references from 1493 particles were selected as 2D references for reference-based picking. A total of 230,944 particles were repicked using these 2D references, binned by 4, extracted with a 60^2 pixel box, and subjected to several rounds of 2D classification. 2D classes of monomeric telomerase RNP from 14,547 particles are shown in fig. S16B.

The P4.2 comp. mutant: A total of 278,349 particles were picked using the 2D references from the P4.2 switch mutant, binned by 4, and extracted with a 60^2 pixel box. After several rounds of 2D classification,

we obtained 2D class averages of monomeric telomerase RNP from 94,006 particles, which are shown in fig. S16D.

DMS chemical probing and data analysis

RNA structures in telomerase complexes reconstituted with WT hTR, and P4.2 switch and comp. hTR mutants were obtained using DMS-MaPseq (*58*). For DMS probing, the RNA was allowed to react with DMS at a final concentration of 1% for 5 min at 37°C. DTT was added to a final concentration of 0.5 M to quench the reaction. To remove the protein components after DMS probing, we added an equal volume of triazole and chloroform, mixed well, and centrifuged the sample for 15 min. The supernatant was mixed with an equal volume of 100% ethanol. RNA Clean & Concentrator Kits (Zymo Research, Cat# R1016) were used for RNA purification following the manufacturer's protocol. Reverse transcription was done using SuperScript II Reverse Transcriptase (Thermo Fisher, Cat# 18064014) at 42°C for 90 min (*59*). To remove the SuperScript II enzyme, an equal volume of phenol:chloroform:isoamyl alcohol (25:24:1) was added to the reaction mixture, followed by centrifugation for 15 min. The aqueous phase was collected and subjected to further purification using a MicroSpin S-200 HR column (Cytiva, Cat# 27512001) in accordance with the manufacturer's instructions.

Polymerase chain reactions with 10 cycles were performed with the reverse primer (5′-GCGGGGACTCGCTCCGTTCCTCTT-3′) and the forward primer (5′-GGGTTGCGGAGGGTGGGCCTG-3′) using KOD Xtreme Hot Start DNA Polymerase (Novagen, Cat# 71975). Two independent biological replicates for each sample were generated. The purified DNA samples were subjected to Nanopore library construction by following the manufacturer's instructions for the native barcoding kit (NBD-24). Raw reads from DMS probing data were base called and demultiplexed using Dorado (https://github.com/nanoporetech/dorado). The resulting reads were mapped using minimap2 (*60*) with the following parameters: minimap2 -t 8 -ax splice --secondary=no -G 12000. The mutation rate at each nucleotide was calculated by dividing the number of mutations by the number of reads at that location to generate the overall DMS reactivity profiles (fig. S15E). DMS reactivity profiles were then normalized by scaling each reactivity value by the median of the top 10% most reactive positions (*61*).

Cryo-EM sample preparation and data collection

Purified telomerase-DNA-TPT sample was cross-linked with bis(sulfosuccinimidyl)suberate (BS3) cross-linker (Thermo Fisher, Cat# A39266) on ice for 1 hour at 0.5 mM final BS3 concentration. The reaction was then stopped with quench buffer (200 mM Tris pH 8.0, 150 mM NaCl, 2 mM $MgCl_2$, 0.05% IGEPAL CA-630, and 1 mM DTT) and buffer-exchanged into cryo-EM buffer (20 mM HEPES NaOH pH 8.0, 150 mM NaCl, 2 mM $MgCl_2$, 0.05% IGEPAL CA-630, 1.0% trehalose, and 1 mM DTT) before cryo-EM grid preparation. Cross-linked telomerase-DNA-TPT complex was applied (3 μl per grid) onto a C-flat-T-50 4/2 grids (Protochips, Cat# CF-4/2-4Cu-T-50). The grids were precoated inhouse with a 5- to 6-nm-thick layer of homemade continuous carbon film and glow-discharged using a Sputter coater discharger (model Edwards S150B). Following a 2-min incubation, the grids were blotted for 5 to 6 s at 4°C and 100% humidity and vitrified in liquid ethane using an FEI Vitrobot MK IV. Data collection was performed on Thermo Fisher Titan Krios transmission electron microscope operated at 300 kV and equipped with a Gatan K3 direct electron detector camera and a GIF Quantum energy filter using 20 eV slit width. EPU software (Thermo Fisher) was used for automatic collection in counting mode. The physical pixel size of 1.059 Å was used with a total electron dose of ~48 electrons per $Å^2$ over a total exposure time of 2.5 s and a defocus range of −0.8 to 2.4 μm. Doses were fractionated into 48 movie frames. A total of 66,992 movies were collected in four separate sessions.

Cryo-EM data processing

Data processing was performed using RELION 4.0, RELION 5.0, and CryoSPARC v4.1.2 (fig. S2) (*54*, *57*, *62*). Movie frames were gain- and drift-corrected, dose-weighted, and summed into single micrographs using motion-correction program implemented within RELION 4.0 (*57*). All 3D classification after the signal subtraction steps (except for those without alignments) and refinements in RELION were performed with the Blush algorithm (*55*). CTF parameters were estimated for the motion-corrected micrographs using CTFFIND-4.1 (*56*). A total of 66,992 movies were corrected as described above [dataset 1 (23,681 micrographs), dataset 2 (22,330 micrographs), dataset 3 (10,832 micrographs), dataset 4 (10,149 micrographs)].

3D refinements were performed using independent data half-sets. Reported resolutions are estimated at the gold-standard Fourier shell correlation (FSC) = 0.143 criterion between the two half-maps. FSCs were calculated using a soft mask. We also corrected for the modulation transfer function of the detector and applied a B-factor sharpening, as determined by RELION or a user-defined value.

Cryo-EM data processing of the telomerase dimer

For dataset 1, particle picking was performed using a reference-based autopicking. We first used 2D references generated from previous work (*23*) and then generated new references through multiple rounds of 2D classification. Particles were picked again using the new 2D references. Picked particles from dataset 1 were binned by 8 and extracted using a 56^2 pixel box size. Two rounds of 2D and 3D classifications were done together with the dataset 2 using a consensus monomeric telomerase map as a reference (map not deposited) (*23*). During the classification, a subset of telomerase dimer particles was obtained and refined to yield a 11.8-Å reconstruction, which was used as an initial dimer reference for subsequent classification.

All binned particles from dataset 1 were subjected to an initial round of 3D classification using a dimer map as a reference. We then performed a second round of 3D classification using an angular sampling of 15° for 25 iterations and 7.5° for another 25 iterations, regularization parameter T of 4 and a dimer map as a reference. The best dimer classes were selected for a reference-free 2D classification, from which a total of 598,022 particles were selected, unbinned, and imported into CryoSPARC.

For dataset 2, particle picking was done using a Topaz trained model (*63*) implemented within RELION 4.0. Selected particles with figure-of-merit (FOM) cutoff values of −1.5 were binned by 8 and extracted using a 56^2 pixel box size. Particles from dataset 1 and dataset 2 were subjected to two rounds of 2D and 3D classifications to obtain a telomerase dimer map as described above. After obtaining the dimer reference, all binned particles from dataset 2 underwent two rounds of 3D classification with a dimer map as a reference. The best 3D classes of telomerase dimer were selected for a reference-free 2D classification to further remove bad particles. A total of 824,473 particles were selected, unbinned, and imported into CryoSPARC.

For dataset 3 and dataset 4, particle picking was performed using a reference-based autopicking with 2D references of the monomeric telomerase obtained from dataset 1. The picked particles were binned by 8 and extracted using a 56^2 pixel box size. The binned particles underwent a first round of 3D classification to remove junk particles, followed by a second round of 3D classification using an angular sampling of 7.5° and regularization parameter T of 4. The second round of 3D classification used a dimer map as a reference as described for dataset 1 and dataset 2. The best dimer 3D classes were selected for a reference-free 2D classification, from which a total of 239,908 (dataset 3) and a total of 208,882 (dataset 4) particles were selected, unbinned, and imported into CryoSPARC.

In CryoSPARC, a subset of particles (193,181 particles) from datasets 1, 2, 3, and 4 was used to generate six ab initio reconstruction maps with C2 symmetry. The whole particle set was then classified

into six volumes using the heterogeneous refinement algorithm with C2 symmetry and maps from the prior ab initio reconstruction step as initial models (*62*). The class with the best features containing 505,039 particles was subjected to the nonuniform refinement (*64*) to yield a reconstruction of telomerase dimer at 6.2-Å resolution. The particles were exported as a particle stack using PyEM (*65*) for further processing in RELION 4.0 and RELION 5.0. To investigate the heterogeneity of the full telomerase dimer, we performed 3D variability analysis (3DVA) on the 6.2-Å dimer map in CryoSPARC (*66*). The 3DVA results showing the global heterogeneity are presented in movie S1.

The exported particle stack was refined in RELION to give a reconstruction at 7.1-Å resolution without any symmetry applied. The map was aligned to the C2 symmetry axis, symmetrized in RELION, and used as a reference for a 3D refinement with C2 symmetry. This yielded a reconstruction of the full telomerase dimer at 4.4-Å resolution. This reconstruction was well aligned on the H/ACA RNPs but poorly aligned on the catalytic cores. Thus, we used this refinement for the subsequent signal subtraction procedures but not for model fitting or deposition to the Electron Microscopy Data Bank (EMDB). Particles from this refinement were subjected to C2 symmetry expansion.

Cryo-EM data processing of the individual H/ACA RNP protomer

To improve the resolution of the individual H/ACA RNP lobes and regions responsible for dimerization, we used the 4.4-Å dimer reconstruction to perform signal subtraction with recentering on the symmetry expanded particles. The box size of the signal subtracted particles was downsized to 280^2 pixels to speed up computation. The signal-subtracted particles were refined and then classified into four classes using a local classification with 5° local angular search steps. One class with 322,295 particles had well-defined high-resolution features and was further refined to 3.0-Å resolution. To resolve the dimerization interface between the 5′ H/ACA heterotetramer of one H/ACA RNP and the P4/5 linker of hTR of the second H/ACA RNP, a mask that included only these regions was used for alignment-free focused 3D classification with a regularization parameter *T* of 10. A subset of 260,466 particles, which showed the best-resolved P4/5 linker region, was refined to 3.0-Å resolution. We then performed CTF refinement (beam tilt, trefoil, and fourth-order aberrations, anisotropic magnification, per-particle defocus and per-micrograph astigmatism) (*67*), followed by a 3D refinement. The resulting particles yielded a final 3.0-Å resolution map of an individual H/ACA RNP with the bound P4/P5 linker from the other protomer. Although the resolution of the map after CTF refinement did not improve, the quality of the map was improved. This reconstruction was used for model building, refinement, and validation of telomerase H/ACA RNP protomer.

Cryo-EM data processing of the H/ACA RNP dimer

To analyze the dimerization interface between the two H/ACA RNPs, we performed signal subtraction with recentering on the non-symmetry-expanded particles. We generated a mask around the two H/ACA RNPs to remove the signal from both catalytic cores. The box size of the signal-subtracted particles was downsized to 280^2 pixels to speed up computation. The signal-subtracted particles were refined to 4.0-Å resolution with C2 symmetry using a C2 symmetry axis–aligned and symmetrized dimer reference. We then performed a 3D classification with local searches and a C2 symmetry relaxation. A subset of 130,095 particles was used for 3D refinement (4.1-Å resolution), followed by alignment-free 3D classification with regularization parameter *T* of 8 and a mask around the 3′ GAR1-dimerization interface. A subset of 88,419 particles, which showed the most complete density for both 3′ GAR1 subunits, was refined to 3.9-Å resolution. This reconstruction was used for model building, refinement, and validation of the telomerase H/ACA RNP dimer.

Cryo-EM data processing of telomerase catalytic cores

To analyze the catalytic core, we used the 4.4-Å dimer reconstruction to perform signal subtraction around one telomerase catalytic core with recentering on the symmetry-expanded particles. The box size of the signal-subtracted particles was downsized to 280^2 pixels to speed up computation. The signal-subtracted particles were refined and then classified into four classes using 25 iterations with angular sampling of 1.8° and regularization parameter *T* of 4. The best class with 273,757 particles had well-defined features and was further refined to 3.4-Å resolution. We then performed CTF refinement (beam tilt, trefoil, and fourth-order aberrations, anisotropic magnification, per-particle defocus, and per-micrograph astigmatism) (*67*), followed by a 3D refinement. This yielded a final map of individual telomerase catalytic core at 3.3-Å resolution. This reconstruction was used for model building, refinement, and validation of telomerase catalytic core monomer (C2).

Additionally, we wanted to determine whether the DNA is bound in both catalytic cores of the telomerase dimer. To resolve the two catalytic cores independently, signal subtraction was performed around each catalytic core in a 7.1-Å dimer map, with recentering on the non-symmetry-expanded particles. Subsequently, a 3D classification into four classes using 25 iterations with angular sampling of 3.7° was carried out, resulting in one class with high-resolution features. For catalytic core from protomer 1 (catalytic core 1), we selected a subset of 138,966 particles. For catalytic core from protomer 2 (catalytic core 2), a subset of 133,259 particles was selected. We refined these two subsets, followed by CTF refinement (beam tilt, trefoil, and fourth-order aberrations, anisotropic magnification, per-particle defocus, and per-micrograph astigmatism), and final 3D refinement. This approach yielded reconstructions at 3.8-Å resolution for catalytic core 1 and at 3.6-Å resolution for catalytic core 2.

Finally, to confirm the presence of DNA in both catalytic cores within a single telomerase dimer particle, we examined the particle subsets used to obtain the maps of telomerase catalytic cores 1 and 2. We searched for dimer particles present in both subsets using https://github.com/sami-chaaban/starparser. We then performed local 3D refinement on the shared particles using 1.8° angular sampling. This approach yielded maps of telomerase catalytic cores 1 and 2 at 4.1- and 3.9-Å resolution, respectively, with both reconstructions showing DNA density in the active site.

Model building and refinement

To facilitate model building, all maps were converted into MTZ format using REFMAC5.8 (*68*, *69*) to allow map blurring and sharpening in COOT (*70*). The published models of the catalytic core bound to TPP1 [Protein Data Bank (PDB) ID 7QXA] and H/ACA RNP (PDB ID 8OUE) (*23*, *27*) were used as initial models for model building. These models were fitted into the corresponding maps by rigid-body fitting in COOT. Manual adjustments of the models were performed in COOT to improve the map fit. The P4.2/5 and P1 linkers of hTR were first manually built in COOT using the 3.9-Å H/ACA RNP dimer map. The resulting model was used as a starting model for DRRAFTER (*26*). After DRRAFTER, the RNA geometry was further improved using ERRASER2.0 (*71*) and manual adjustments in COOT.

Model refinement was performed in reciprocal space using Servalcat and REFMAC5.8 (*68*, *72*) with protein secondary structure restraints and nucleic acid restraints calculated using PROSMART and LIBG, respectively (*69*, *73*). Phenix 1.20 was used to calculate model-versus-map FSCs and EMRinger scores (*74*). Geometries were assessed using the MolProbity server (http://molprobity.biochem.duke.edu/) (*75*). Tables S1 and S2 provide a summary of the refined models.

The refined models of the H/ACA RNP dimer and the catalytic cores were rigid-body fitted into the 6.2-Å consensus dimer map. The resulting models were used as an input for DRRAFTER modeling of the full hTR within the dimer. Due to the limited resolution of the map, no model refinement was performed. Instead, the top 10 DRRAFTER models of hTR and fitted models of the protein subunits of both the

catalytic core and the H/ACA RNP are provided in a Pymol session (data S1). The G-quadruplex structure in the 5′ region of hTR was modeled by DRRAFTER; and the ensemble of the structures with the lowest energy are included in a Pymol session (data S3).

DRRAFTER modeling of RNA in telomerase dimer

DRRAFTER was used for the modeling of hTR regions with higher disorder (*26*). In each case, 2000 to 5000 models were obtained, and a set of the lowest energy models were selected to represent the ensemble of conformations. The secondary structure was enforced, with ideal A-form helices used as a template as well as the parallel conformation of the G-quadruplex for residues 1–17 of hTR (*76*). For the H/ACA RNP dimer region, the cryo-EM map around the RNA of interest (residues 1–31, 195–247, and 322–370) was isolated by creating a 12-Å zoning around the RNA and removing segments associated with modeled protein using Segger in ChimeraX (*77*). Within the H/ACA RNP dimer, only one of the RNA chains was modeled, assuming the other is a symmetry copy. Four sets of ensemble models of the H/ACA RNP dimer region were created. One was created using 15-Å restraints from the initial placed positions, and another with 30-Å restraints. Little difference was observed between these two ensembles, suggesting confidence in the global placement of helices. Furthermore, observing density between P4.1 stem of hTR and the proposed G-quadruplex (GQ) density, we attempted to model that density in a variety of methods. First, we did not enforce any base pairing in the region, resulting in an unstructured RNA chain modeled into the density. We named this model "unordered." Second, to obtain models with a more energetically favorable RNA fold in line with literature (*72*), we enforced base pairing between nucleotides in that region (data S3). We used a published G-quadruplex model (PDB ID 1RAU) as a template (*78*). Two additional model ensembles were created, one forcing a base pairing between U5 and G345 of hTR, and another between C7 and G345 of hTR (data S3). For the full telomerase dimer map, a similar method was used with first isolating the cryo-EM map around the RNA to be modeled (residues 1–40, 185–210, 219–250, and 320–355). Secondary structure was enforced, and template helices and quadruplex were used as above, but there were no restraints placed on initial positions. Additionally, both RNA chains were modeled separately. The lowest energy models of each RNA chain were selected and combined to create an ensemble of full dimer models (data S1).

Q-score calculations for the 5′ leader sequence of hTR

From all sets of model ensembles, the best 5′ GQ model was selected on the basis of the highest Q-score (model number 6 with 15-Å restraints). Additionally, the unordered model for the same region was generated without enforcing base pairing as described above. The best 5′ GQ model (ordered 5′GQ), the unordered model, and the 5′ hairpin (PDB ID 7V9A) (*10*) were compared to determine the most suitable conformation of the 5′ hTR leader sequence (residues 1–17) on the basis of the map-vervus-model Q-scores using the 3.9-Å H/ACA RNP dimer map. The backbone and overall Q-scores were calculated in UCSF Chimera and ChimeraX (*77*, *79*, *80*). In ChimeraX, a Q-score plugin (courtesy of T. Croll) was used to visualize the backbone Q-scores for individual residues (fig. S20) (*79*). Q-scores for unordered model, ordered 5′ GQ, and 5′ hairpin generated in Chimera are also included in data S2.

Map and model visualization

Maps were visualized in both Chimera and ChimeraX. Illustrations were prepared using Chimera, ChimeraX (*77*), Pymol (www.pymol.org), and Adobe Illustrator.

REFERENCES AND NOTES

1. M. Z. Levy, R. C. Allsopp, A. B. Futcher, C. W. Greider, C. B. Harley, Telomere end-replication problem and cell aging. *J. Mol. Biol.* **225**, 951–960 (1992). doi: 10.1016/0022-2836(92)90096-3; pmid: 1613801
2. R. A. Wu, H. E. Upton, J. M. Vogan, K. Collins, Telomerase mechanism of telomere synthesis. *Annu. Rev. Biochem.* **86**, 439–460 (2017). doi: 10.1146/annurev-biochem-061516-045019; pmid: 28141967
3. E. H. Blackburn, K. Collins, "Telomerase: An RNP enzyme synthesizes DNA" in *RNA Worlds*, R. F. Gesteland, J. F. Atkins, T. R. Cech, Eds. (Cold Spring Harbor Laboratory Press, 2010), pp. 205–213.
4. N. W. Kim *et al.*, Specific association of human telomerase activity with immortal cells and cancer. *Science* **266**, 2011–2015 (1994). doi: 10.1126/science.7605428; pmid: 7605428
5. J. W. Shay, S. Bacchetti, A survey of telomerase activity in human cancer. *Eur. J. Cancer* **33**, 787–791 (1997). doi: 10.1016/S0959-8049(97)00062-2; pmid: 9282118
6. G. Sarek, P. Marzec, P. Margalef, S. J. Boulton, Molecular basis of telomere dysfunction in human genetic diseases. *Nat. Struct. Mol. Biol.* **22**, 867–874 (2015). doi: 10.1038/nsmb.3093; pmid: 26581521
7. M. Armanios, The role of telomeres in human disease. *Annu. Rev. Genomics Hum. Genet.* **23**, 363–381 (2022). doi: 10.1146/annurev-genom-010422-091101; pmid: 35609925
8. T. H. D. Nguyen *et al.*, Cryo-EM structure of substrate-bound human telomerase holoenzyme. *Nature* **557**, 190–195 (2018). doi: 10.1038/s41586-018-0062-x; pmid: 29695869
9. G. E. Ghanim *et al.*, Structure of human telomerase holoenzyme with bound telomeric DNA. *Nature* **593**, 449–453 (2021). doi: 10.1038/s41586-021-03415-4; pmid: 33883742
10. F. Wan *et al.*, Zipper head mechanism of telomere synthesis by human telomerase. *Cell Res.* **31**, 1275–1290 (2021). doi: 10.1038/s41422-021-00586-7; pmid: 34782750
11. E. D. Egan, K. Collins, Biogenesis of telomerase ribonucleoproteins. *RNA* **18**, 1747–1759 (2012). doi: 10.1261/rna.034629.112; pmid: 22875809
12. A. S. Venteicher *et al.*, A human telomerase holoenzyme protein required for Cajal body localization and telomere synthesis. *Science* **323**, 644–648 (2009). doi: 10.1126/science.1165357; pmid: 19179534
13. K. T. Tycowski, M. D. Shu, A. Kukoyi, J. A. Steitz, A conserved WD40 protein binds the Cajal body localization signal of scaRNP particles. *Mol. Cell* **34**, 47–57 (2009). doi: 10.1016/j.molcel.2009.02.020; pmid: 19285445
14. G. Schnapp, H.-P. Rodi, W. J. Rettig, A. Schnapp, K. Damm, One-step affinity purification protocol for human telomerase. *Nucleic Acids Res.* **26**, 3311–3313 (1998). doi: 10.1093/nar/26.13.3311; pmid: 9628936
15. C. Wenz *et al.*, Human telomerase contains two cooperating telomerase RNA molecules. *EMBO J.* **20**, 3526–3534 (2001). doi: 10.1093/emboj/20.13.3526; pmid: 11432839
16. S. B. Cohen *et al.*, Protein composition of catalytically active human telomerase from immortal cells. *Science* **315**, 1850–1853 (2007). doi: 10.1126/science.1138596; pmid: 17395830
17. A. Sauerwald *et al.*, Structure of active dimeric human telomerase. *Nat. Struct. Mol. Biol.* **20**, 454–460 (2013). doi: 10.1038/nsmb.2530; pmid: 23474713
18. D. Alves *et al.*, Single-molecule analysis of human telomerase monomer. *Nat. Chem. Biol.* **4**, 287–289 (2008). doi: 10.1038/nchembio.82; pmid: 18391947
19. R. A. Wu, Y. S. Dagdas, S. T. Yilmaz, A. Yildiz, K. Collins, Single-molecule imaging of telomerase reverse transcriptase in human telomerase holoenzyme and minimal RNP complexes. *eLife* **4**, e08363 (2015). doi: 10.7554/eLife.08363; pmid: 26457608
20. T. M. Errington, D. Fu, J. M. Wong, K. Collins, Disease-associated human telomerase RNA variants show loss of function for telomere synthesis without dominant-negative interference. *Mol. Cell. Biol.* **28**, 6510–6520 (2008). doi: 10.1128/MCB.00777-08; pmid: 18710936
21. E. D. Egan, K. Collins, Specificity and stoichiometry of subunit interactions in the human telomerase holoenzyme assembled in vivo. *Mol. Cell. Biol.* **30**, 2775–2786 (2010). doi: 10.1128/MCB.00151-10; pmid: 20351177
22. B. Liu *et al.*, Structure of active human telomerase with telomere shelterin protein TPP1. *Nature* **604**, 578–583 (2022). doi: 10.1038/s41586-022-04582-8; pmid: 35418675
23. Z. Sekne, G. E. Ghanim, A. M. van Roon, T. H. D. Nguyen, Structural basis of human telomerase recruitment by TPP1-POT1. *Science* **375**, 1173–1176 (2022). doi: 10.1126/science.abn6840; pmid: 35201900
24. A. S. Dixon *et al.*, NanoLuc complementation reporter optimized for accurate measurement of protein interactions in cells. *ACS Chem. Biol.* **11**, 400–408 (2016). doi: 10.1021/acschembio.5b00753; pmid: 26569370
25. T. L. Beattie, W. Zhou, M. O. Robinson, L. Harrington, Functional multimerization of the human telomerase reverse transcriptase. *Mol. Cell. Biol.* **21**, 6151–6160 (2001). doi: 10.1128/MCB.21.18.6151-6160.2001; pmid: 11509658
26. K. Kappel *et al.*, De novo computational RNA modeling into cryo-EM maps of large ribonucleoprotein complexes. *Nat. Methods* **15**, 947–954 (2018). doi: 10.1038/s41592-018-0172-2; pmid: 30377372
27. G. E. Ghanim, Z. Sekne, S. Balch, A.-M. M. van Roon, T. H. D. Nguyen, 2.7 Å cryo-EM structure of human telomerase H/ACA ribonucleoprotein. *Nat. Commun.* **15**, 746 (2024). doi: 10.1038/s41467-024-45002-x; pmid: 38272871
28. M. E. Sayed *et al.*, Catalysis-dependent inactivation of human telomerase and its reactivation by intracellular telomerase-activating factors (iTAFs). *J. Biol. Chem.* **294**, 11579–11596 (2019). doi: 10.1074/jbc.RA118.007234; pmid: 31186347
29. J. R. Mitchell, J. Cheng, K. Collins, A box H/ACA small nucleolar RNA-like domain at the human telomerase RNA 3′ end. *Mol. Cell. Biol.* **19**, 567–576 (1999). doi: 10.1128/MCB.19.1.567; pmid: 9858580

30. T. Kiss, E. Fayet-Lebaron, B. E. Jády, Box H/ACA small ribonucleoproteins. *Mol. Cell* **37**, 597–606 (2010). doi: 10.1016/j.molcel.2010.01.032; pmid: 20227365
31. J. M. Vogan *et al.*, Minimized human telomerase maintains telomeres and resolves endogenous roles of H/ACA proteins, TCAB1, and Cajal bodies. *eLife* **5**, e18221 (2016). doi: 10.7554/eLife.18221; pmid: 27525486
32. E. D. Egan, K. Collins, An enhanced H/ACA RNP assembly mechanism for human telomerase RNA. *Mol. Cell. Biol.* **32**, 2428–2439 (2012). doi: 10.1128/MCB.00286-12; pmid: 22527283
33. C. Trahan, C. Martel, F. Dragon, Effects of dyskeratosis congenita mutations in dyskerin, NHP2 and NOP10 on assembly of H/ACA pre-RNPs. *Hum. Mol. Genet.* **19**, 825–836 (2010). doi: 10.1093/hmg/ddp551; pmid: 20008900
34. D. Fu, K. Collins, Distinct biogenesis pathways for human telomerase RNA and H/ACA small nucleolar RNAs. *Mol. Cell* **11**, 1361–1372 (2003). doi: 10.1016/S1097-2765(03)00196-5; pmid: 12769858
35. P. A. Chong, R. M. Vernon, J. D. Forman-Kay, RGG/RG motif regions in RNA binding and phase separation. *J. Mol. Biol.* **430**, 4650–4665 (2018). doi: 10.1016/j.jmb.2018.06.014; pmid: 29913160
36. J. Gros, A. Guédin, J.-L. Mergny, L. Lacroix, G-Quadruplex formation interferes with P1 helix formation in the RNA component of telomerase hTERC. *ChemBioChem* **9**, 2075–2079 (2008). doi: 10.1002/cbic.200800300; pmid: 18683270
37. X. Li *et al.*, Structure, interactions and effects on activity of the 5′-terminal region of human telomerase RNA. *J. Biochem.* **141**, 755–765 (2007). doi: 10.1093/jb/mvm081; pmid: 17387120
38. A. N. Sexton, K. Collins, The 5′ guanosine tracts of human telomerase RNA are recognized by the G-quadruplex binding domain of the RNA helicase DHX36 and function to increase RNA accumulation. *Mol. Cell. Biol.* **31**, 736–743 (2011). doi: 10.1128/MCB.01033-10; pmid: 21149580
39. S. Lattmann, M. B. Stadler, J. P. Vaughn, S. A. Akman, Y. Nagamine, The DEAH-box RNA helicase RHAU binds an intramolecular RNA G-quadruplex in TERC and associates with telomerase holoenzyme. *Nucleic Acids Res.* **39**, 9390–9404 (2011). doi: 10.1093/nar/gkr630; pmid: 21846770
40. J. L. Chen, M. A. Blasco, C. W. Greider, Secondary structure of vertebrate telomerase RNA. *Cell* **100**, 503–514 (2000). doi: 10.1016/S0092-8674(00)80687-X; pmid: 10721988
41. E. P. Booy *et al.*, The RNA helicase RHAU (*DHX36*) unwinds a G4-quadruplex in human telomerase RNA and promotes the formation of the P1 helix template boundary. *Nucleic Acids Res.* **40**, 4110–4124 (2012). doi: 10.1093/nar/gkr1306; pmid: 22238380
42. Z. Lu *et al.*, Identification of G-quadruplex-interacting proteins in living cells using an artificial G4-targeting biotin ligase. *Nucleic Acids Res.* **52**, e37 (2024). doi: 10.1093/nar/gkae126; pmid: 38452210
43. J. Wapling, K. L. Moore, S. Sonza, J. Mak, G. Tachedjian, Mutations that abrogate human immunodeficiency virus type 1 reverse transcriptase dimerization affect maturation of the reverse transcriptase heterodimer. *J. Virol.* **79**, 10247–10257 (2005). doi: 10.1128/JVI.79.16.10247-10257.2005; pmid: 16051818
44. T. Restle, B. Müller, R. S. Goody, Dimerization of human immunodeficiency virus type 1 reverse transcriptase. A target for chemotherapeutic intervention. *J. Biol. Chem.* **265**, 8986–8988 (1990). doi: 10.1016/S0021-9258(19)38799-X; pmid: 1693146
45. R. S. Fletcher *et al.*, Single-step purification of recombinant wild-type and mutant HIV-1 reverse transcriptase. *Protein Expr. Purif.* **7**, 27–32 (1996). doi: 10.1006/prep.1996.0004; pmid: 9172779
46. C.-K. Tseng, H.-F. Wang, M. R. Schroeder, P. Baumann, The H/ACA complex disrupts triplex in hTR precursor to permit processing by RRP6 and PARN. *Nat. Commun.* **9**, 5430 (2018). doi: 10.1038/s41467-018-07822-6; pmid: 30575725
47. K. G. Zyner *et al.*, Genetic interactions of G-quadruplexes in humans. *eLife* **8**, e46793 (2019). doi: 10.7554/eLife.46793; pmid: 31287417
48. I. A. Hendriks *et al.*, Uncovering global SUMOylation signaling networks in a site-specific manner. *Nat. Struct. Mol. Biol.* **21**, 927–936 (2014). doi: 10.1038/nsmb.2890; pmid: 25218447
49. S. E. Whitehead *et al.*, Determinants of the interaction of the spinal muscular atrophy disease protein SMN with the dimethylarginine-modified box H/ACA small nucleolar ribonucleoprotein GAR1. *J. Biol. Chem.* **277**, 48087–48093 (2002). doi: 10.1074/jbc.M204551200; pmid: 12244096
50. J. C. Schmidt, A. J. Zaug, T. R. Cech, Live cell imaging reveals the dynamics of telomerase recruitment to telomeres. *Cell* **166**, 1188–1197.e9 (2016). doi: 10.1016/j.cell.2016.07.033; pmid: 27523609
51. J. Jiang *et al.*, The architecture of *Tetrahymena* telomerase holoenzyme. *Nature* **496**, 187–192 (2013). doi: 10.1038/nature12062; pmid: 23552895
52. E. Bajon, N. Laterreur, R. J. Wellinger, A single templating RNA in yeast telomerase. *Cell Rep.* **12**, 441–448 (2015). doi: 10.1016/j.celrep.2015.06.045; pmid: 26166570
53. J. D. Podlevsky, C. J. Bley, R. V. Omana, X. Qi, J. J. Chen, The Telomerase Database. *Nucleic Acids Res.* **36**, D339–D343 (2008). doi: 10.1093/nar/gkm700; pmid: 18073191
54. D. Kimanius, L. Dong, G. Sharov, T. Nakane, S. H. W. Scheres, New tools for automated cryo-EM single-particle analysis in RELION-4.0. *Biochem. J.* **478**, 4169–4185 (2021). doi: 10.1042/BCJ20210708; pmid: 34783343
55. D. Kimanius *et al.*, Data-driven regularization lowers the size barrier of cryo-EM structure determination. *Nat. Methods* **21**, 1216–1221 (2024). doi: 10.1038/s41592-024-02304-8; pmid: 38862790
56. A. Rohou, N. Grigorieff, CTFFIND4: Fast and accurate defocus estimation from electron micrographs. *J. Struct. Biol.* **192**, 216–221 (2015). doi: 10.1016/j.jsb.2015.08.008; pmid: 26278980
57. J. Zivanov *et al.*, New tools for automated high-resolution cryo-EM structure determination in RELION-3. *eLife* **7**, e42166 (2018). doi: 10.7554/eLife.42166; pmid: 30412051
58. M. Zubradt *et al.*, DMS-MaPseq for genome-wide or targeted RNA structure probing in vivo. *Nat. Methods* **14**, 75–82 (2017). doi: 10.1038/nmeth.4057; pmid: 27819661
59. D. Mitchell III, J. Cotter, I. Saleem, A. M. Mustoe, Mutation signature filtering enables high-fidelity RNA structure probing at all four nucleobases with DMS. *Nucleic Acids Res.* **51**, 8744–8757 (2023). doi: 10.1093/nar/gkad522; pmid: 37334863
60. H. Li, Minimap2: Pairwise alignment for nucleotide sequences. *Bioinformatics* **34**, 3094–3100 (2018). doi: 10.1093/bioinformatics/bty191; pmid: 29750242
61. N. M. Forino *et al.*, Telomerase RNA structural heterogeneity in living human cells detected by DMS-MaPseq. *Nat. Commun.* **16**, 925 (2025). doi: 10.1038/s41467-025-56149-6; pmid: 39843442
62. A. Punjani, J. L. Rubinstein, D. J. Fleet, M. A. Brubaker, cryoSPARC: Algorithms for rapid unsupervised cryo-EM structure determination. *Nat. Methods* **14**, 290–296 (2017). doi: 10.1038/nmeth.4169; pmid: 28165473
63. T. Bepler *et al.*, Positive-unlabeled convolutional neural networks for particle picking in cryo-electron micrographs. *Nat. Methods* **16**, 1153–1160 (2019). doi: 10.1038/s41592-019-0575-8; pmid: 31591578
64. A. Punjani, H. Zhang, D. J. Fleet, Non-uniform refinement: Adaptive regularization improves single-particle cryo-EM reconstruction. *Nat. Methods* **17**, 1214–1221 (2020). doi: 10.1038/s41592-020-00990-8; pmid: 33257830
65. D. Asarnow, E. Palovcak, Y. Cheng, asarnow/pyem: UCSF pyem v0.5 (v0.5). **Zenodo** (2019); https://doi.org/10.5281/zenodo.3576630.
66. A. Punjani, D. J. Fleet, 3D variability analysis: Resolving continuous flexibility and discrete heterogeneity from single particle cryo-EM. *J. Struct. Biol.* **213**, 107702 (2021). doi: 10.1016/j.jsb.2021.107702; pmid: 33582281
67. J. Zivanov, T. Nakane, S. H. W. Scheres, Estimation of high-order aberrations and anisotropic magnification from cryo-EM data sets in *RELION*-3.1. *IUCrJ* **7**, 253–267 (2020). doi: 10.1107/S2052252520000081; pmid: 32148853
68. G. N. Murshudov *et al.*, REFMAC5 for the refinement of macromolecular crystal structures. *Acta Crystallogr. D Biol. Crystallogr.* **67**, 355–367 (2011). doi: 10.1107/S0907444911001314; pmid: 21460454
69. A. Brown *et al.*, Tools for macromolecular model building and refinement into electron cryo-microscopy reconstructions. *Acta Crystallogr. D Biol. Crystallogr.* **71**, 136–153 (2015). doi: 10.1107/S1399004714021683; pmid: 25615868
70. A. Casañal, B. Lohkamp, P. Emsley, Current developments in Coot for macromolecular model building of electron cryo-microscopy and crystallographic data. *Protein Sci.* **29**, 1069–1078 (2020). doi: 10.1002/pro.3791; pmid: 31730249
71. F.-C. Chou, N. Echols, T. C. Terwilliger, R. Das, RNA structure refinement using the ERRASER-Phenix pipeline. *Methods Mol. Biol.* **1320**, 269–282 (2016). doi: 10.1007/978-1-4939-2763-0_17; pmid: 26227049
72. K. Yamashita, C. M. Palmer, T. Burnley, G. N. Murshudov, Cryo-EM single-particle structure refinement and map calculation using *Servalcat*. *Acta Crystallogr. D Struct. Biol.* **77**, 1282–1291 (2021). doi: 10.1107/S2059798321009475; pmid: 34605431
73. R. A. Nicholls, M. Fischer, S. McNicholas, G. N. Murshudov, Conformation-independent structural comparison of macromolecules with *ProSMART*. *Acta Crystallogr. D Biol. Crystallogr.* **70**, 2487–2499 (2014). doi: 10.1107/S1399004714016241; pmid: 25195761
74. D. Liebschner *et al.*, Macromolecular structure determination using X-rays, neutrons and electrons: Recent developments in *Phenix*. *Acta Crystallogr. D Struct. Biol.* **75**, 861–877 (2019). doi: 10.1107/S2059798319011471; pmid: 31588918
75. C. J. Williams *et al.*, MolProbity: More and better reference data for improved all-atom structure validation. *Protein Sci.* **27**, 293–315 (2018). doi: 10.1002/pro.3330; pmid: 29067766
76. H. Martadinata, A. T. Phan, Formation of a stacked dimeric G-quadruplex containing bulges by the 5′-terminal region of human telomerase RNA (hTERC). *Biochemistry* **53**, 1595–1600 (2014). doi: 10.1021/bi4015727; pmid: 24601523
77. T. D. Goddard *et al.*, UCSF ChimeraX: Meeting modern challenges in visualization and analysis. *Protein Sci.* **27**, 14–25 (2018). doi: 10.1002/pro.3235; pmid: 28710774
78. C. Cheong, P. B. Moore, Solution structure of an unusually stable RNA tetraplex containing G- and U-quartet structures. *Biochemistry* **31**, 8406–8414 (1992). doi: 10.1021/bi00151a003; pmid: 1382577
79. G. Pintilie *et al.*, Measurement of atom resolvability in cryo-EM maps with Q-scores. *Nat. Methods* **17**, 328–334 (2020). doi: 10.1038/s41592-020-0731-1; pmid: 32042190
80. E. F. Pettersen *et al.*, UCSF Chimera—A visualization system for exploratory research and analysis. *J. Comput. Chem.* **25**, 1605–1612 (2004). doi: 10.1002/jcc.20084; pmid: 15264254

ACKNOWLEDGMENTS

We thank K. Collins and X. Zhang for sharing the HCT116 hTR knockout cell line and AAVS1 rescue plasmids and technical advice; J. Yang and D. Barford for the anaphase-promoting complex sample; D. Clift and L. James for reagents and technical advice on the nanoluciferase assays; H. Wang and M. Hegde for reagents and technical advice on telomerase in vitro reconstitution; G. Murshudov and K. Yamashita for guidance with model refinement; MRC LMB EM facility staff for access and maintenance of the EM facility; J. Grimmett, T. Darling,

and I. Clayson for maintaining the Scientific Computing facility; K. Turton and J. Shi for help with tissue and insect cell culture; the Scheres lab for RELION data processing advice; and A. Carter, K. Collins, M. Jefferies, B. Greber, H. Hu, and L. Passmore for critical reading of the manuscript. **Funding:** UKRI-Medical Research Council grant MC_UP_1201/19 (T.H.D.N.); Wellcome Trust Career Development grant 226015/Z/22/Z (T.H.D.N.); EMBO Young Investigator Program Award (T.H.D.N.); Bio-X Bowes Graduate Student Fellowship (R.C.K.); China Scholarship Council No. 202206620047 (W.Q.S.); UK Biotechnology and Biological Sciences Research Council BB/X01102X/1 (H.P.Y., Y.L.D.); Jane Coffin Childs Postdoctoral Fellowship (G.E.G.); National Institutes of Health grant NIGMS 2R35GM122579 (R.D.); Howard Hughes Medical Institute Investigator (R.D.). **Author contributions:** T.H.D.N. conceived of and supervised the project. S.B. purified samples, prepared cryo-EM grids, collected negative stain and cryo-EM data, and performed preliminary cryo-EM data analysis. Z.S. performed cryo-EM analyses for structure determination of the telomerase dimer. G.E.G. and S.T. assisted Z.S. with data analysis. T.H.D.N. analyzed the negative stain EM data. T.H.D.N. and G.E.G. performed model building and refinement. R.C.K. and R.D. performed modeling by DRRAFTER. S.B., E.F.-E., P.L., and T.H.D.N. performed all biochemical experiments. P.L. performed in-cell experiments. W.Q.S. performed DMS RNA structural probing experiments, and H.P.Y. conducted the DMS RNA structural probing data analysis. Y.L.D. supervised the DMS RNA structural probing experiments and analyses. Z.S., S.B., E.F.-E., and T.H.D.N. prepared all illustrations. T.H.D.N. wrote the first draft with input from all authors. T.H.D.N. prepared the final version of the manuscript. **Competing interests:** The authors declare that they have no competing interests. **Data and materials availability:** Cryo-EM maps are deposited in EMDB under the following accession numbers: EMD-52976 for the full dimer, EMD-52983 for the H/ACA RNP protomer, EMD-52984 for the H/ACA RNP dimer, EMD-52978 for the catalytic core obtained by symmetry expansion, EMD-52979 for catalytic core 1, EMD-52980 for catalytic core 2, EMD-52981 for catalytic core 1 using the common subset of particles, and EMD-52982 for catalytic core 2 using the common subset of particles. PDB coordinates are deposited in the Protein Data Bank under PDB IDs 9QB2 for the H/ACA RNP protomer, 9QB3 for the H/ACA RNP dimer, 9QAX for the catalytic core obtained by symmetry expansion, 9QAY for catalytic core 1, and 9QAZ for catalytic core 2. For the full dimer, the corresponding fitted models and the RNA models built by DRRAFTER (not refined) are included as a Pymol session in data S1. Q-scores of different models for the 5′ leader sequence of hTR are included in data S2. The G-quadruplex model built by DRRAFTER is included as a Pymol session in data S3. The raw nanopore sequence data of the DMS RNA structure probing data have been deposited in the European Nucleotide Archive (ENA) at EMBL-EBI under accession number PRJEB88555 (https://www.ebi.ac.uk/ena/browser/view/PRJEB88555). Materials are available from T.H.D.N. under a material transfer agreement with the MRC Laboratory of Molecular Biology. This research was funded in whole or in part by UK Research and Innovation (MC_UP_1201/19) and Wellcome Trust (226015/Z/22/Z), cOAlition S organizations. The author will make the Author Accepted Manuscript (AAM) version available under a CC BY public copyright license.

SUPPLEMENTARY MATERIALS

science.org/doi/10.1126/science.adr5817
Figs. S1 to S20; Tables S1 to S3; References (*81*–*83*); MDAR Reproducibility Checklist; Movie S1; Data S1 to S3

Submitted 9 July 2024; accepted 29 April 2025

10.1126/science.adr5817

Science
AAAS

Supplementary Materials for

Cryo-EM structure of human telomerase dimer reveals H/ACA RNP-mediated dimerization

Sebastian Balch *et al*.

Corresponding author: Thi Hoang Duong Nguyen, knguyen@mrc-lmb.cam.ac.uk

Science **389**, eadr5817 (2025)
DOI: 10.1126/science.adr5817

The PDF file includes:

Other Supplementary Material for this manuscript includes the following:

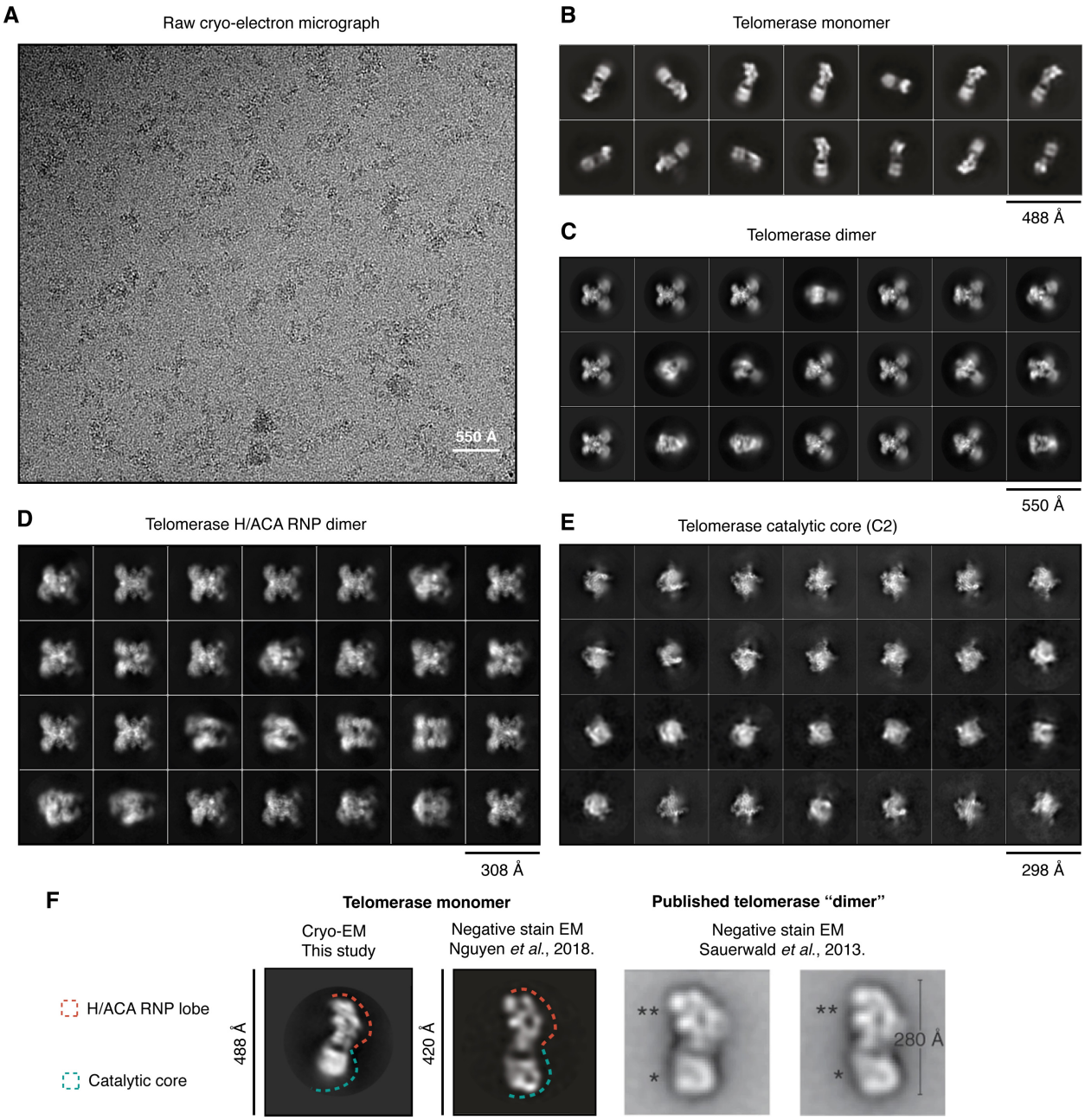

Fig. S1. Representative cryo-EM data.

(A) Representative cryo-EM micrograph. **(B to E)** Cryo-EM 2D class averages of the full monomeric telomerase (B), full dimeric telomerase (C), telomerase H/ACA RNP dimer (D), and catalytic core (E) from the dimeric telomerase, respectively. **(F)** Comparison of the cryo-EM and negative stain EM 2D class averages of the human telomerase monomer from this study and a previous study (*8*) with those of the published negative stain EM structure of the proposed dimer of TERT and hTR (*17*).

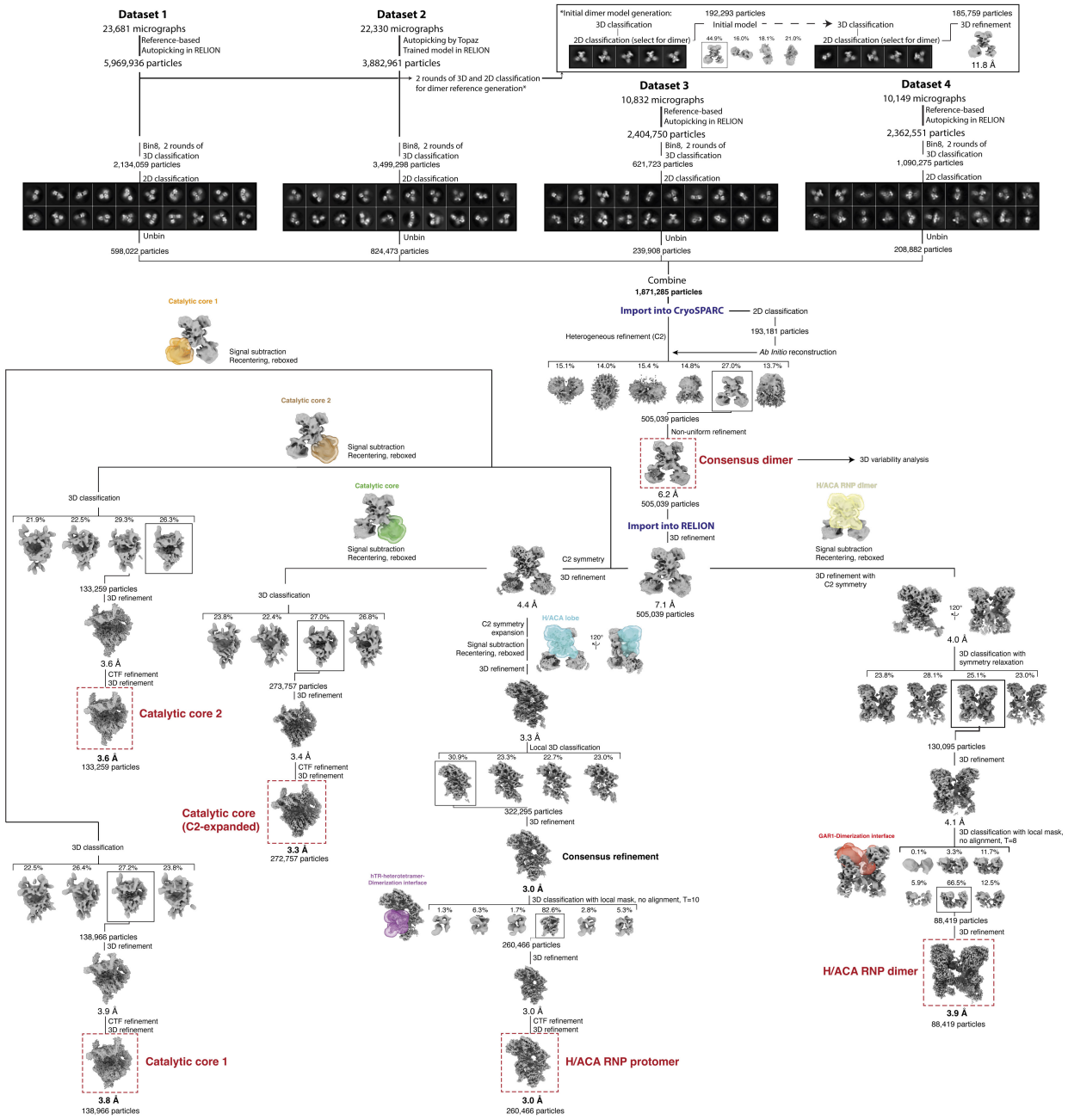

Fig. S2. Cryo-EM data processing.

Image processing strategies to obtain the maps presented in this study. Red boxes and labels indicate maps discussed in the main text.

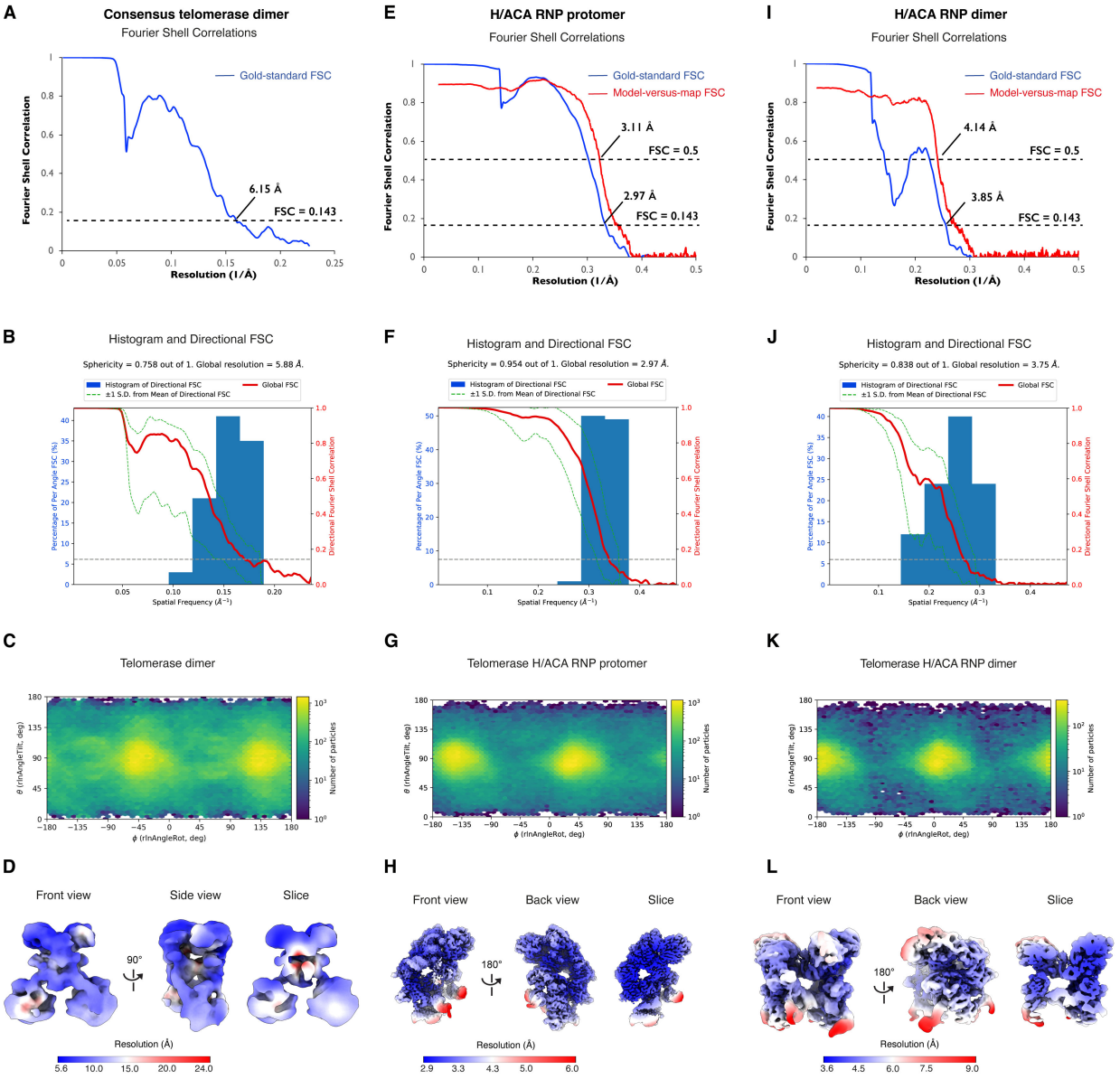

Fig. S3. Overall and local resolution estimation for the full telomerase dimer, the H/ACA RNP protomer and the H/ACA RNP dimer.

(A, E, I) Model-versus-map (red) and gold-standard (blue) FSC plots for the full telomerase dimer ((A) - only gold-standard FSC plot), telomerase H/ACA RNP protomer (E) and telomerase H/ACA RNP dimer (I). The resolution was estimated at FSC = 0.5 (model-versus-map) and FSC = 0.143 (gold-standard). **(B, F, J)** Directional FSC plots and sphericity values are presented for the full telomerase dimer (B), telomerase H/ACA RNP protomer (F) and telomerase H/ACA RNP dimer (J) (*81*). Directional FSC plots were generated using a 3D-FSC server (https://3dfsc.salk.edu). **(C, G, K)** 2D histograms depict the Euler angles of particles used for reconstructions of the full telomerase dimer (C), telomerase H/ACA RNP protomer (G) and telomerase H/ACA RNP dimer (K). Histograms were plotted using a Python script (https://githubhelp.com/Guillawme/angdist). **(D, H, L)** Local resolution of the full telomerase dimer (D), telomerase H/ACA RNP protomer (H)

and telomerase H/ACA RNP dimer (L) maps. RELION 5.0 was used to generate local resolution estimation.

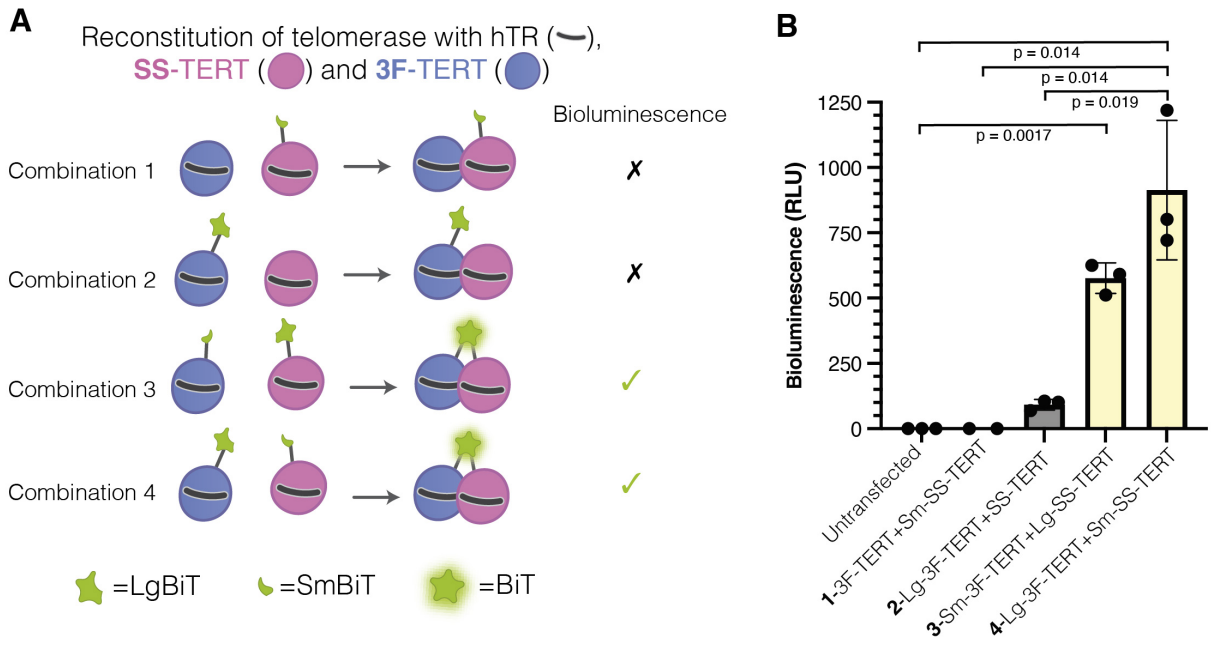

Fig. S4. Split nano-luciferase assays.

(A) Schematic of the split nano-luciferase assays. Four combinations of TERT constructs were co-transfected with hTR into HEK293T cells as shown. Bioluminescence is obtained when the LgBiT and SmBiT fragments of nano-luciferase are in close proximity. **(B)** Analysis of the bioluminescence from the nano-luciferase assays for the different combinations of TERT constructs co-transfected with hTR as shown in (A). Experiments were done in triplicates. Error bars represent the standard error of the mean (SEM), and significant p values are also reported.

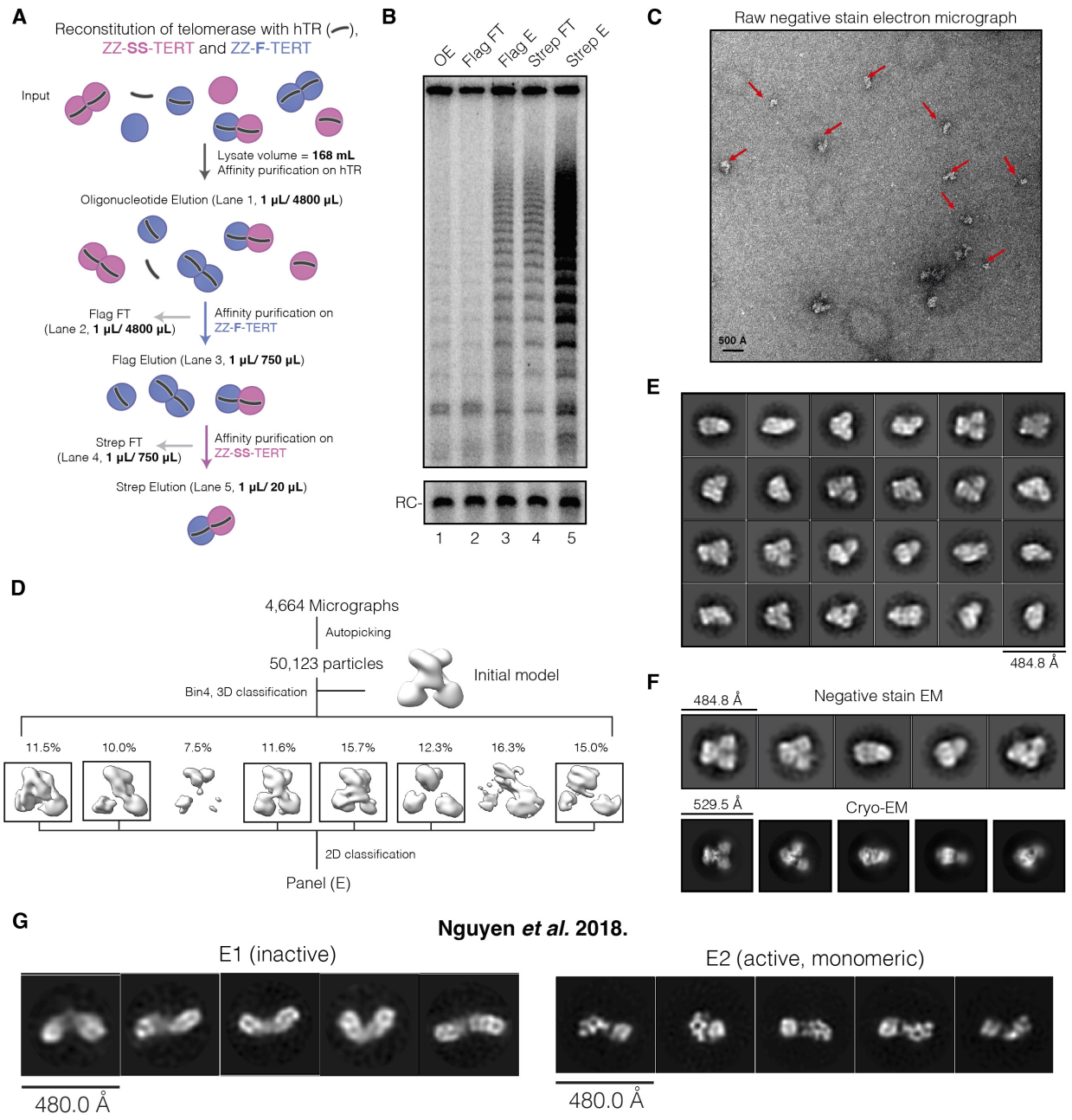

Fig. S5. Biochemical reconstitution and characterization of the human telomerase holoenzyme dimer.

(A) Schematic of the biochemical purification to isolate dual-tagged dimeric telomerase. Samples were collected for telomerase activity assays shown in (B). 1 µL of sample at different steps of the purification was collected for telomerase activity assays. The total volume of telomerase samples at these different steps is also indicated. **(B)** Telomerase activity assays of the samples collected in (A). OE, oligonucleotide elution; Flag FT, Flag flow-through; Flag E, Flag elution; Strep FT, Strep-Tactin flow-through; Strep E, Strep-Tactin elution. **(C)** Representative negative stain EM image of telomerase with both Flag and Strep tags resulting from the purification strategy shown in (A). **(D)** Negative stain EM data processing strategy for the purified dual-tagged telomerase sample shown

in (C). **(E)** 2D class averages of telomerase complexes resulting from Strep E shown in (A). **(F)** Comparison between representative negative stain 2D class averages of the purified dual-tagged telomerase particles and the cryo-EM 2D class averages of the telomerase dimer. **(G)** Representative negative stain EM 2D class averages of two fractions of telomerase with different activities from a previous study (*8*). These fractions resulted from biotin elution of telomerase from magnetic Strep-Tactin resin. The first elution fraction (E1) is inactive and has a different structural morphology to the second elution fraction (E2), which is active and has monomeric TERT/hTR composition and additional holoenzyme factors.

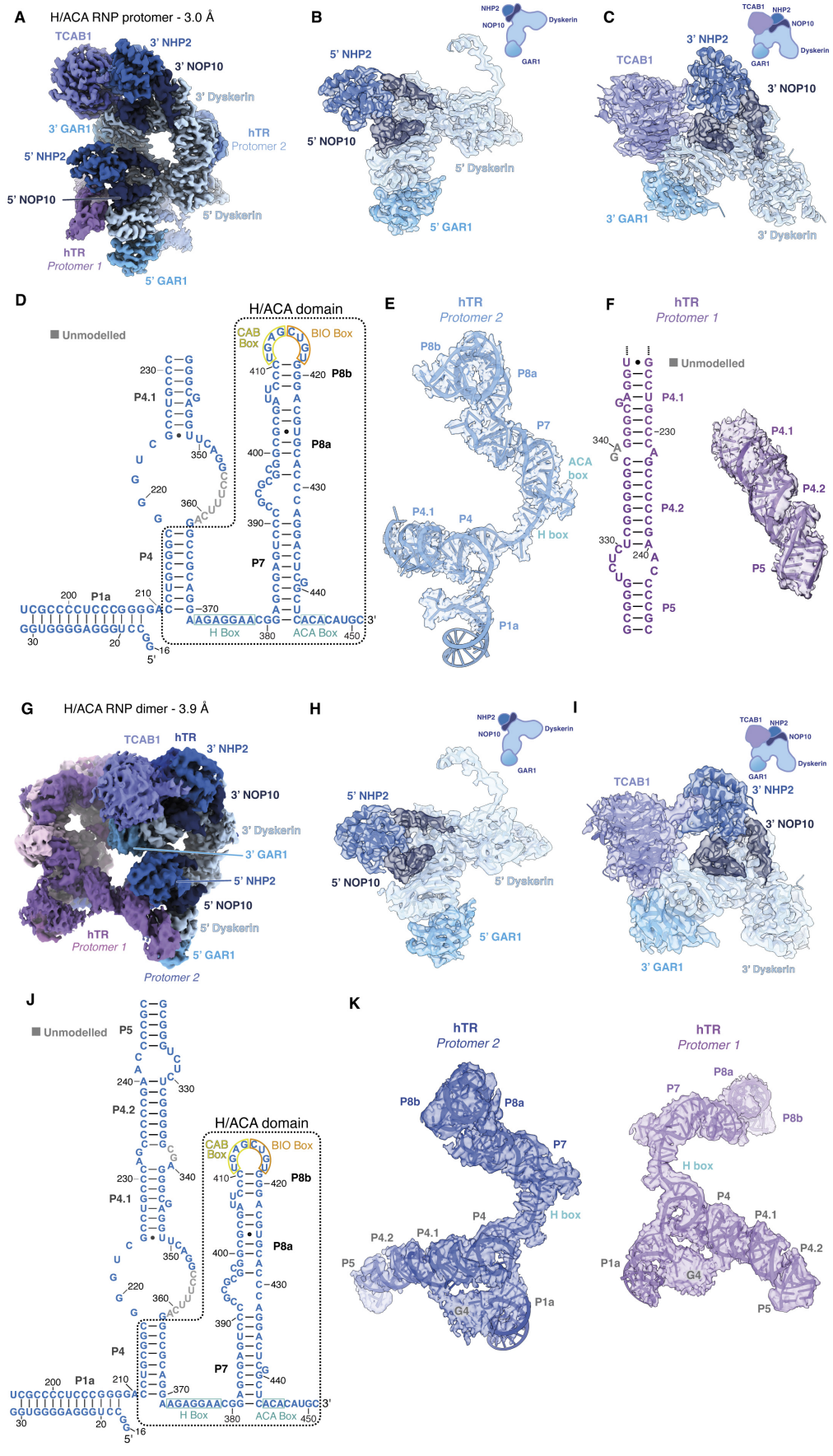
A
H/ACA RNP protomer - 3.0 Å
TCAB1
3' NHP2
3' NOP10
3' Dyskerin
3' GAR1
hTR
Protomer 2
5' NHP2
5' NOP10
5' Dyskerin
hTR
Protomer 1
5' GAR1
B
NHP2
NOP10
Dyskerin
GAR1
5' NHP2
5' NOP10
5' Dyskerin
5' GAR1
C
TCAB1
NHP2
NOP10
Dyskerin
GAR1
3' NHP2
TCAB1
3' NOP10
3' GAR1
3' Dyskerin
D
Unmodelled
H/ACA domain
CAB Box
BIO Box
P8b
P8a
P4.1
P4
P7
P1a
H Box
ACA Box
E
hTR
Protomer 2
P8b
P8a
P7
ACA box
P4.1
P4
H box
P1a
F
hTR
Protomer 1
Unmodelled
P4.1
P4.2
P5
G
H/ACA RNP dimer - 3.9 Å
TCAB1
hTR
3' NHP2
3' NOP10
3' Dyskerin
3' GAR1
5' NHP2
5' NOP10
5' Dyskerin
hTR
Protomer 1
5' GAR1
Protomer 2
H
NHP2
NOP10
Dyskerin
GAR1
5' NHP2
5' NOP10
5' Dyskerin
5' GAR1
I
TCAB1
NHP2
NOP10
Dyskerin
GAR1
3' NHP2
3' NOP10
3' GAR1
3' Dyskerin
J
Unmodelled
P5
P4.2
P4.1
H/ACA domain
CAB Box
BIO Box
P8b
P8a
P4
P7
P1a
H Box
ACA Box
K
hTR
Protomer 2
P8b
P8a
P7
P4
H box
P4.2
P4.1
P5
P1a
G4
hTR
Protomer 1
P8a
P7
P8b
H box
P4
P4.1
P1a
G4
P4.2
P5

Fig. S6. Representative cryo-EM density of the 3.0 Å H/ACA RNP protomer and the 3.9 Å H/ACA RNP dimer map.

(A) 3.0 Å cryo-EM density of the H/ACA RNP lobe of a single protomer in the telomerase dimer. **(B)** Model fitted into the map of the 5' H/ACA heterotetramer of the H/ACA RNP protomer. **(C)** Model fitted into the map of the 3' H/ACA heterotetramer and TCAB1 of the H/ACA RNP protomer. **(D)** Schematic of hTR modelled in the H/ACA RNP protomer. The H/ACA domain of hTR is labelled in with a dashed box. **(E)** Model of hTR from protomer 2 fitted into the cryo-EM density of the H/ACA RNP protomer. **(F)** Schematic and model-map fit of the P4/P5 linker of hTR from the protomer 1 that interacts with H/ACA proteins of protomer 2. **(G)** 3.9 Å cryo-EM density map of the H/ACA RNP dimer. Only protomer 2 is labelled for simplicity. **(H)** Model of the 5' H/ACA heterotetramer of protomer 2 fitted into the 3.9 Å H/ACA RNP dimer map. **(I)** Model of the 3' H/ACA heterotetramer and TCAB1 of protomer 2 fitted into the 3.9 Å H/ACA RNP dimer map. **(J)** Schematic of hTR modelled into the H/ACA RNP dimer. **(K)** Models of hTR from both protomers of the H/ACA RNP dimer fitted into the 3.9 Å H/ACA RNP dimer map. G4, G quadruplex.

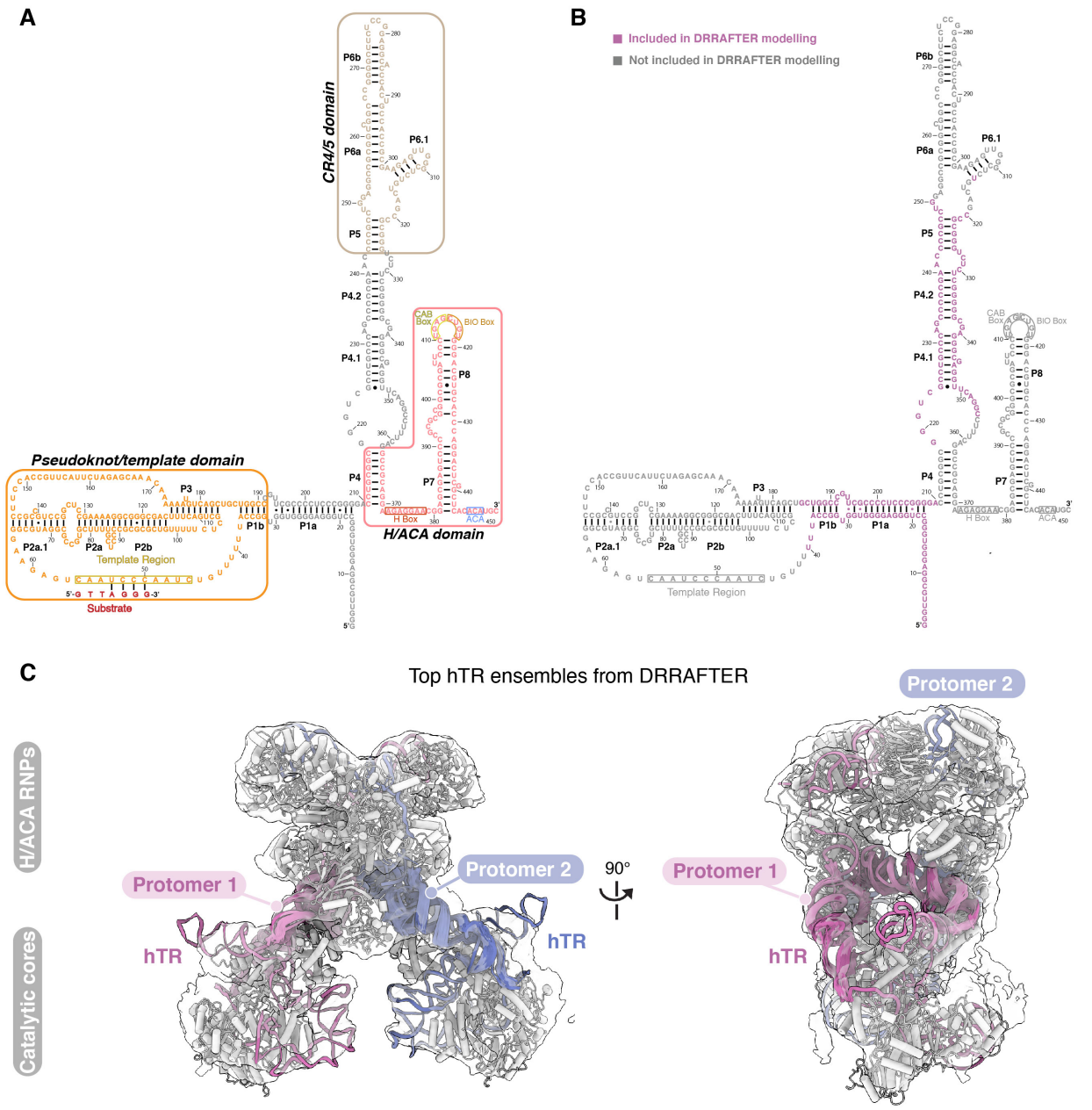

Fig. S7. DRRAFTER modeling of telomerase RNA in the full telomerase dimer.
(A) Sequence and secondary structure of hTR. The pseudoknot/template, CR4/5 and H/ACA domains are colored as indicated. **(B)** Sequence and secondary structure of hTR with regions included in DRRAFTER modeling colored in magenta. **(C)** The top DRRAFTER models of hTR in the full telomerase dimer using the 6.2 Å resolution map. DRRAFTER was performed on hTR of both protomers. Also see Data S1.

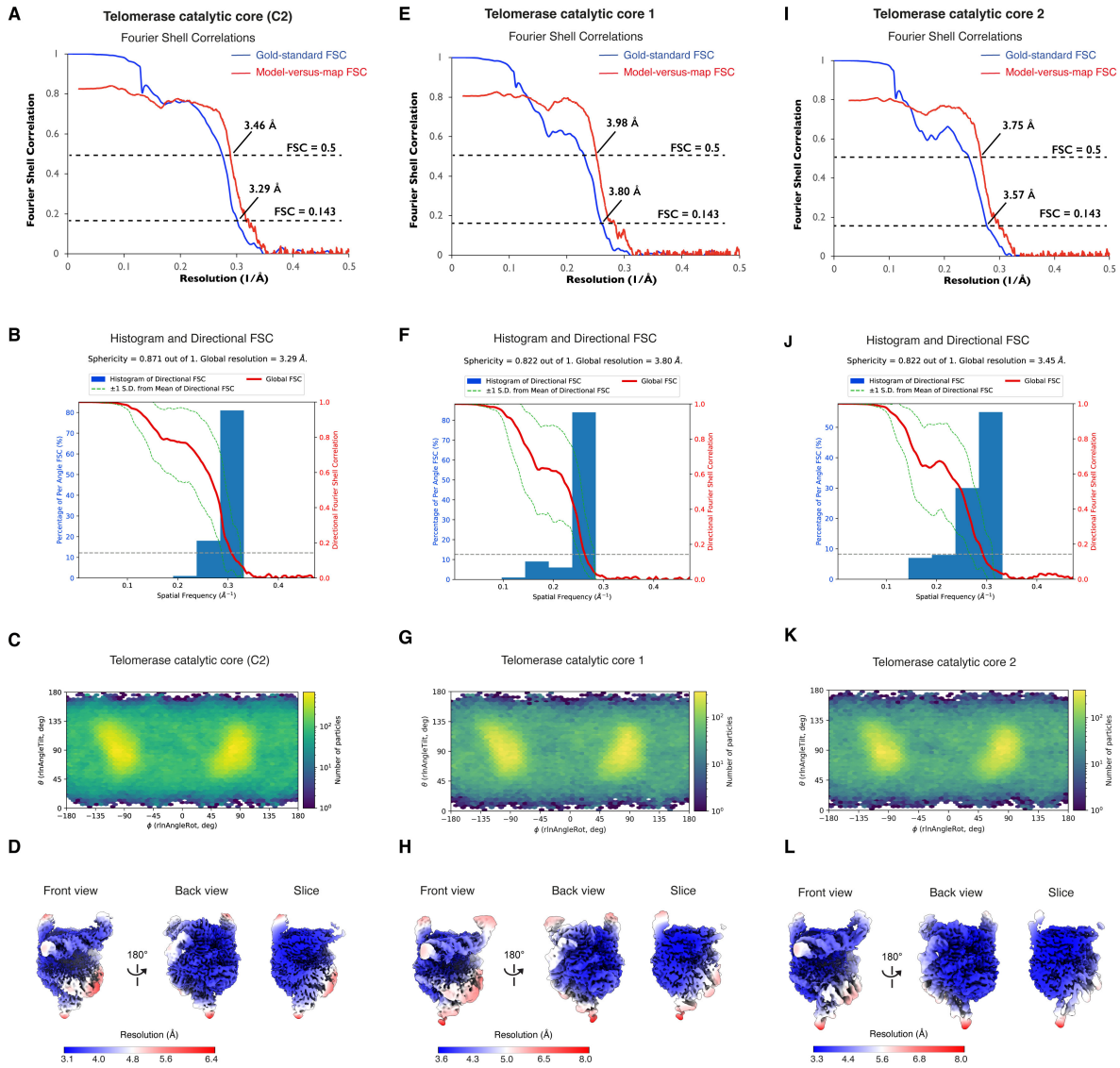

Fig. S8. Overall and local resolution estimation for the telomerase catalytic cores.
(A, E, I) Model-versus-map (red) and gold-standard (blue) FSC plots for the telomerase catalytic core (from the C2 symmetry expanded particle stack (C2)) (A), telomerase catalytic core 1 (E) and telomerase catalytic core 2 (I) for the full telomerase dimer. The resolution was estimated at FSC = 0.5 (model-versus-map) and FSC = 0.143 (gold-standard). **(B, F, J)** Directional FSC plots and sphericity values are presented for the telomerase catalytic core (C2) (B), telomerase catalytic core 1 (F) and telomerase catalytic core 2 (J) (*81*). Directional FSC plots were generated using a 3D-FSC server (https://3dfsc.salk.edu). **(C, G, K)** 2D histograms depict the Euler angles of particles used for reconstructions of the telomerase catalytic core (C2) (C), telomerase catalytic core 1 (G) and telomerase catalytic core 2 (K). Histograms were plotted using a Python script (https://githubhelp.com/Guillawme/angdist). **(D, H, L)** Local resolution of the telomerase catalytic core (C2) (D), telomerase catalytic core 1 (H) and telomerase catalytic core 2 (L) maps. RELION 5.0 was used to generate local resolution estimation.

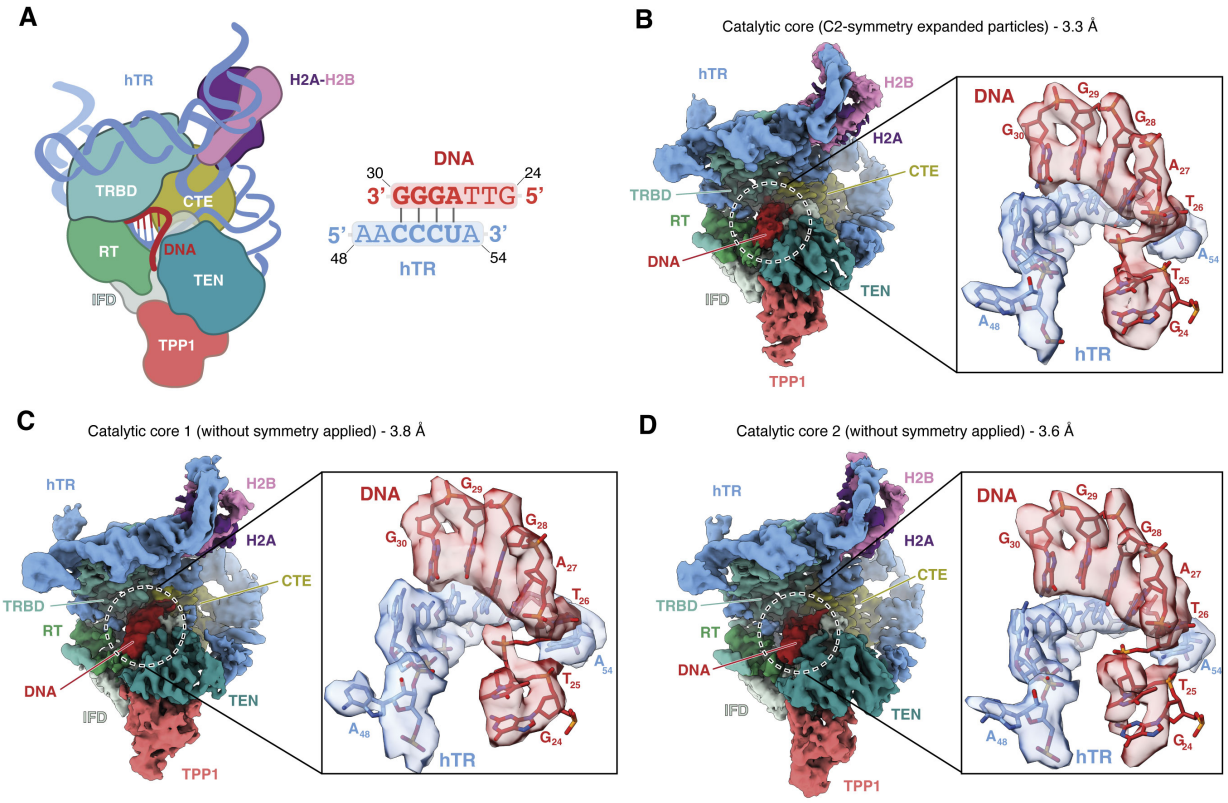

Fig. S9. Representative cryo-EM densities of the telomerase catalytic cores.
(A) Schematic of the human telomerase catalytic core with the shelterin subunit TPP1. A schematic of the RNA-DNA duplex in the active site is also shown. Human TERT subunit is divided into domains by colors. TEN, telomerase essential N-terminal; TRBD, telomerase RNA binding domain; RT, reverse transcriptase; IFD, insertion in the fingers domain; CTE, C-terminal extension; hTR, human telomerase RNA. **(B)** Cryo-EM density of the telomerase catalytic core obtained from the C2 symmetry expanded particle stack at 3.3 Å resolution. Subunits are colored and labelled as in (A). **(C)** Cryo-EM density of the catalytic core 1 of the human telomerase dimer at 3.8 Å resolution. **(D)** Cryo-EM density of the catalytic core 2 of the human telomerase dimer at 3.6 Å resolution. Insets in (B) to (D) show close-up views of the RNA-DNA duplex with the model fitted to the corresponding semi-transparent cryo-EM map.

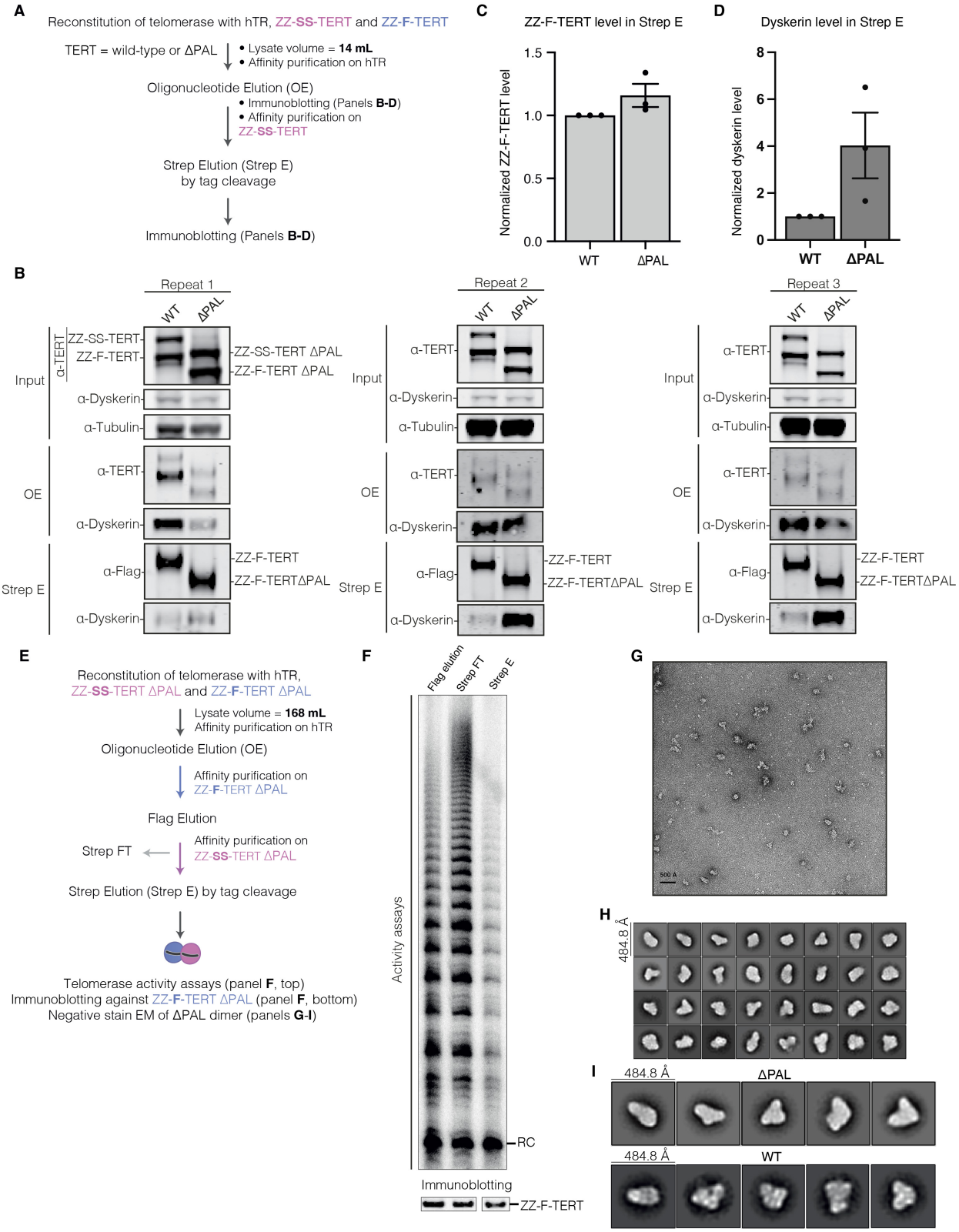

Fig. S10. Deleting the PAL of TERT does not affect dimer formation.

(A) Schematic of the two-step purification strategy to examine the ability of the TERT ΔPAL mutant to form the telomerase dimer. A 1:1 mixture of ZZ-SS-TERT and ZZ-F-TERT was co-

transfected with hTR, followed by O-purification and Strep-Tactin pulldown. The Flag signal in Strep E was used as a readout for dimer formation. The same experiment was also performed for wild-type (WT) TERT for comparison. **(B)** Triplicates of immunoblotting experiments of the input lysates (input), OE and Strep E from the purification of WT and ΔPAL TERT as shown in (A). **(C)** Bar graph showing the levels of ZZ-F-TERT in the Strep E fractions of the WT and ΔPAL purification. The signal of ZZ-F-TERT in the ΔPAL mutant was normalized against the WT signal. Error bars represent the standard error of the mean (SEM) (n = 3). **(D)** Bar graph showing the levels of dyskerin in the Strep E fractions for the WT and ΔPAL purification. The signal of dyskerin in the ΔPAL mutant was normalized against the WT signal. Error bars represent the standard error of the mean (SEM) (n = 3). **(E)** Schematic of the three-step purification strategy to isolate the ΔPAL mutant dimer for activity assays, immunoblotting and negative stain EM. **(F)** Telomerase activity assay (top panel) and immunoblotting (bottom panel) of samples from the Flag elution, the Strep flow-through (Strep FT) and the Strep E resulting from the purification of the ΔPAL mutant dimer as shown in (E). RC, recovery control. **(G)** Representative negative stain EM image of the purified ΔPAL mutant dimer. **(H)** Negative stain 2D class averages of the ΔPAL mutant dimer purified as shown in (E). **(I)** Comparison of representative negative stain 2D class averages of the purified ΔPAL mutant dimer (top) and the WT dimer (bottom).

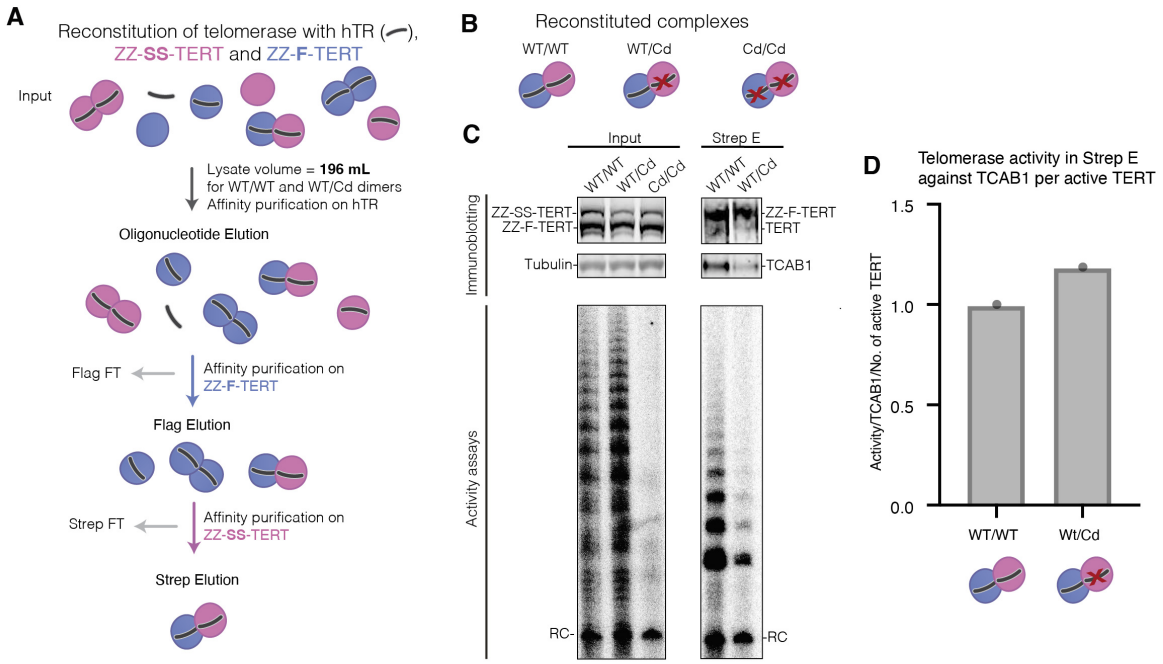

Fig. S11. Functional independence of the two catalytic cores within the telomerase dimer. **(A)** Schematic of the three-step purification strategy to isolate the dual-tagged telomerase with different TERT constructs. **(B)** Schematic of the three reconstituted telomerase complexes: one with both WT TERT (WT/WT), one with one WT TERT and one catalytically dead (Cd) TERT (WT/Cd), and one with both Cd TERT (Cd/Cd). We used the strategy shown in (A) to purify the WT/WT and WT/Cd dimers. The Cd/Cd reconstitution was only used as a negative control and not purified. **(C)** Immunoblotting (top panels) and telomerase activity assay (bottom panels) of the input lysates for the WT/WT, WT/Cd and Cd/Cd telomerase reconstitutions and the WT/WT and WT/Cd dimers purified as shown in (A). RC, recovery control. **(D)** Bar graph showing quantification of telomerase activity of the purified WT/WT and WT/Cd dimers. Telomerase activity was first normalized against the RC and then against TCAB1 per active TERT molecule (2 for WT/WT and 1 for WT/Cd). The normalized activity of the WT/Cd dimer is then normalized against the WT/WT dimer. Untagged TERT and ZZ-F-TERT should be present at an equal molar ratio using the three-step purification strategy shown in (A). However, the Proteintech TERT antibody gave weaker signals for the untagged TERT. TERT and TCAB1 are present at a 1:1 stoichiometry in telomerase. Thus, we used TCAB1 signal instead of TERT for quantification.

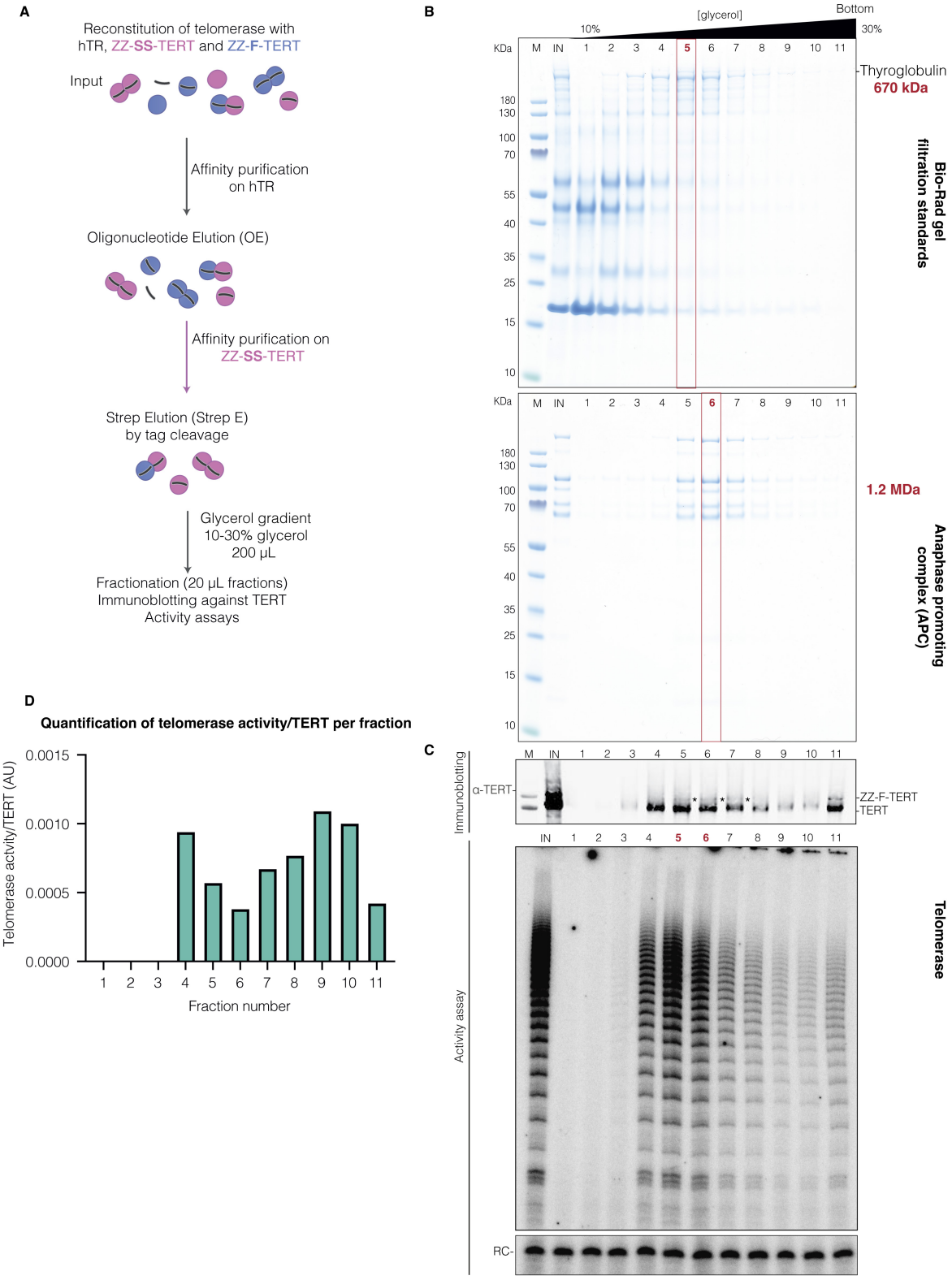

Fig. S12. Glycerol gradient centrifugation suggests that dimer formation did not enhance telomerase activity.

(A) Schematic of the biochemical strategy to separate the monomeric and dimeric telomerase complexes by glycerol gradient. Telomerase was reconstituted using ZZ-SS-TERT, ZZ-F-TERT and hTR, followed by O-purification and Strep-Tactin pulldown. The resulting Strep E sample would contain a mixture of monomeric (major) and dimeric (minor) telomerase complexes, which were separated by a 10-30% glycerol gradient. **(B)** Coomassie-stained SDS-PAGE of the input (IN) and fractions from 10-30% glycerol gradients of Bio-Rad gel filtration standards (top) and the anaphase promoting complex (APC) (bottom) as size markers. Thyroglobulin (670 KDa), with a size similar to the telomerase monomer, peaks at fraction 5. The APC complex (1.2 MDa), with a size similar to the telomerase dimer, peaks at fraction 6. The molecular weight markers are labelled as M. **(C)** Immunoblotting (top) and telomerase activity assay (bottom) of the input and fractions from a 10-30% glycerol gradient for Strep E sample from the two-step purification as shown in (A). Based on the size markers shown in (B), fractions 5 and 6 correspond to where the telomerase monomer and dimer peak, respectively. The signal of the ZZ-F-TERT in the fractions is an indicator of the dimeric complexes. Due to the low abundance of the dimer, these ZZ-F-TERT signal is weak and thus marked with asterisks on the right side of the bands. **(D)** Bar graph showing the quantification of telomerase activity per TERT across the fractions from the glycerol gradient of Strep E. Due to the overlap of the monomer and dimer peaks, we quantified the telomerase activity against TERT signals. If there was cooperativity between the two catalytic cores, we would observe more activity per TERT in the dimer peak fraction. However, we did not observe this trend, suggesting that dimer formation does not lead to increase in activity. These experiments could not be performed in triplicates due to the discontinuation of a commercial TERT antibody used for the immunoblotting experiment.

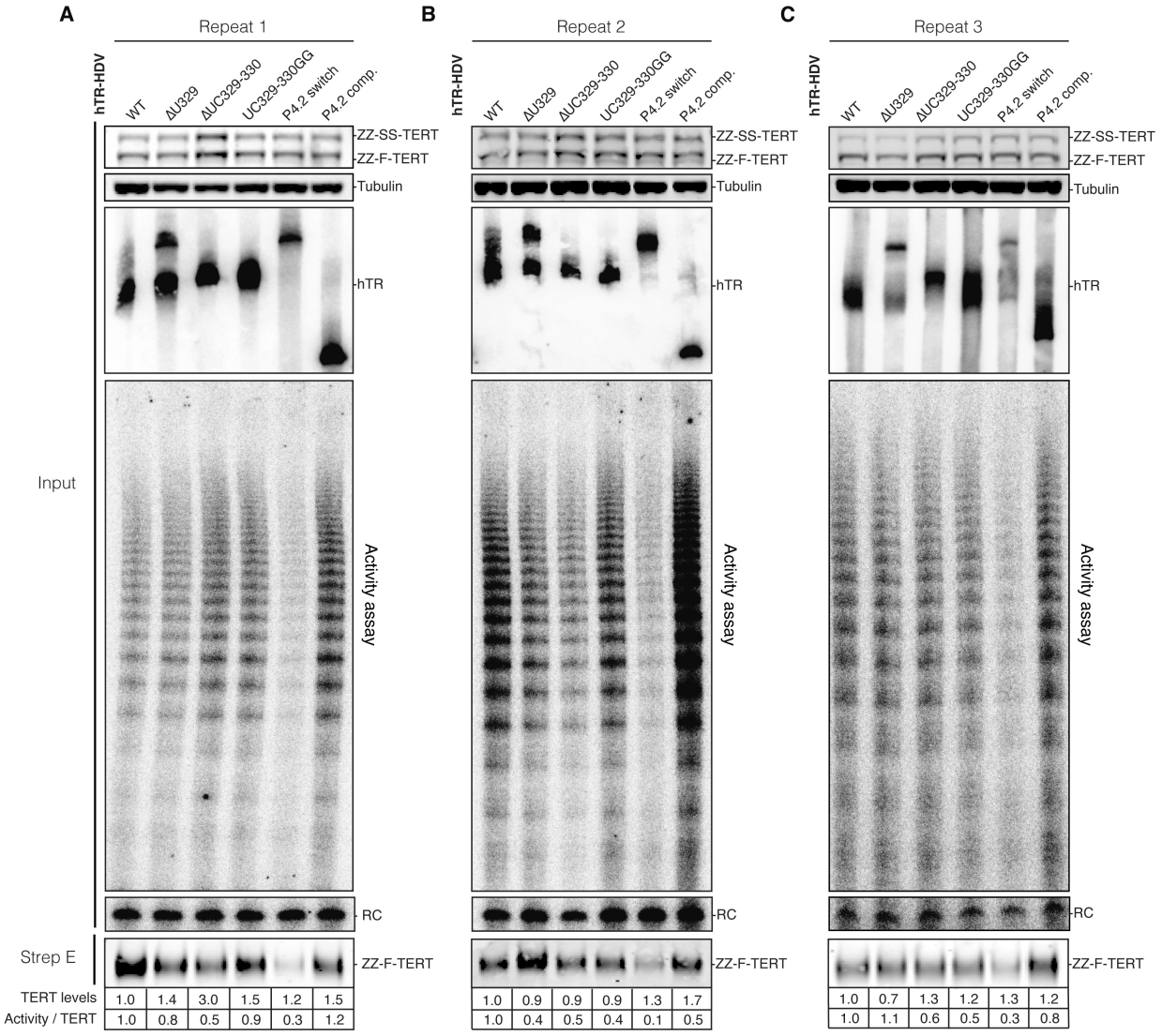

Fig. S13. Mutations in the P4.2/P5 linker region of hTR that disrupt dimer formation reduce telomerase activity.

(A to C) Triplicates of experiments characterizing the effects of disrupting the P4/5 linker regions of hTR. In this experiment, WT and mutant hTR constructs were reconstituted with ZZ-SS-TERT and ZZ-F-TERT. Telomerase was purified as shown in Fig. 1D; and the signal of ZZ-F-TERT in the Strep E was probed by immunoblotting as a readout for dimer formation. Also see Fig. 4B for quantification.

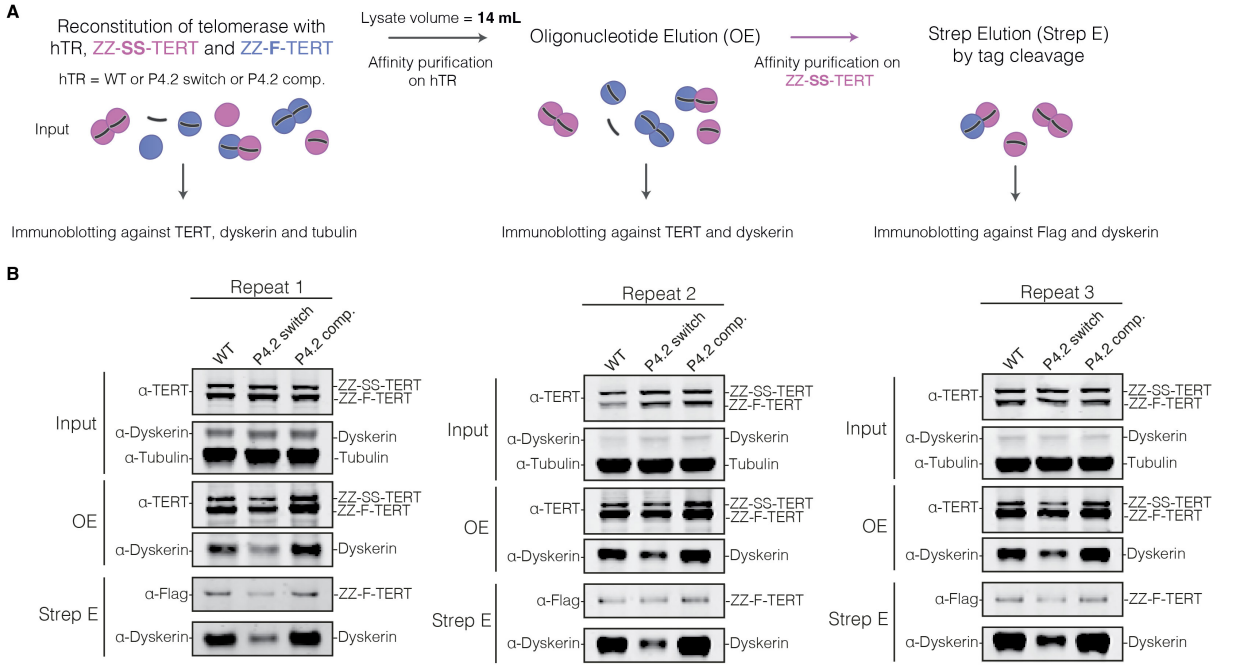

Fig. S14. Disrupting the P4.2 stem of hTR severely reduces binding of dyskerin.
(A) Schematic of the biochemical strategy to dissect the effects of disrupting the P4.2 stem of hTR for the data shown in Fig. 4D. Each of hTR construct, either WT or P4.2 switch or P4.2 comp. mutant, was reconstituted with a mixture of ZZ-SS-TERT and ZZ-F-TERT. Telomerase was purified via the O-purification and Strep-Tactin pulldown. Samples were analyzed by immunoblotting at each step of the purification. **(B)** Triplicates of the immunoblotting experiments of the input lysates (input), OE and Strep E from the purification strategy shown in (A). See Fig. 4, E to H for quantification.

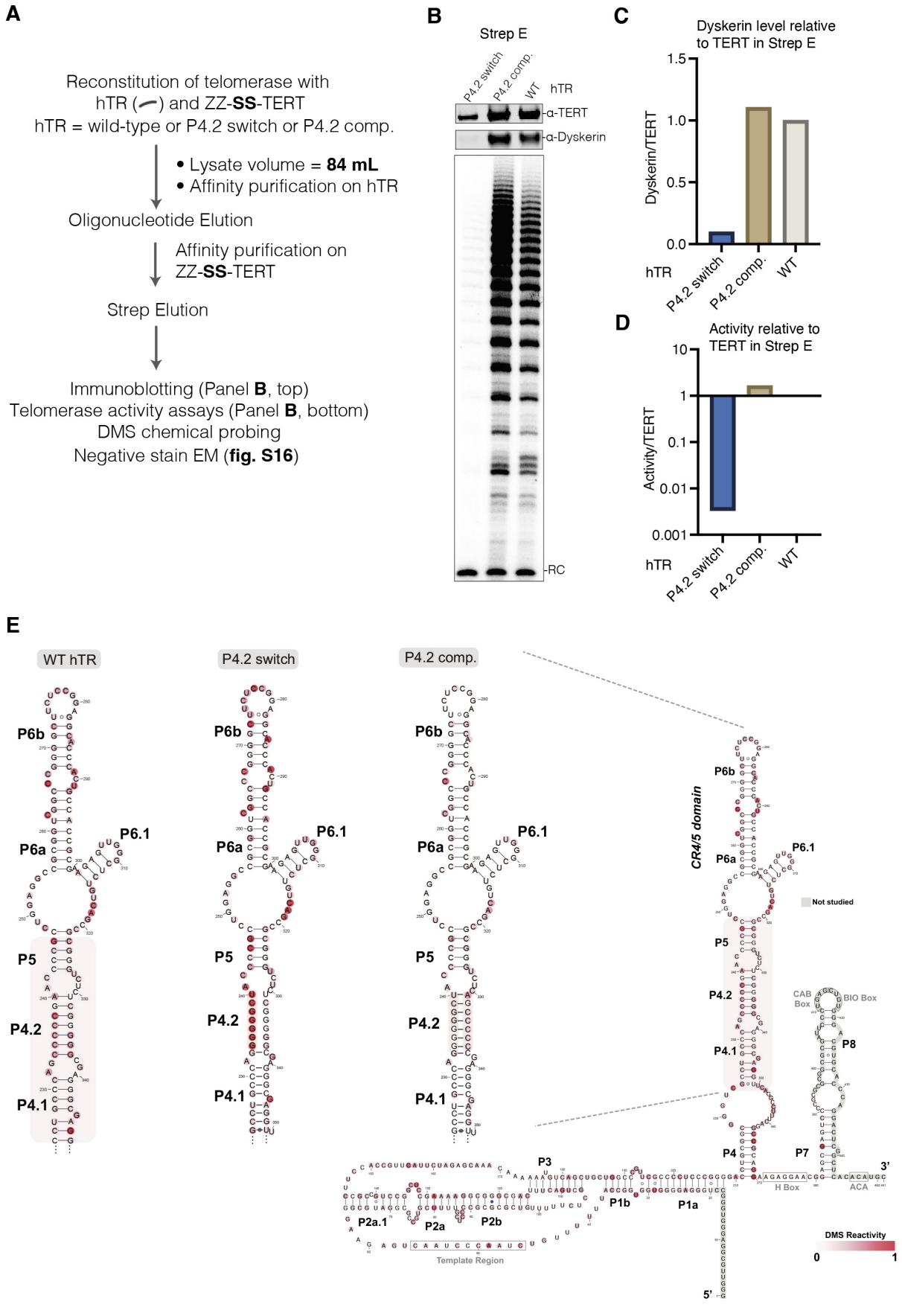
A
Reconstitution of telomerase with
hTR (—) and ZZ-SS-TERT
hTR = wild-type or P4.2 switch or P4.2 comp.
• Lysate volume = 84 mL
• Affinity purification on hTR
Oligonucleotide Elution
Affinity purification on
ZZ-SS-TERT
Strep Elution
Immunoblotting (Panel B, top)
Telomerase activity assays (Panel B, bottom)
DMS chemical probing
Negative stain EM (fig. S16)
B
Strep E
P4.2 switch
P4.2 comp.
WT
hTR
α-TERT
α-Dyskerin
RC
C
Dyskerin level relative
to TERT in Strep E
Dyskerin/TERT
1.5
1.0
0.5
0.0
hTR
P4.2 switch
P4.2 comp.
WT
D
Activity relative to
TERT in Strep E
Activity/TERT
10
1
0.1
0.01
0.001
hTR
P4.2 switch
P4.2 comp.
WT
E
WT hTR
P4.2 switch
P4.2 comp.
P6b
P6.1
P6a
P5
P4.2
P4.1
CR4/5 domain
Not studied
P3
P1b
P1a
P2a.1
P2a
P2b
Template Region
P4
P7
CAB Box
BIO Box
P8
H Box
ACA
3'
5'
DMS Reactivity
0
1

Fig. S15. Characterization of telomerase reconstituted with P4.2 switch and P4.2 comp. hTR mutants.

(A) Schematic of the strategy to characterize telomerase reconstituted with either WT, P4.2 switch and P4.2 comp. constructs of hTR. WT hTR and the two P4.2 hTR mutants were reconstituted with ZZ-SS-TERT, followed by O-purification and Strep-Tactin pulldown to obtain purified bulk telomerase. The Strep E sample was subjected to immunoblotting, telomerase activity assay, DMS chemical probing and negative staining EM (fig. S16). **(B)** Immunoblotting (top) and telomerase activity assay of the purified telomerase with WT hTR and the P4.2 switch and P4.2 comp. hTR mutants. RC, recovery control. **(C)** Bar graph showing the level of dyskerin relative to TERT in the Strep E fractions of telomerase reconstituted with either WT hTR, the P4.2 switch or P4.2 comp. hTR mutant. Levels were normalized against the telomerase sample with WT hTR. **(D)** Bar graph showing the level of telomerase activity per TERT for the Strep E fractions of telomerase reconstituted with WT hTR, the P4.2 switch or P4.2 comp. hTR mutant. Levels were normalized against the telomerase sample with WT hTR. The Y-axis is shown in $\log_{10}$-scale due to the low level of telomerase activity in the P4.2 switch mutant. **(E)** DMS chemical probing of human telomerase RNA in the purified telomerase complexes reconstituted with the WT, the P4.2 switch and the P4.2 comp. mutant constructs of hTR. Samples were purified as shown in (A). The overall RNA secondary structure of the WT hTR in the purified complex with DMS reactivities is shown. The RNA secondary structures across the P4.1 and P4.2 stems and the CR4/5 region with DMS reactivities in the WT hTR and the P4.2 switch and P4.2 comp. mutants are shown in the close-up views. RNA regions that are used for the two primer-binding sites and that are close to the 5’ and 3’ ends cannot be assessed; these regions are shaded with a light grey box.

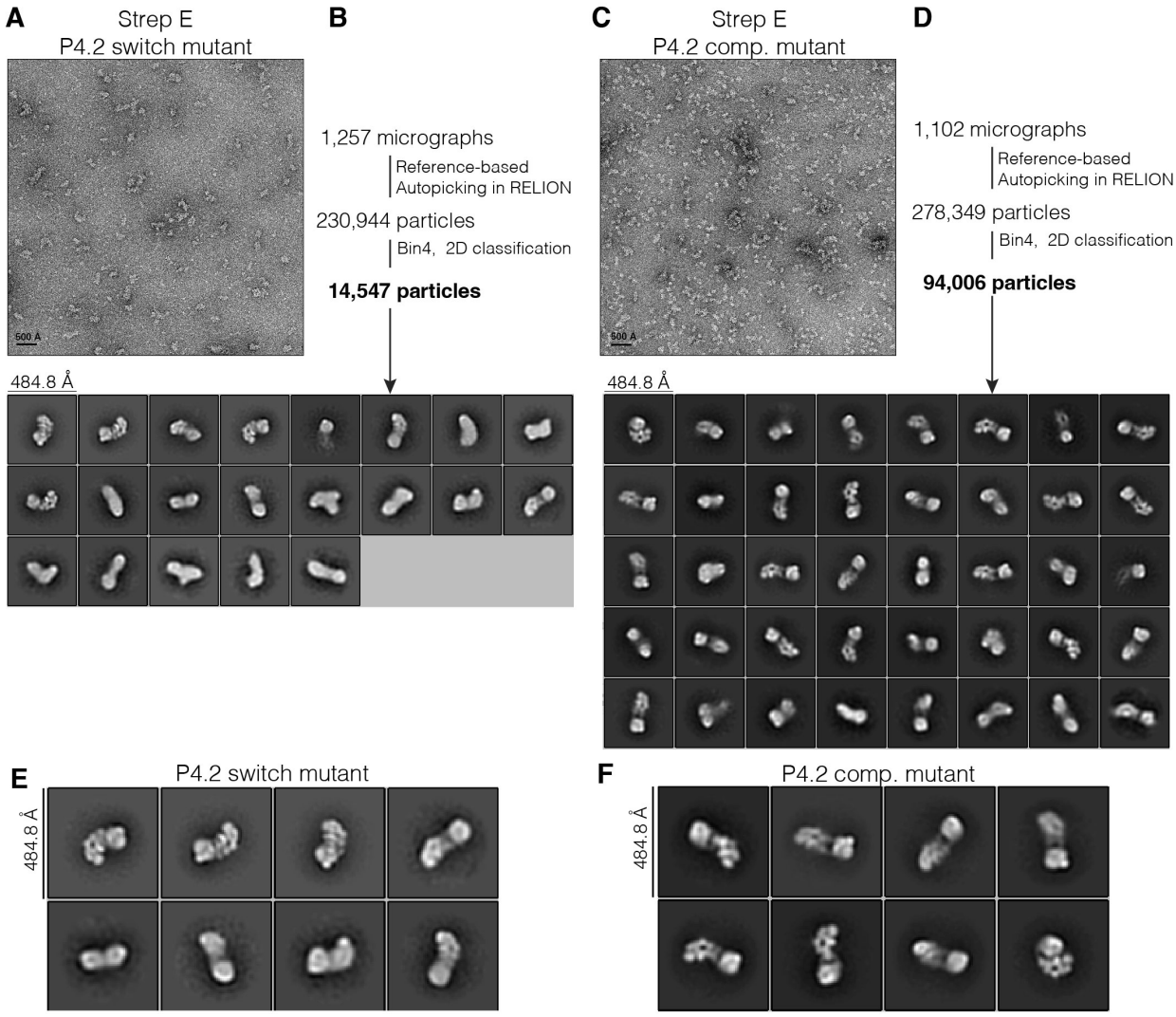

Fig. S16. Visualization of the purified hTR P4.2 switch and P4.2 comp. telomerase mutants by negative stain EM.

(A) Representative negative stain EM image of the telomerase P4.2 switch hTR mutant purified using the schematic shown in fig. S15A. **(B)** Data processing strategy to obtain the 2D class averages for the telomerase P4.2 switch hTR mutant. **(C)** Representative negative stain EM image of the telomerase P4.2 comp. hTR mutant purified using the schematic shown in fig. S15A. **(D)** Data processing strategy to obtain the 2D class averages for the telomerase P4.2 comp. hTR mutant. **(E and F)** Representative negative stain EM 2D class averages for the P4.2 switch and P4.2 comp. hTR mutants, respectively, for comparison.

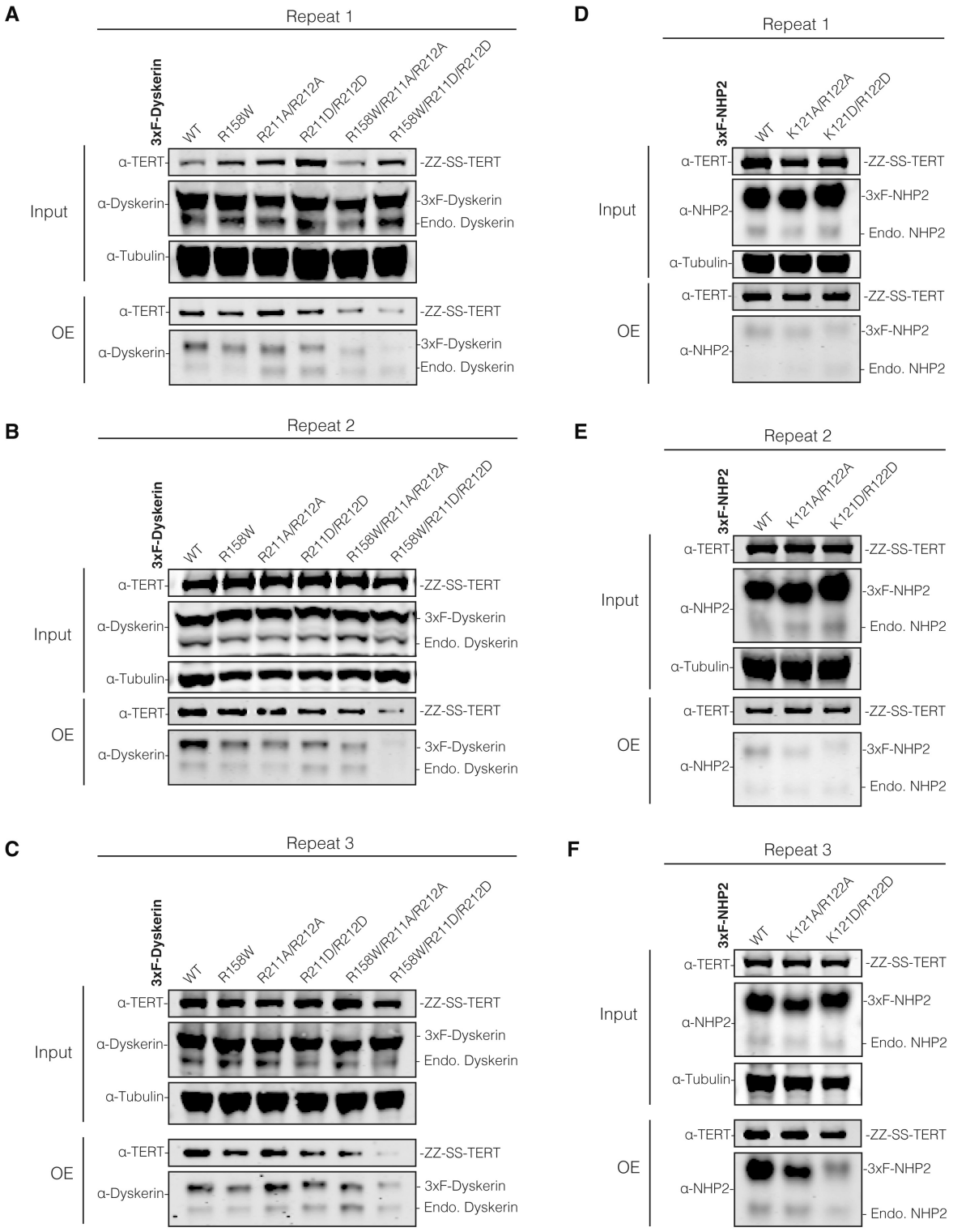

Fig. S17. Mutations of dyskerin and NHP2 that disrupt dimerization result in defects in telomerase incorporation.

(A to C) Triplicates of experiments in which residues crucial for dimerization in dyskerin were mutated and reconstituted with TERT and hTR. **(D to F)** Triplicates of experiments in which residues crucial for dimerization in NHP2 were mutated and reconstituted with TERT and hTR. In

all experiments, telomerase was purified via hTR using O-purification. The amounts of the overexpressed WT and mutant dyskerin or NHP2 relative to the corresponding endogenous protein were compared to test for incorporation defects. Also see Fig. 5, E and F for quantification.

A

Dyskerin sequence

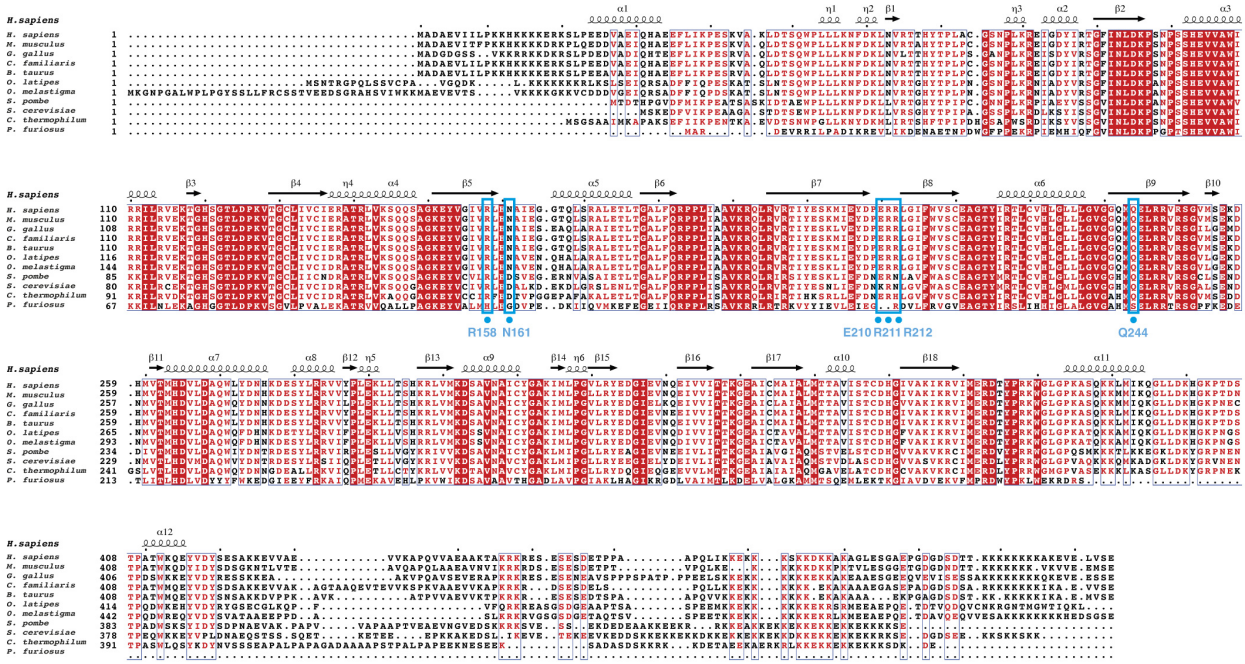

B

GAR1 sequence

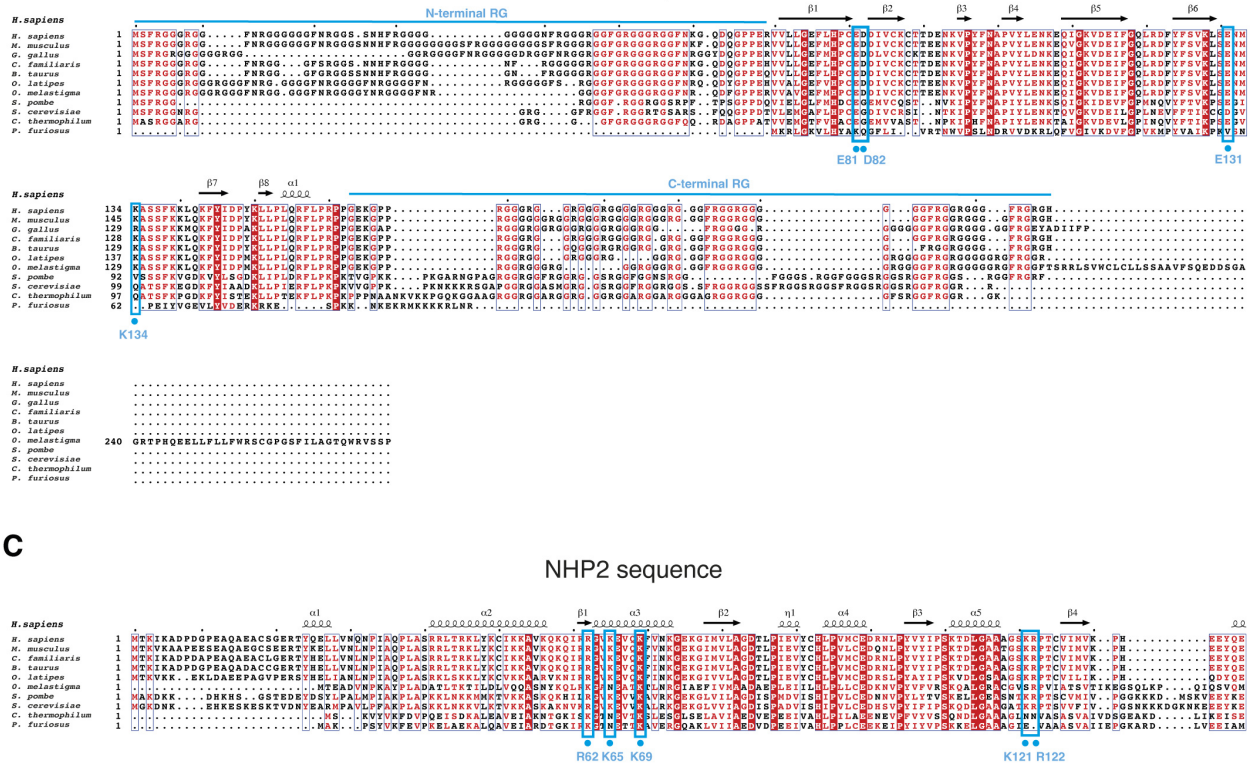

C

NHP2 sequence

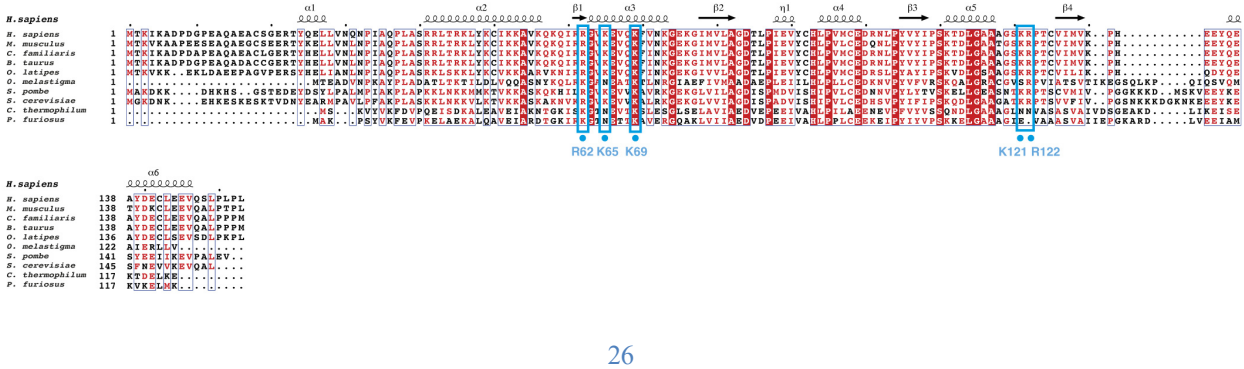

Fig. S18. Sequence alignments of dyskerin, GAR1 and NHP2.

(A) to **(C)** Sequence alignments of dyskerin (A), GAR1 (B), and NHP2 (C). Sequences of dyskerin and GAR1 from 11 species, and NHP2 from 10 species, were obtained from UniProt and aligned using Clustal Omega (*82*). ESPript 3.0 was utilized for the visualization of aligned sequences (*83*). Residues with 70% sequence conservation are colored, with red boxes indicating absolute conservation. Residues highlighted in the text and figures are labelled with a blue box and a blue dot.

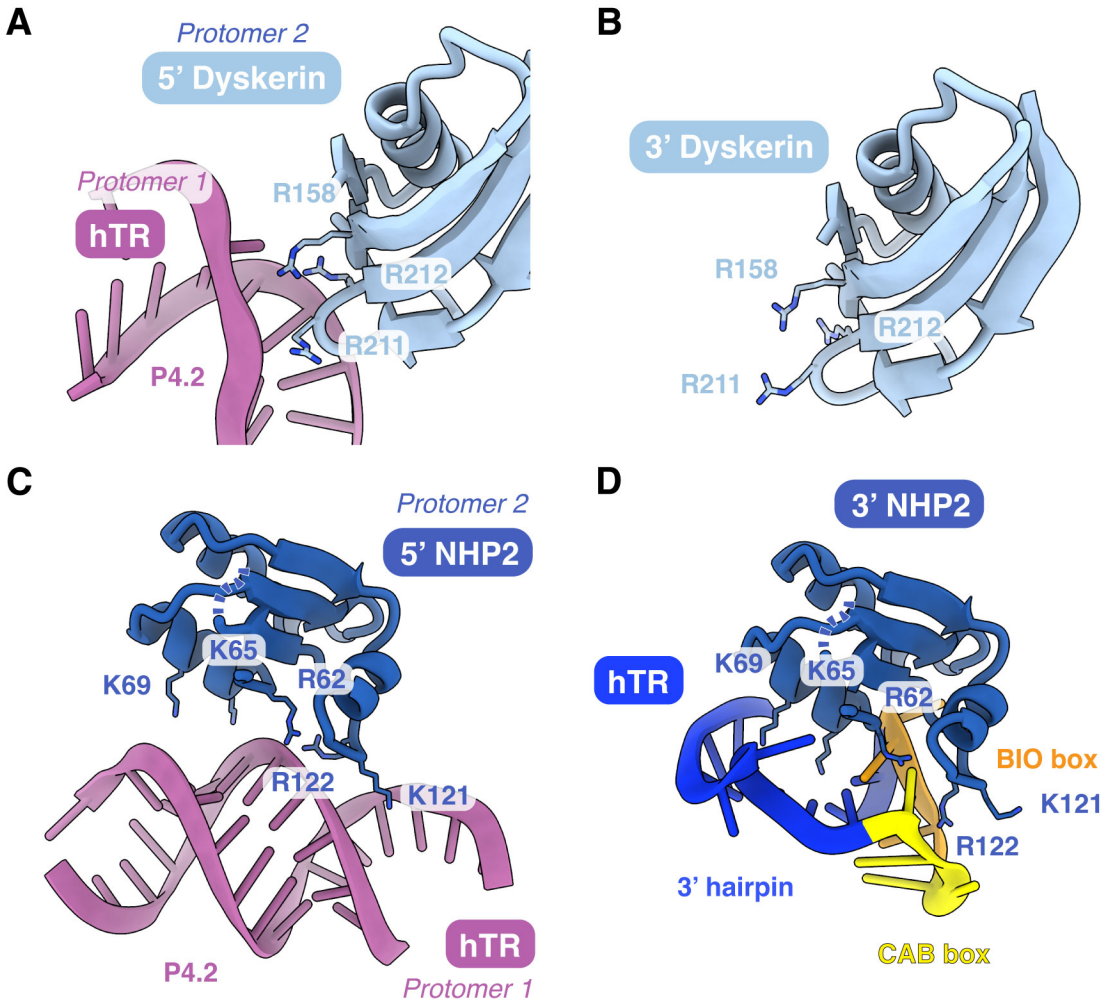

Fig. S19. hTR interaction with NHP2 and dyskerin of the 5' and 3' H/ACA heterotetramers. **(A)** Interaction between hTR of H/ACA RNP protomer 1 and the 5' dyskerin of H/ACA RNP protomer 2. **(B)** The 3' dyskerin surface equivalent to the one shown in (A). This region does not form interactions with the 3' H/ACA hairpin of hTR. **(C)** Interaction between hTR of H/ACA RNP protomer 1 and the 5' NHP2 of H/ACA RNP protomer 2. **(D)** Interaction between the 3' hairpin of hTR and the 3' NHP2, showing the same region of NHP2 as shown in (C).

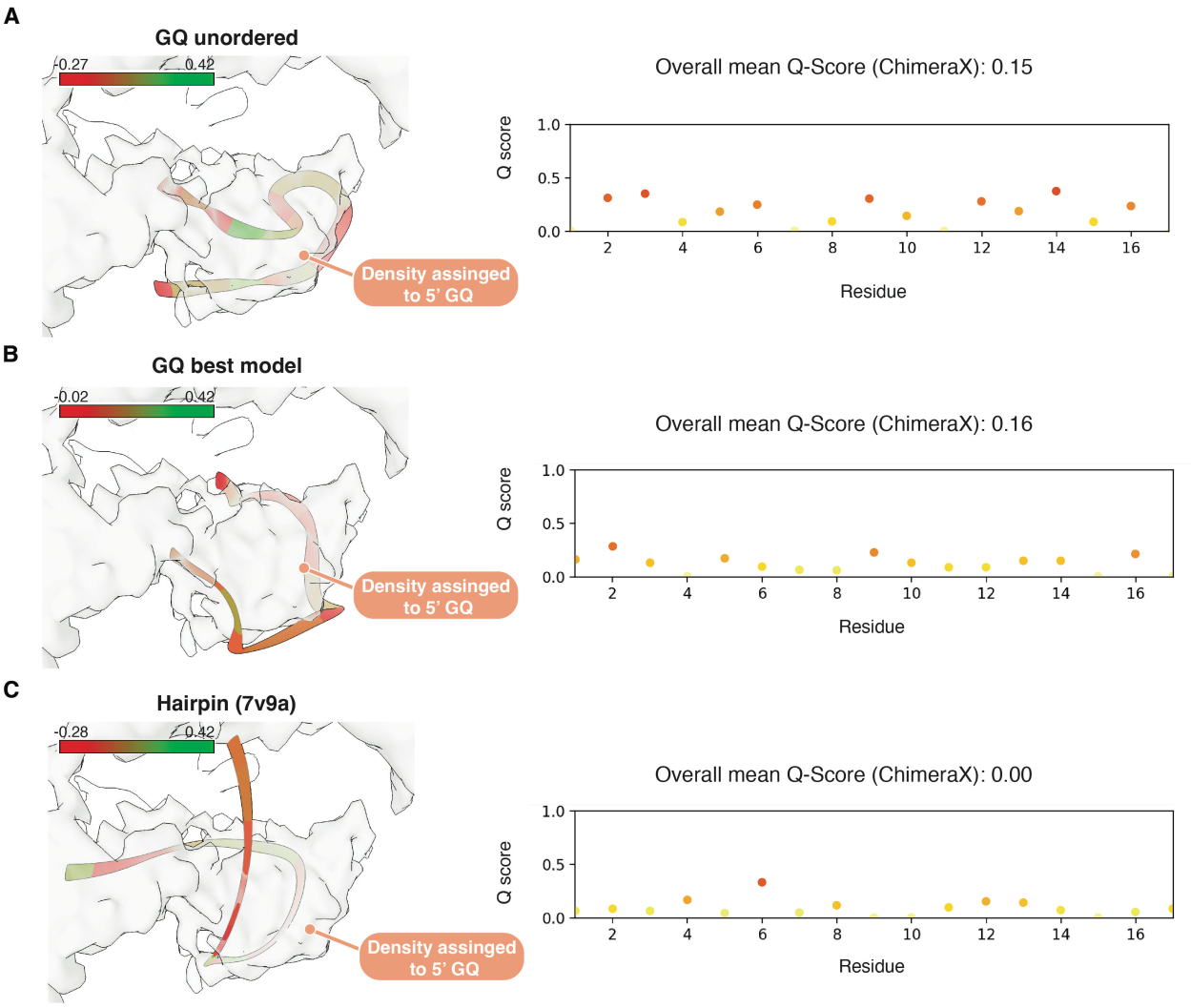

Fig. S20. Q-scores for the 5' leader sequence modelled as unordered 5' GQ, ordered 5' GQ, and 5' hairpin.

(A to C) Unordered model, ordered 5' GQ (best fit), and 5' hairpin (PDB 7V9A), respectively, fitted within the 3.9 Å H/ACA RNP dimer map and colored by the backbone Q-scores generated in UCSF Chimera (*10, 79, 80*). The right panels show the backbone Q-scores for individual residues (nucleotides 1–17 of hTR), generated and visualized in UCSF ChimeraX (*77, 79*).

Table S1. Cryo-EM data collection, refinement and statistics for the consensus map and the H/ACA RNP.

	Consensus dimer	H/ACA RNP protomer	H/ACA RNP dimer
		PDB 9QB2	PDB 9QB3
	EMD-52976	EMD-52983	EMD-52984
Data collection and Processing			
Microscope		Titan Krios G3i	
Voltage (keV)		300	
Camera		Gatan K3	
Magnification		81,000; 45,782	
Pixel size at detector (Å/pixel)		1.059	
Total electron exposure (e^{-}/Å^2)		47–50	
Exposure rate (e-/ Å^2/sec)		15.66	
Number of frames		48	
Defocus range (μm)		0.8–2.4	
Automation software		EPU	
Energy filter slit width		20 eV	
Micrographs collected (no.)		66,992	
Total extracted particles (no.)		14,236,535	
For each reconstruction:			
Final particles (no.)	505,039	260,466	88,419
Point-group	C1	C1	C2
Estimated error (translations/rotations)		0.554/1.116	0.822/1.233
Resolution (global, Å)	6.2	3.0	3.9
FSC 0.5 (unmasked/masked)	9.3/7.8	4.1/3.3	6.7/4.3
FSC 0.143 (unmasked/masked)	7.6/6.2	3.4/3.0	4.3/3.9
Resolution range (local, Å)	5.6–24.0	2.9–8.2	3.7–10.8
3DFSC Sphericity	0.758	0.954	0.838
Map sharpening *B* factor (Å^2)	NA	-100	-50
Map sharpening methods	RELION5.0	RELION5.0	RELION5.0
Model composition			
Protein (residues)	NA	1674	3348
RNA/DNA (nucleotides)	NA	297	372
Model Refinement			
Refinement package	NA	Servalcat/REFMAC5.8	Servalcat/REFMAC5.8
- real or reciprocal space	NA	Reciprocal Space	Reciprocal Space
- resolution cutoff	NA	0.5	0.5
Model-Map scores	NA		
- CCvolume/mask	NA	0.75/0.75	0.76/0.78
B factors (Å^2)			
Protein residues (min/max/mean)	NA	34.97/444.10/123.31	39.53/721.76/269.62
RNA/DNA (min/max/mean)	NA	33.03/580.27/303.75	5349.50/636.00/373.95
R.m.s. deviations from ideal values			
Bond lengths (Å) (#>4σ)	NA	0.009 (1)	0.009 (1)
Bond angles (°) (#>4σ)	NA	1.287 (4)	1.297 (17)
Validation			
MolProbity score	NA	0.82	0.93
CaBLAM outliers (%)	NA	1.17%	2.6%
Clashscore	NA	1.13	1.73
Poor rotamers (%)	NA	0.27	0.27
C-beta deviations (%)	NA	0	0
EMRinger score	NA	3.79	1.01
Ramachandran plot	NA		
Favored (%)	NA	98.18	98.06
Outliers (%)	NA	0	0

Table S2. Cryo-EM map and model refinement, and validation statistics for the catalytic core

	Catalytic Core protomer with symmetry expansion PDB 9QAX EMD-52978	**Catalytic Core Protomer 1** PDB 9QAY EMD-52979	**Catalytic Core Protomer 2** PDB 9QAZ EMD-52980	**Catalytic Core Protomer 1 (shared subset)** EMD-52981	**Catalytic Core Protomer 2 (shared subset)** EMD-52982
For each reconstruction:					
Final particles (no.)	272,757	138,966	133,259	41,195	41,195
Point-group	C1	C1	C1	C1	C1
Estimated error (translations/rotations)	0.756/1.502	0.831/1.807	0.772/1.591	0.892/1.95	0.821/1.74
Resolution (global, Å)	3.3	3.8	3.6	4.1	3.9
FSC 0.5 (unmasked/masked)	4.2/3.7	6.8/4.3	6.9/4.0	8.5/6.1	8.6/6.1
FSC 0.143 (unmasked/masked)	3.7/3.3	4.1/3.8	4.0/3.6	4.6/4.1	4.3/3.9
Resolution range (local, Å)	3.1–6.4	3.7–8.0	3.3–8.0	3.9–9.8	3.6–11.9
3DFSC Sphericity	0.871	0.822	0.822	0.760	0.786
Map sharpening *B* factor (Å^2)	-40	-50	-50	-70	-70
Map sharpening methods	RELION5.0	RELION5.0	RELION5.0		
Model composition					
Protein (residues)	1247	1247	1247		
RNA/DNA (nucleotides)	260	260	260		
Model Refinement					
Refinement package	Servalcat/REFMAC5.8	Servalcat/REFMAC5.8	Servalcat/REFMAC5.8		
- real or reciprocal space	Reciprocal Space	Reciprocal Space	Reciprocal Space		
- resolution cutoff	0.5	0.5	0.5		
Model-Map scores	3.5	4.0	3.7		
- CCvolume/mask	0.76/0.77	0.75/0.76	0.73/0.74		
B factors (Å^2)					
Protein residues (min/max/mean)	37.23/964.00/278.33	39.80/999.00/314.56	38.08/999.00/281.70		
RNA/DNA (min/max/mean)	41.48/999.00/324.40	41.08/999.00/351.00	46.37/999.00/358.74		
R.m.s. deviations from ideal values					
Bond lengths (Å) (#>4σ)	0.009 (0)	0.009 (0)	0.009 (0)		
Bond angles (°) (#>4σ)	1.203 (5)	1.228 (8)	1.232 (6)		
Validation					
MolProbity score	1.81	1.81	1.82		
CaBLAM outliers (%)	2.9%	2.73%	2.9%		
Clashscore	6.76	6.94	6.97		
Poor rotamers (%)	0.09	0.09	0.09		
C-beta deviations (%)	0.09	0.17	0.09		
EMRinger score	0.94	0.39	1.03		

Ramachandran plot			
Favored (%)	93.32	93.40	93.32
Outliers (%)	0.41	0.41	0.41

Table S3.

Sequences of DNA primers used for mutagenesis of hTR, TERT, dyskerin and NHP2.

Construct	Mutation	Primers
pcDNA3.1-U3-hTR-HDV	ΔU329	5'CTCGGGGGCGAGGGC3'
		5'GACCCGCGGCTGACAG3'
pcDNA3.1-U3-hTR-HDV	ΔUC329–330	5'TCGGGGGCGAGGGCG3'
		5'GACCCGCGGCTGACAGAG3'
pcDNA3.1-U3-hTR-HDV	UC329–330GG	5'GCCGCGGGTCGGTCGGGGGCGA3'
		5'TGACAGAGCCCAACTCTTCG3'
pcDNA3.1-U3-hTR-HDV	P4.2 switch	5'GGCTACCCCGCCTGGAGGC3'
		5'CCCCTGGGCAGGCGACCC3'
pcDNA3.1-U3-hTR-HDV	P4.2 comp.	5'CCCCCGAGGGCGAGGTTCAG3'
		5'GCTGAGACCCGCGGCTGAC3'
pcDNA3.1-3xFlag-dyskerin	R158W	5'GGGGATTGTCTGGCTGCACAA3'
		5'ACATACTCTTTGCCTGCACTC3'
pcDNA3.1-3xFlag-dyskerin	R211A & R212A	5'CGATCCTGAAGCGGCTTTAGGAATCTTTTGGG3'
		5'TATTCAATCATTTTGCTCTCG3'
pcDNA3.1-3xFlag-dyskerin	R211D & R212D	5'CGATCCTGAAGATGACTTAGGAATCTTTTGGGTG3'
		5'TATTCAATCATTTTGCTCTCG3'
pcDNA3.1-3xFlag-NHP2	K121A & R122A	5'CGCAGGCTCCGCGGCTCCCACCTGTGTGATAATG3'
		5'GCTGCACCCAGGTCCG3'
pcDNA3.1-3xFlag-NHP2	K121D & R122D	5'CGCAGGCTCCGACGATCCCACCTGTGTGATAATGG TCAAG3'
		5'GCTGCACCCAGGTCCG3'
pcDNA3.1-SmBiT-ZZ-TEV-twin-Strep-SUMO*-TERT	WT	5'GCTGGCTAGCGCTGCCACCATGGTCACCGGCTACC GG3'
		5'CGCGTTTTGTTGTTCTTTGTTGAATTTGTTGTCCAC TCCAGAACTTCCACCTCC3'
pcDNA3.1-LgBiT-ZZ-TEV-twin-Strep-SUMO*-TERT	WT	5'GCTGGCTAGCGCTGCCACCATGGTGTTCACCCTGG AAGATTTC3'
		5'CGCGTTTTGTTGTTCTTTGTTGAATTTGTTGTCCAC GGATCCACTTCCACCTCC3'
pcDNA3.1-SmBiT-ZZ-TEV-3xFlag-TERT	WT	5'GCTGGCTAGCGCTGCCACCATGGTCACCGGCTACC GG3'
		5'CGCGTTTTGTTGTTCTTTGTTGAATTTGTTGTCCAC TCCAGAACTTCCACCTCC3'
pcDNA3.1-LgBiT-ZZ-TEV-3xFlag-TERT	WT	5'GCTGGCTAGCGCTGCCACCATGGTGTTCACCCTGG AAGATTTC3'
		5'CGCGTTTTGTTGTTCTTTGTTGAATTTGTTGTCCAC GGATCCACTTCCACCTCC3'
pcDNA3.1-ZZ-TEV-twin-Strep-SUMO*-TERT	D868A & D869A	5'CTCCTGCGTTTGGTGGCGGCTTTCTTGTTGGTGAC ACC3'
		5'GGTGTCACCAACAAGAAAGCCGCCACCAAACGCA GGAG3'
pcDNA3.1-ZZ-TEV-3xFlag-TERT	D868A & D869A	5'CTCCTGCGTTTGGTGGCGGCTTTCTTGTTGGTGAC ACC3'
		5'GGTGTCACCAACAAGAAAGCCGCCACCAAACGCA GGAG3'
pcDNA3.1-ZZ-TEV-twin-Strep-SUMO*-TERT	D712A	5'CTTTGTCAAGGTGGCGGTGACGGGCGCG3'
		5'CGCGCCCGTCACCGCCACCTTGACAAAG3'
pcDNA3.1-ZZ-TEV-3xFlag-TERT	D712A	5'CTTTGTCAAGGTGGCGGTGACGGGCGCG3'
		5'CGCGCCCGTCACCGCCACCTTGACAAAG3'
pcDNA3.1-ZZ-TEV-twin-Strep-SUMO*-TERT	Δ200–325 (PAL)	5'GCCGAGACCAAGCAC3'
		5'GCAGACCCTACGCTT3'
pcDNA3.1-ZZ-TEV-3xFlag-TERT	Δ200–325 (PAL)	5'GCCGAGACCAAGCAC3'
		5'GCAGACCCTACGCTT3'

Movie S1.

3D variability analysis of the full telomerase dimer performed in CryoSPARC.

Data S1. Pymol session containing the DRRAFTER models of hTR.

Fitted models of the catalytic cores and the H/ACA RNPs in the consensus dimer map are included in the session.

Data S2. Q-scores for different models of the 5' leader sequence of hTR.

Calculated Q-scores for different models of the 5' leader sequence of hTR (nucleotides 1–17). See also fig. S20.

Data S3. Pymol session containing the DRRAFTER models of the 5' G-quadruplex of hTR.

These models were performed using the 3.9 Å reconstruction of the H/ACA RNP dimer. The refined model of the H/ACA RNP dimer is also included in the session as a reference.

References and Notes

1. M. Z. Levy, R. C. Allsopp, A. B. Futcher, C. W. Greider, C. B. Harley, Telomere end-replication problem and cell aging. *J. Mol. Biol.* **225**, 951–960 (1992). doi:10.1016/0022-2836(92)90096-3 Medline

2. R. A. Wu, H. E. Upton, J. M. Vogan, K. Collins, Telomerase mechanism of telomere synthesis. *Annu. Rev. Biochem.* **86**, 439–460 (2017). doi:10.1146/annurev-biochem-061516-045019 Medline

3. E. H. Blackburn, K. Collins, "Telomerase: An RNP enzyme synthesizes DNA" in *RNA Worlds*, R. F. Gesteland, J. F. Atkins, T. R. Cech, Eds. (Cold Spring Harbor Laboratory Press, 2010), pp. 205–213.

4. N. W. Kim, M. A. Piatyszek, K. R. Prowse, C. B. Harley, M. D. West, P. L. C. Ho, G. M. Coviello, W. E. Wright, S. L. Weinrich, J. W. Shay, Specific association of human telomerase activity with immortal cells and cancer. *Science* **266**, 2011–2015 (1994). doi:10.1126/science.7605428 Medline

5. J. W. Shay, S. Bacchetti, A survey of telomerase activity in human cancer. *Eur. J. Cancer* **33**, 787–791 (1997). doi:10.1016/S0959-8049(97)00062-2 Medline

6. G. Sarek, P. Marzec, P. Margalef, S. J. Boulton, Molecular basis of telomere dysfunction in human genetic diseases. *Nat. Struct. Mol. Biol.* **22**, 867–874 (2015). doi:10.1038/nsmb.3093 Medline

7. M. Armanios, The role of telomeres in human disease. *Annu. Rev. Genomics Hum. Genet.* **23**, 363–381 (2022). doi:10.1146/annurev-genom-010422-091101 Medline

8. T. H. D. Nguyen, J. Tam, R. A. Wu, B. J. Greber, D. Toso, E. Nogales, K. Collins, Cryo-EM structure of substrate-bound human telomerase holoenzyme. *Nature* **557**, 190–195 (2018). doi:10.1038/s41586-018-0062-x Medline

9. G. E. Ghanim, A. J. Fountain, A.-M. M. van Roon, R. Rangan, R. Das, K. Collins, T. H. D. Nguyen, Structure of human telomerase holoenzyme with bound telomeric DNA. *Nature* **593**, 449–453 (2021). doi:10.1038/s41586-021-03415-4 Medline

10. F. Wan, Y. Ding, Y. Zhang, Z. Wu, S. Li, L. Yang, X. Yan, P. Lan, G. Li, J. Wu, M. Lei, Zipper head mechanism of telomere synthesis by human telomerase. *Cell Res.* **31**, 1275–1290 (2021). doi:10.1038/s41422-021-00586-7 Medline

11. E. D. Egan, K. Collins, Biogenesis of telomerase ribonucleoproteins. *RNA* **18**, 1747–1759 (2012). doi:10.1261/rna.034629.112 Medline

12. A. S. Venteicher, E. B. Abreu, Z. Meng, K. E. McCann, R. M. Terns, T. D. Veenstra, M. P. Terns, S. E. Artandi, A human telomerase holoenzyme protein required for Cajal body localization and telomere synthesis. *Science* **323**, 644–648 (2009). doi:10.1126/science.1165357 Medline

13. K. T. Tycowski, M. D. Shu, A. Kukoyi, J. A. Steitz, A conserved WD40 protein binds the Cajal body localization signal of scaRNP particles. *Mol. Cell* **34**, 47–57 (2009). doi:10.1016/j.molcel.2009.02.020 Medline

14. G. Schnapp, H.-P. Rodi, W. J. Rettig, A. Schnapp, K. Damm, One-step affinity purification protocol for human telomerase. *Nucleic Acids Res.* **26**, 3311–3313 (1998). doi:10.1093/nar/26.13.3311 Medline

15. C. Wenz, B. Enenkel, M. Amacker, C. Kelleher, K. Damm, J. Lingner, Human telomerase contains two cooperating telomerase RNA molecules. *EMBO J.* **20**, 3526–3534 (2001). doi:10.1093/emboj/20.13.3526 Medline

16. S. B. Cohen, M. E. Graham, G. O. Lovrecz, N. Bache, P. J. Robinson, R. R. Reddel, Protein composition of catalytically active human telomerase from immortal cells. *Science* **315**, 1850–1853 (2007). doi:10.1126/science.1138596 Medline

17. A. Sauerwald, S. Sandin, G. Cristofari, S. H. W. Scheres, J. Lingner, D. Rhodes, Structure of active dimeric human telomerase. *Nat. Struct. Mol. Biol.* **20**, 454–460 (2013). doi:10.1038/nsmb.2530 Medline

18. D. Alves, H. Li, R. Codrington, A. Orte, X. Ren, D. Klenerman, S. Balasubramanian, Single-molecule analysis of human telomerase monomer. *Nat. Chem. Biol.* **4**, 287–289 (2008). doi:10.1038/nchembio.82 Medline

19. R. A. Wu, Y. S. Dagdas, S. T. Yilmaz, A. Yildiz, K. Collins, Single-molecule imaging of telomerase reverse transcriptase in human telomerase holoenzyme and minimal RNP complexes. *eLife* **4**, e08363 (2015). doi:10.7554/eLife.08363 Medline

20. T. M. Errington, D. Fu, J. M. Wong, K. Collins, Disease-associated human telomerase RNA variants show loss of function for telomere synthesis without dominant-negative interference. *Mol. Cell. Biol.* **28**, 6510–6520 (2008). doi:10.1128/MCB.00777-08 Medline

21. E. D. Egan, K. Collins, Specificity and stoichiometry of subunit interactions in the human telomerase holoenzyme assembled in vivo. *Mol. Cell. Biol.* **30**, 2775–2786 (2010). doi:10.1128/MCB.00151-10 Medline

22. B. Liu, Y. He, Y. Wang, H. Song, Z. H. Zhou, J. Feigon, Structure of active human telomerase with telomere shelterin protein TPP1. *Nature* **604**, 578–583 (2022). doi:10.1038/s41586-022-04582-8 Medline

23. Z. Sekne, G. E. Ghanim, A. M. van Roon, T. H. D. Nguyen, Structural basis of human telomerase recruitment by TPP1-POT1. *Science* **375**, 1173–1176 (2022). doi:10.1126/science.abn6840 Medline

24. A. S. Dixon, M. K. Schwinn, M. P. Hall, K. Zimmerman, P. Otto, T. H. Lubben, B. L. Butler, B. F. Binkowski, T. Machleidt, T. A. Kirkland, M. G. Wood, C. T. Eggers, L. P. Encell, K. V. Wood, NanoLuc complementation reporter optimized for accurate measurement of protein interactions in cells. *ACS Chem. Biol.* **11**, 400–408 (2016). doi:10.1021/acschembio.5b00753 Medline

25. T. L. Beattie, W. Zhou, M. O. Robinson, L. Harrington, Functional multimerization of the human telomerase reverse transcriptase. *Mol. Cell. Biol.* **21**, 6151–6160 (2001). doi:10.1128/MCB.21.18.6151-6160.2001 Medline

26. K. Kappel, S. Liu, K. P. Larsen, G. Skiniotis, E. V. Puglisi, J. D. Puglisi, Z. H. Zhou, R. Zhao, R. Das, De novo computational RNA modeling into cryo-EM maps of large

ribonucleoprotein complexes. *Nat. Methods* **15**, 947–954 (2018). doi:10.1038/s41592-018-0172-2 Medline

27. G. E. Ghanim, Z. Sekne, S. Balch, A.-M. M. van Roon, T. H. D. Nguyen, 2.7 Å cryo-EM structure of human telomerase H/ACA ribonucleoprotein. *Nat. Commun.* **15**, 746 (2024). doi:10.1038/s41467-024-45002-x Medline

28. M. E. Sayed, A. Cheng, G. P. Yadav, A. T. Ludlow, J. W. Shay, W. E. Wright, Q.-X. Jiang, Catalysis-dependent inactivation of human telomerase and its reactivation by intracellular telomerase-activating factors (iTAFs). *J. Biol. Chem.* **294**, 11579–11596 (2019). doi:10.1074/jbc.RA118.007234 Medline

29. J. R. Mitchell, J. Cheng, K. Collins, A box H/ACA small nucleolar RNA-like domain at the human telomerase RNA 3′ end. *Mol. Cell. Biol.* **19**, 567–576 (1999). doi:10.1128/MCB.19.1.567 Medline

30. T. Kiss, E. Fayet-Lebaron, B. E. Jády, Box H/ACA small ribonucleoproteins. *Mol. Cell* **37**, 597–606 (2010). doi:10.1016/j.molcel.2010.01.032 Medline

31. J. M. Vogan, X. Zhang, D. T. Youmans, S. G. Regalado, J. Z. Johnson, D. Hockemeyer, K. Collins, Minimized human telomerase maintains telomeres and resolves endogenous roles of H/ACA proteins, TCAB1, and Cajal bodies. *eLife* **5**, e18221 (2016). doi:10.7554/eLife.18221 Medline

32. E. D. Egan, K. Collins, An enhanced H/ACA RNP assembly mechanism for human telomerase RNA. *Mol. Cell. Biol.* **32**, 2428–2439 (2012). doi:10.1128/MCB.00286-12 Medline

33. C. Trahan, C. Martel, F. Dragon, Effects of dyskeratosis congenita mutations in dyskerin, NHP2 and NOP10 on assembly of H/ACA pre-RNPs. *Hum. Mol. Genet.* **19**, 825–836 (2010). doi:10.1093/hmg/ddp551 Medline

34. D. Fu, K. Collins, Distinct biogenesis pathways for human telomerase RNA and H/ACA small nucleolar RNAs. *Mol. Cell* **11**, 1361–1372 (2003). doi:10.1016/S1097-2765(03)00196-5 Medline

35. P. A. Chong, R. M. Vernon, J. D. Forman-Kay, RGG/RG motif regions in RNA binding and phase separation. *J. Mol. Biol.* **430**, 4650–4665 (2018). doi:10.1016/j.jmb.2018.06.014 Medline

36. J. Gros, A. Guédin, J.-L. Mergny, L. Lacroix, G-Quadruplex formation interferes with P1 helix formation in the RNA component of telomerase hTERC. *ChemBioChem* **9**, 2075–2079 (2008). doi:10.1002/cbic.200800300 Medline

37. X. Li, H. Nishizuka, K. Tsutsumi, Y. Imai, Y. Kurihara, S. Uesugi, Structure, interactions and effects on activity of the 5′-terminal region of human telomerase RNA. *J. Biochem.* **141**, 755–765 (2007). doi:10.1093/jb/mvm081 Medline

38. A. N. Sexton, K. Collins, The 5′ guanosine tracts of human telomerase RNA are recognized by the G-quadruplex binding domain of the RNA helicase DHX36 and function to increase RNA accumulation. *Mol. Cell. Biol.* **31**, 736–743 (2011). doi:10.1128/MCB.01033-10 Medline

39. S. Lattmann, M. B. Stadler, J. P. Vaughn, S. A. Akman, Y. Nagamine, The DEAH-box RNA helicase RHAU binds an intramolecular RNA G-quadruplex in TERC and associates with telomerase holoenzyme. *Nucleic Acids Res.* **39**, 9390–9404 (2011). doi:10.1093/nar/gkr630 Medline

40. J. L. Chen, M. A. Blasco, C. W. Greider, Secondary structure of vertebrate telomerase RNA. *Cell* **100**, 503–514 (2000). doi:10.1016/S0092-8674(00)80687-X Medline

41. E. P. Booy, M. Meier, N. Okun, S. K. Novakowski, S. Xiong, J. Stetefeld, S. A. McKenna, The RNA helicase RHAU (*DHX36*) unwinds a G4-quadruplex in human telomerase RNA and promotes the formation of the P1 helix template boundary. *Nucleic Acids Res.* **40**, 4110–4124 (2012). doi:10.1093/nar/gkr1306 Medline

42. Z. Lu, S. Xie, H. Su, S. Han, H. Huang, X. Zhou, Identification of G-quadruplex-interacting proteins in living cells using an artificial G4-targeting biotin ligase. *Nucleic Acids Res.* **52**, e37 (2024). doi:10.1093/nar/gkae126 Medline

43. J. Wapling, K. L. Moore, S. Sonza, J. Mak, G. Tachedjian, Mutations that abrogate human immunodeficiency virus type 1 reverse transcriptase dimerization affect maturation of the reverse transcriptase heterodimer. *J. Virol.* **79**, 10247–10257 (2005). doi:10.1128/JVI.79.16.10247-10257.2005 Medline

44. T. Restle, B. Müller, R. S. Goody, Dimerization of human immunodeficiency virus type 1 reverse transcriptase. A target for chemotherapeutic intervention. *J. Biol. Chem.* **265**, 8986–8988 (1990). doi:10.1016/S0021-9258(19)38799-X Medline

45. R. S. Fletcher, G. Holleschak, E. Nagy, D. Arion, G. Borkow, Z. Gu, M. A. Wainberg, M. A. Parniak, Single-step purification of recombinant wild-type and mutant HIV-1 reverse transcriptase. *Protein Expr. Purif.* **7**, 27–32 (1996). doi:10.1006/prep.1996.0004 Medline

46. C.-K. Tseng, H.-F. Wang, M. R. Schroeder, P. Baumann, The H/ACA complex disrupts triplex in hTR precursor to permit processing by RRP6 and PARN. *Nat. Commun.* **9**, 5430 (2018). doi:10.1038/s41467-018-07822-6 Medline

47. K. G. Zyner, D. S. Mulhearn, S. Adhikari, S. Martínez Cuesta, M. Di Antonio, N. Erard, G. J. Hannon, D. Tannahill, S. Balasubramanian, Genetic interactions of G-quadruplexes in humans. *eLife* **8**, e46793 (2019). doi:10.7554/eLife.46793 Medline

48. I. A. Hendriks, R. C. J. D'Souza, B. Yang, M. Verlaan-de Vries, M. Mann, A. C. O. Vertegaal, Uncovering global SUMOylation signaling networks in a site-specific manner. *Nat. Struct. Mol. Biol.* **21**, 927–936 (2014). doi:10.1038/nsmb.2890 Medline

49. S. E. Whitehead, K. W. Jones, X. Zhang, X. Cheng, R. M. Terns, M. P. Terns, Determinants of the interaction of the spinal muscular atrophy disease protein SMN with the dimethylarginine-modified box H/ACA small nucleolar ribonucleoprotein GAR1. *J. Biol. Chem.* **277**, 48087–48093 (2002). doi:10.1074/jbc.M204551200 Medline

50. J. C. Schmidt, A. J. Zaug, T. R. Cech, Live cell imaging reveals the dynamics of telomerase recruitment to telomeres. *Cell* **166**, 1188–1197.e9 (2016). doi:10.1016/j.cell.2016.07.033 Medline

51. J. Jiang, E. J. Miracco, K. Hong, B. Eckert, H. Chan, D. D. Cash, B. Min, Z. H. Zhou, K. Collins, J. Feigon, The architecture of *Tetrahymena* telomerase holoenzyme. *Nature* **496**, 187–192 (2013). doi:10.1038/nature12062 Medline

52. E. Bajon, N. Laterreur, R. J. Wellinger, A single templating RNA in yeast telomerase. *Cell Rep.* **12**, 441–448 (2015). doi:10.1016/j.celrep.2015.06.045 Medline

53. J. D. Podlevsky, C. J. Bley, R. V. Omana, X. Qi, J. J. Chen, The Telomerase Database. *Nucleic Acids Res.* **36**, D339–D343 (2008). doi:10.1093/nar/gkm700 Medline

54. D. Kimanius, L. Dong, G. Sharov, T. Nakane, S. H. W. Scheres, New tools for automated cryo-EM single-particle analysis in RELION-4.0. *Biochem. J.* **478**, 4169–4185 (2021). doi:10.1042/BCJ20210708 Medline

55. D. Kimanius, K. Jamali, M. E. Wilkinson, S. Lövestam, V. Velazhahan, T. Nakane, S. H. W. Scheres, Data-driven regularization lowers the size barrier of cryo-EM structure determination. *Nat. Methods* **21**, 1216–1221 (2024). doi:10.1038/s41592-024-02304-8 Medline

56. A. Rohou, N. Grigorieff, CTFFIND4: Fast and accurate defocus estimation from electron micrographs. *J. Struct. Biol.* **192**, 216–221 (2015). doi:10.1016/j.jsb.2015.08.008 Medline

57. J. Zivanov, T. Nakane, B. O. Forsberg, D. Kimanius, W. J. H. Hagen, E. Lindahl, S. H. W. Scheres, New tools for automated high-resolution cryo-EM structure determination in RELION-3. *eLife* **7**, e42166 (2018). doi:10.7554/eLife.42166 Medline

58. M. Zubradt, P. Gupta, S. Persad, A. M. Lambowitz, J. S. Weissman, S. Rouskin, DMS-MaPseq for genome-wide or targeted RNA structure probing in vivo. *Nat. Methods* **14**, 75–82 (2017). doi:10.1038/nmeth.4057 Medline

59. D. Mitchell III, J. Cotter, I. Saleem, A. M. Mustoe, Mutation signature filtering enables high-fidelity RNA structure probing at all four nucleobases with DMS. *Nucleic Acids Res.* **51**, 8744–8757 (2023). doi:10.1093/nar/gkad522 Medline

60. H. Li, Minimap2: Pairwise alignment for nucleotide sequences. *Bioinformatics* **34**, 3094–3100 (2018). doi:10.1093/bioinformatics/bty191 Medline

61. N. M. Forino, J. Z. Woo, A. J. Zaug, A. G. Jimenez, E. Edelson, T. R. Cech, S. Rouskin, M. D. Stone, Telomerase RNA structural heterogeneity in living human cells detected by DMS-MaPseq. *Nat. Commun.* **16**, 925 (2025). doi:10.1038/s41467-025-56149-6 Medline

62. A. Punjani, J. L. Rubinstein, D. J. Fleet, M. A. Brubaker, cryoSPARC: Algorithms for rapid unsupervised cryo-EM structure determination. *Nat. Methods* **14**, 290–296 (2017). doi:10.1038/nmeth.4169 Medline

63. T. Bepler, A. Morin, M. Rapp, J. Brasch, L. Shapiro, A. J. Noble, B. Berger, Positive-unlabeled convolutional neural networks for particle picking in cryo-electron micrographs. *Nat. Methods* **16**, 1153–1160 (2019). doi:10.1038/s41592-019-0575-8 Medline

64. A. Punjani, H. Zhang, D. J. Fleet, Non-uniform refinement: Adaptive regularization improves single-particle cryo-EM reconstruction. *Nat. Methods* **17**, 1214–1221 (2020). doi:10.1038/s41592-020-00990-8 Medline

65. D. Asarnow, E. Palovcak, Y. Cheng, asarnow/pyem: UCSF pyem v0.5 (v0.5), Zenodo (2019); https://doi.org/10.5281/zenodo.3576630.

66. A. Punjani, D. J. Fleet, 3D variability analysis: Resolving continuous flexibility and discrete heterogeneity from single particle cryo-EM. *J. Struct. Biol.* **213**, 107702 (2021). doi:10.1016/j.jsb.2021.107702 Medline

67. J. Zivanov, T. Nakane, S. H. W. Scheres, Estimation of high-order aberrations and anisotropic magnification from cryo-EM data sets in *RELION*-3.1. *IUCrJ* **7**, 253–267 (2020). doi:10.1107/S2052252520000081 Medline

68. G. N. Murshudov, P. Skubák, A. A. Lebedev, N. S. Pannu, R. A. Steiner, R. A. Nicholls, M. D. Winn, F. Long, A. A. Vagin, REFMAC5 for the refinement of macromolecular crystal structures. *Acta Crystallogr. D Biol. Crystallogr.* **67**, 355–367 (2011). doi:10.1107/S0907444911001314 Medline

69. A. Brown, F. Long, R. A. Nicholls, J. Toots, P. Emsley, G. Murshudov, Tools for macromolecular model building and refinement into electron cryo-microscopy reconstructions. *Acta Crystallogr. D Biol. Crystallogr.* **71**, 136–153 (2015). doi:10.1107/S1399004714021683 Medline

70. A. Casañal, B. Lohkamp, P. Emsley, Current developments in Coot for macromolecular model building of electron cryo-microscopy and crystallographic data. *Protein Sci.* **29**, 1069–1078 (2020). doi:10.1002/pro.3791 Medline

71. F.-C. Chou, N. Echols, T. C. Terwilliger, R. Das, RNA structure refinement using the ERRASER-Phenix pipeline. *Methods Mol. Biol.* **1320**, 269–282 (2016). doi:10.1007/978-1-4939-2763-0_17 Medline

72. K. Yamashita, C. M. Palmer, T. Burnley, G. N. Murshudov, Cryo-EM single-particle structure refinement and map calculation using *Servalcat*. *Acta Crystallogr. D Struct. Biol.* **77**, 1282–1291 (2021). doi:10.1107/S2059798321009475 Medline

73. R. A. Nicholls, M. Fischer, S. McNicholas, G. N. Murshudov, Conformation-independent structural comparison of macromolecules with *ProSMART*. *Acta Crystallogr. D Biol. Crystallogr.* **70**, 2487–2499 (2014). doi:10.1107/S1399004714016241 Medline

74. D. Liebschner, P. V. Afonine, M. L. Baker, G. Bunkóczi, V. B. Chen, T. I. Croll, B. Hintze, L.-W. Hung, S. Jain, A. J. McCoy, N. W. Moriarty, R. D. Oeffner, B. K. Poon, M. G. Prisant, R. J. Read, J. S. Richardson, D. C. Richardson, M. D. Sammito, O. V. Sobolev, D. H. Stockwell, T. C. Terwilliger, A. G. Urzhumtsev, L. L. Videau, C. J. Williams, P. D. Adams, Macromolecular structure determination using X-rays, neutrons and electrons: Recent developments in *Phenix*. *Acta Crystallogr. D Struct. Biol.* **75**, 861–877 (2019). doi:10.1107/S2059798319011471 Medline

75. C. J. Williams, J. J. Headd, N. W. Moriarty, M. G. Prisant, L. L. Videau, L. N. Deis, V. Verma, D. A. Keedy, B. J. Hintze, V. B. Chen, S. Jain, S. M. Lewis, W. B. Arendall 3rd, J. Snoeyink, P. D. Adams, S. C. Lovell, J. S. Richardson, D. C. Richardson, MolProbity: More and better reference data for improved all-atom structure validation. *Protein Sci.* **27**, 293–315 (2018). doi:10.1002/pro.3330 Medline

76. H. Martadinata, A. T. Phan, Formation of a stacked dimeric G-quadruplex containing bulges by the 5′-terminal region of human telomerase RNA (hTERC). *Biochemistry* **53**, 1595–1600 (2014). doi:10.1021/bi4015727 Medline

77. T. D. Goddard, C. C. Huang, E. C. Meng, E. F. Pettersen, G. S. Couch, J. H. Morris, T. E. Ferrin, UCSF ChimeraX: Meeting modern challenges in visualization and analysis. *Protein Sci.* **27**, 14–25 (2018). doi:10.1002/pro.3235 Medline

78. C. Cheong, P. B. Moore, Solution structure of an unusually stable RNA tetraplex containing G- and U-quartet structures. *Biochemistry* **31**, 8406–8414 (1992). doi:10.1021/bi00151a003 Medline

79. G. Pintilie, K. Zhang, Z. Su, S. Li, M. F. Schmid, W. Chiu, Measurement of atom resolvability in cryo-EM maps with Q-scores. *Nat. Methods* **17**, 328–334 (2020). doi:10.1038/s41592-020-0731-1 Medline

80. E. F. Pettersen, T. D. Goddard, C. C. Huang, G. S. Couch, D. M. Greenblatt, E. C. Meng, T. E. Ferrin, UCSF Chimera—A visualization system for exploratory research and analysis. *J. Comput. Chem.* **25**, 1605–1612 (2004). doi:10.1002/jcc.20084 Medline

81. S. Aiyer, C. Zhang, P. R. Baldwin, D. Lyumkis, Evaluating local and directional resolution of cryo-EM density maps. *Methods Mol. Biol.* **2215**, 161–187 (2021). doi:10.1007/978-1-0716-0966-8_8 Medline

82. F. Sievers, A. Wilm, D. Dineen, T. J. Gibson, K. Karplus, W. Li, R. Lopez, H. McWilliam, M. Remmert, J. Söding, J. D. Thompson, D. G. Higgins, Fast, scalable generation of high-quality protein multiple sequence alignments using Clustal Omega. *Mol. Syst. Biol.* **7**, 539 (2011). doi:10.1038/msb.2011.75 Medline

83. X. Robert, P. Gouet, Deciphering key features in protein structures with the new ENDscript server. *Nucleic Acids Res.* **42**, W320–W324 (2014). doi:10.1093/nar/gku316 Medline